1-1-2008

Thermal modeling of a high concentration photovoltaic system

Aaron M Sahm
University of Nevada, Las Vegas

THERMAL MODELING OF A HIGH CONCENTRATION PHOTOVOLTAIC SYSTEM

By

Aaron M. Sahm

Bachelor of Science in Engineering
University of Nevada, Las Vegas
2006

A thesis submitted in partial fulfillment
of the requirements for the

Master of Science Degree in Mechanical Engineering
Howard R. Hughes College of Engineering
Department of Mechanical Engineering

Graduate College
University of Nevada, Las Vegas
May 2008

UNLV
UNIVERSITY OF NEVADA LAS VEGAS

Thesis Approval

The Graduate College
University of Nevada, Las Vegas

April 17th, 2008

The Thesis prepared by

Aaron Michael Sahm

Entitled

Thermal Modeling of a High Concentration Photovoltaic System

is approved in partial fulfillment of the requirements for the degree of

Master of Science in Engineering

Examination Committee Chair

Dean of the Graduate College

Examination Committee Member

Examination Committee Member

Examination Committee Member

Graduate College Faculty Representative

1017-53

ABSTRACT

Thermal Modeling of a High Concentration Photovoltaic System

by

Aaron Sahm

Dr. Robert F. Boehm, Examination Committee Chair
Professor of Mechanical Engineering
University of Nevada, Las Vegas

A two-dimensional numerical model was developed to simulate a single chamber with an array of cells for a high concentration photovoltaic system. Gambit was used to generate the computational mesh and Fluent was used to obtain the numerical simulation results. The cells were treated as heat sources with efficiencies that change as a function of temperature. Initially a simulation was run with an assumed cell efficiency of 25%. After the maximum temperature was determined, the cell efficiency was calculated and input into the model to recalculate the temperature solution. Radiation and convection modes of heat transfer were the primary focus as well as air velocity and density. The results from this study were then compared with a previous numerical model and with two cases of measured temperature and air velocity data from the system being modeled. Although wind plays a large role in the chamber temperatures, it was not considered in the model. However, wind was shown to be present when the results of the model and experiment differ significantly.

The temperature and air velocity data were measured in two ways. The first way used a set of candlestick sensors that measure both temperature and air velocity 9 mm from their mounted surface. The second way was with a thermal camera. Also a method for using the camera on a surface with non-uniform emissivities was developed. Generally good agreement was shown between computations and measurements.

TABLE OF CONTENTS

LIST OF FIGURES

LIST OF TABLES

ACKNOWLEDGEMENTS

I would like to thank Dr. Robert Boehm for not only providing me with the opportunity to work at the Center for Energy Research at the University of Nevada, Las Vegas but also for being a great professor and advisor. I would also like to thank Allison Gray who helped me learn and use Fluent which was very critical to the thesis work. Finally, I would like to thank my parents who always encouraged me to learn.

CHAPTER 1

INTRODUCTION

Background

The problem discussed in this manuscript is the thermal modeling of a single chamber of a high concentration photovoltaic system. The variables that are considered are DNI (direct normal radiation), elevation angle of chamber, ambient temperature, cell efficiency, and material radiation properties. Previous work on developing a model for this system has been done and focused on heat convection with fixed cell temperatures with the purpose of determining the chamber temperature profile and the heat transfer coefficient. In this case, the temperature profile as well as other states are determined from ambient parameters such as solar irradiance, ambient temperature, pressure, and angle of chamber. A radiation model is also incorporated to investigate the role that radiation plays in this case. All of these parameters are given by weather data collected at the Center for Energy Research at the University of Nevada, Las Vegas.

Solar Cells

When sunlight hits a solar cell, some percentage of that light is reflected, some is converted to electricity, some passes through, and the rest is lost as

heat. The percentage that passes through is due to photons whose energies are less than the band gap energy E_g of the material [1]. The electron energy band gap diagram can be seen in Figure 1. The photons with energy greater than the band gap make electron hole pairs by stripping an electron from the valence band and moving it to the bottom of the conduction band which leaves a hole at the top of the valence band. The excess energy above the band gap is lost as phonons (heat).

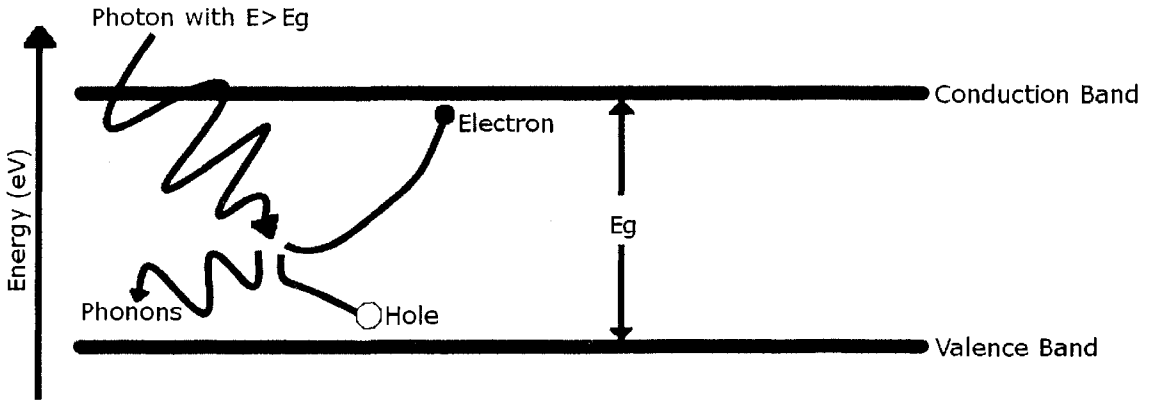

Figure 1. Electron energy band diagram.

This heat along with ambient temperature leads to a higher cell temperature. It is well known that as the cell temperature increases, cell efficiency decreases which will lead to lower power output through an increased resistance from lower mobility. Thus, the determination of the temperature of the cell under differing conditions will help to find what kind of power output to expect from solar technologies as well as a method of determining the performance of the system.

The Center for Energy Research at UNLV has a weather station which monitors ambient temperature, direct normal irradiance, global horizontal irradiance, wind speed, and humidity. These parameters were used in both the numerical model and the experimental. The first time period examined was a typical June or July Las Vegas day. Very high ambient temperatures as well as high DNI occur simultaneously during these months.

The model is steady state and assumes no wind, an initial cell efficiency of 25%, and a 15% transmittance loss through the Fresnel lens with a uniform flux on the cell. See Figure 2 for a graphical representation of the model.

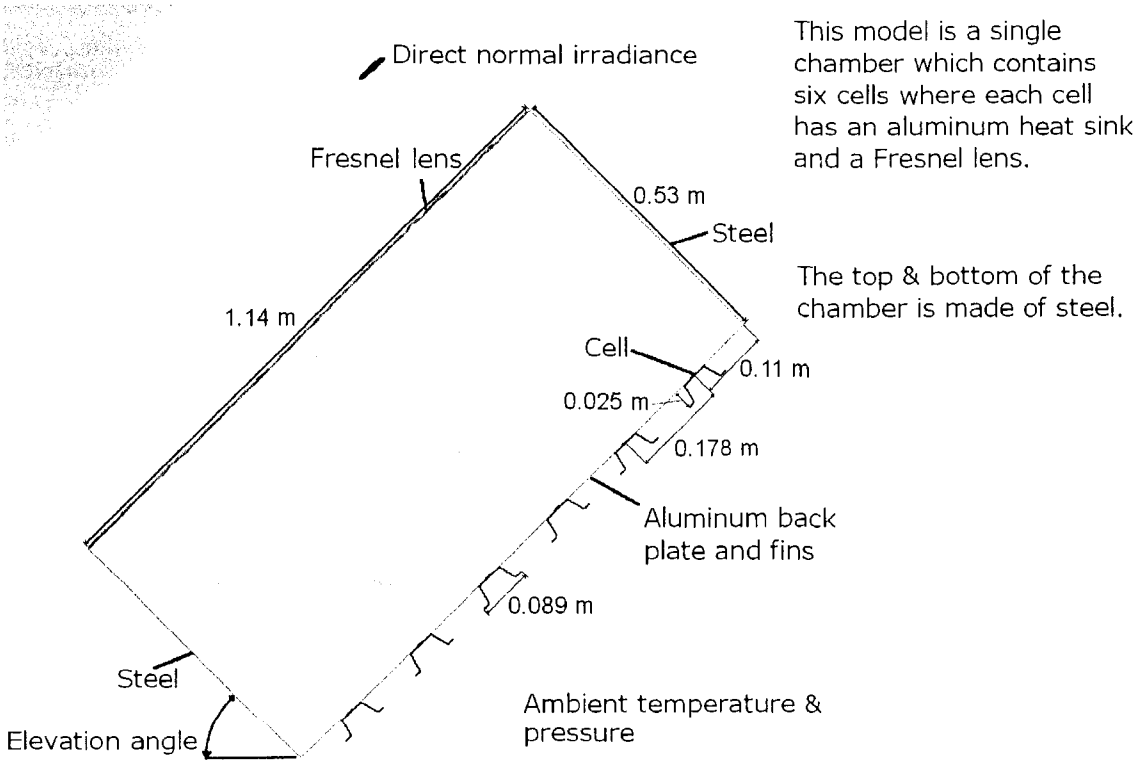

Figure 2. Model description.

There are several differences between the model and the test chamber. The model is two dimensional where as the test chamber is three dimensional. This will mean that the model will not account for heat transfer between other chambers to the side and on top. The test chamber chosen was closest to this situation because its location was to the bottom right of one of the megamodules. This gave it contact with the ambient air on all sides except for its left and top sides. The model does not take into account heat transfer with other surrounding objects such as the ground or global horizontal radiation. The test chamber has other factors that cannot be accounted for like cell or string mismatching and slight errors in tracking due to hardware or wind. The ambient input parameters are air temperature, pressure, and direct normal incidence. Each cell is treated as a single heat source. The value of these heat sources are calculated through two equations. This is done by multiplying the DNI by several factors. They are the area of the Fresnel lens, the transmittance of the lens, and one minus the cell efficiency. Then that value is divided by the volume of a single cell. Cell reflectance was not considered.

$$q = \frac{I \cdot \tau_L \cdot A_L \cdot (1 - \eta_c)}{V_c} \qquad (1)$$

Where q = Heat source (W/m^3)

I = Direct normal incidence (W/m^2)

τ_L = Transmittance through Fresnel lens

A_L = Area of lens (m^2)

η_c = Cell efficiency

V_c = Volume of cell (m^3)

Cell efficiency is a function of temperature, so as temperature increases the cell efficiency decreases [2]. This means that the first simulations will under predict the cell temperatures. This will make the determination of the cell temperature an iterative process where to find the correct cell temperature, a slightly lower efficiency will have to be input into the model and run again for the same conditions until the temperature no longer changes significantly. The equation for cell efficiency can be seen below.

$$\eta(T) = -0.065 \cdot T(K) + 44.48 \qquad (2)$$

where T = Temperature in Kelvin

η = Cell efficiency

Fresnel Lens Study

As was stated before, a transmittance loss of 15% was assumed for this model [3]. Because this value is a critical component in the determination of the heat source, two methods were employed in finding it. One way was through testing of the acrylic and the other was by calculating the transmittance from data found from the manufacturer of the acrylic. An image of the Fresnel lens can be seen in Figure 3. The testing was performed with an Eppley Normal Incidence Pyrheliometer and the sun (Figure 4).

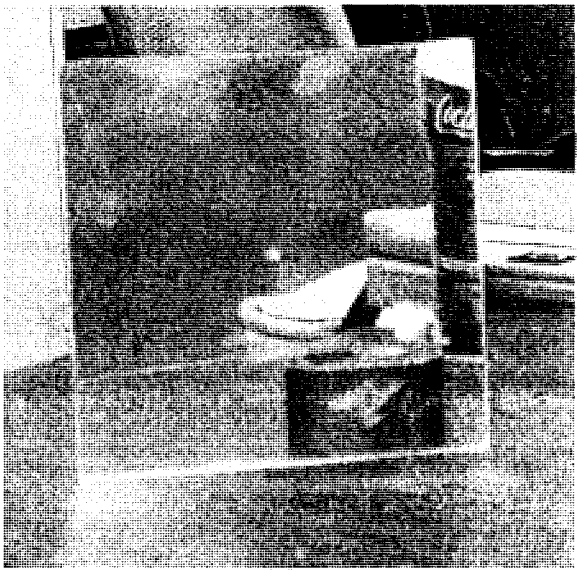

Figure 3. 7 X 7 inch Fresnel lens.

Figure 4. Image two Eppley normal incidence pyrheliometers on a tracker.

First the sun's normal irradiance was measured and then a sheet of acrylic was quickly placed flat against the sensor and the measurement was taken again. The transmittance was found by taking the second result and dividing it by the first. This was done about 50 times for a related study [4]. The average transmittance was found to be about 85%. The manufacturer of the acrylic is Cyro industries [5]. They have graphs of transmittance for several of their products although they are labeled with a warning that they are approximations and not specifications. The transmittance can be seen in Figure 5 as a function of wavelength.

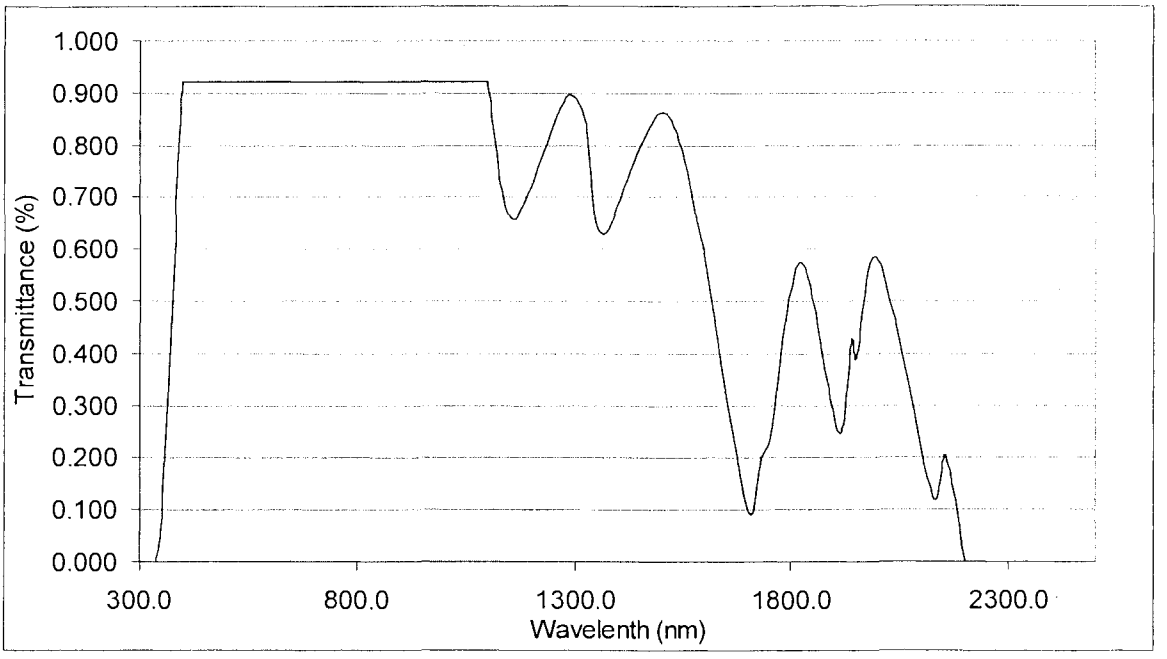

Figure 5. Transmittance of Acrylite FF sheet.

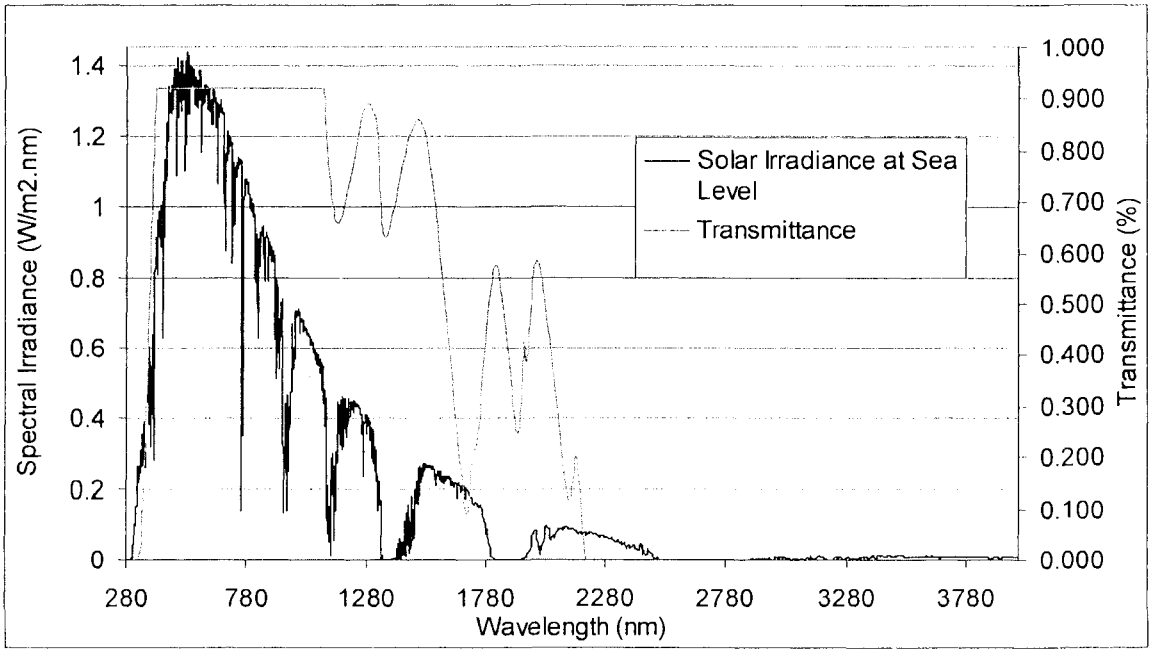

Figure 6. Direct normal spectral irradiance with Acrylite transmittance.

Direct normal spectral irradiance was then used to calculate the overall transmittance over the spectrum in Figure 6. The overall transmittance was calculated by multiplying the transmittance by the irradiance [6] and then dividing by the total irradiance. This was only done with the wavelength range given from 340 to 2200 nm. This gave an overall transmittance of 84%. These results are only on the material with the same thickness and not the Fresnel lens itself. It is assumed that the Fresnel lens pattern does not affect the overall transmittance of the material.

Mesh Study

In order to confirm whether results from the simulations are correct, a mesh analysis was done. This is done because the denser the mesh the more accurate the model solution. But, the denser the mesh, the longer it takes for a simulation

to converge to a solution. Different meshes must be created to find the optimum mesh where accuracy and time are accounted for. Several different meshes were created in Gambit using different mesh densities such as extremely dense, very dense, and coarse. In order to see which mesh scheme was better, some of the meshes were created with triangular schemes, some were quadrilateral, and some were combinations of both. A simulation was run with each mesh to see what the temperature profile would converge to. Simulations were also run with the use of the radiation models. This would slow down the process significantly. It was also desired to keep the domain size similar to meshes that were developed previously for comparison. The densest mesh images are shown in Figures 7 and 8.

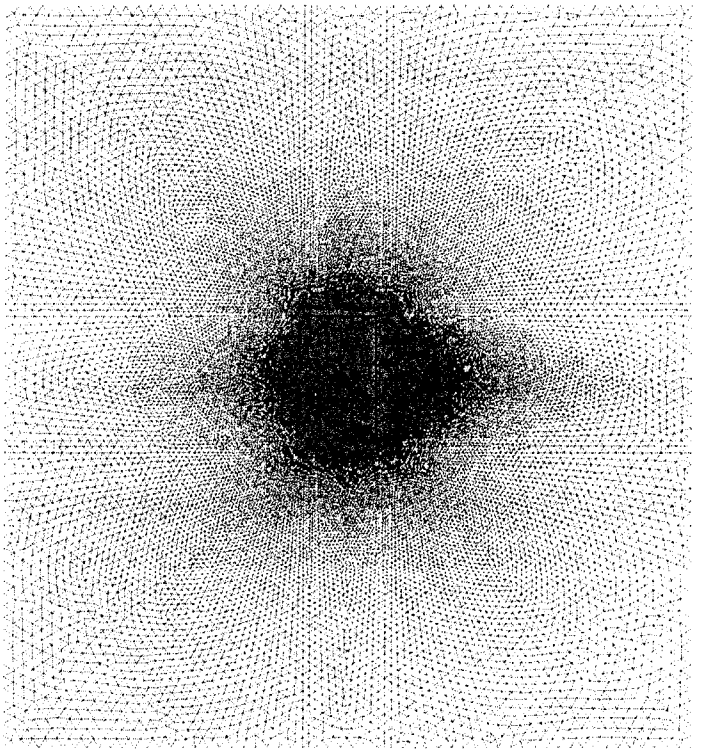

Figure 7. Densest mesh domain.

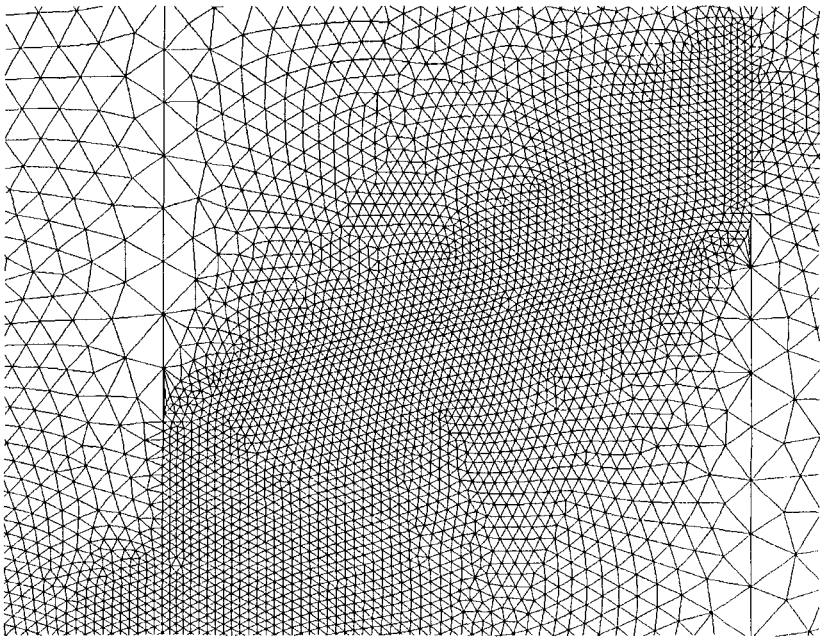

Figure 8. Close-up on densest mesh heat fin.

Figure 8 is a close up on one of the heat fins in the densest mesh. For comparison the next two figures are of the coarse mesh.

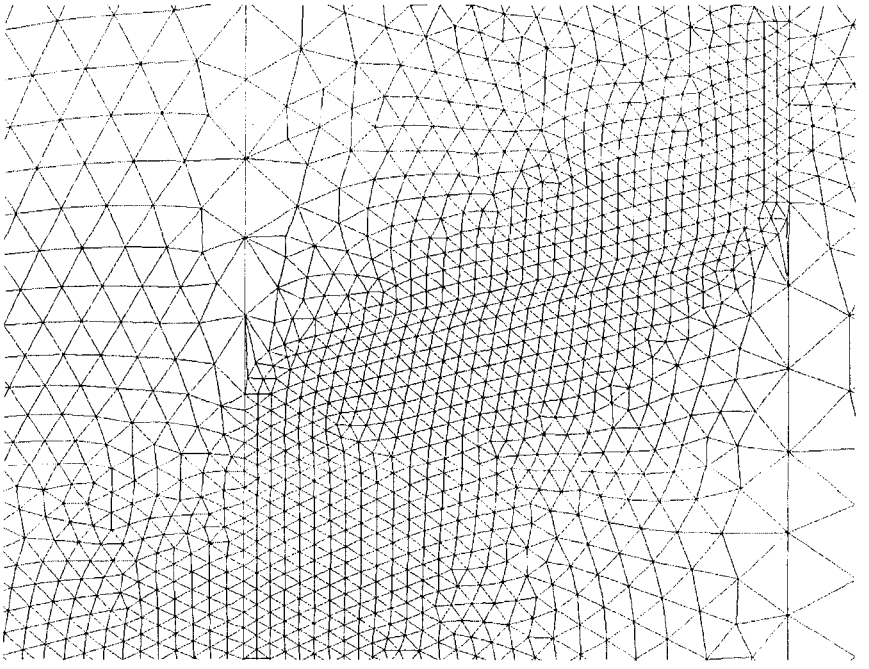

Figure 9. Close-up on coarser mesh heat fin.

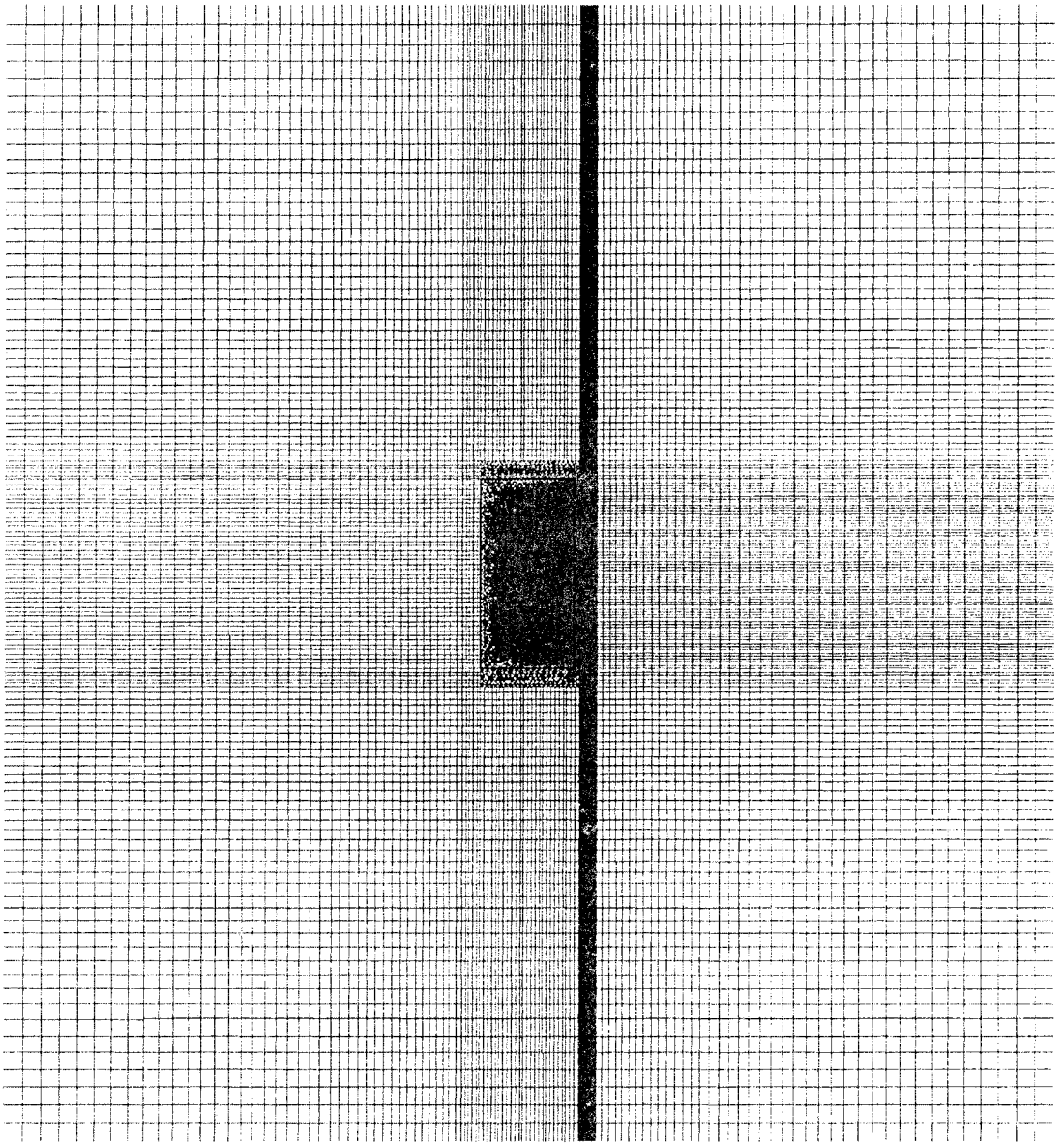

Figure 10. Coarse mesh domain.

A line of six temperature and air velocity values was taken down the length the chamber. The values at these points were compared for each mesh and can be seen in Figure 11 and 12. Although the coarse mesh is not entirely mesh independent, it was found to be sufficient. The maximum temperature difference between the coarsest mesh and the densest mesh was 1.5 degrees.

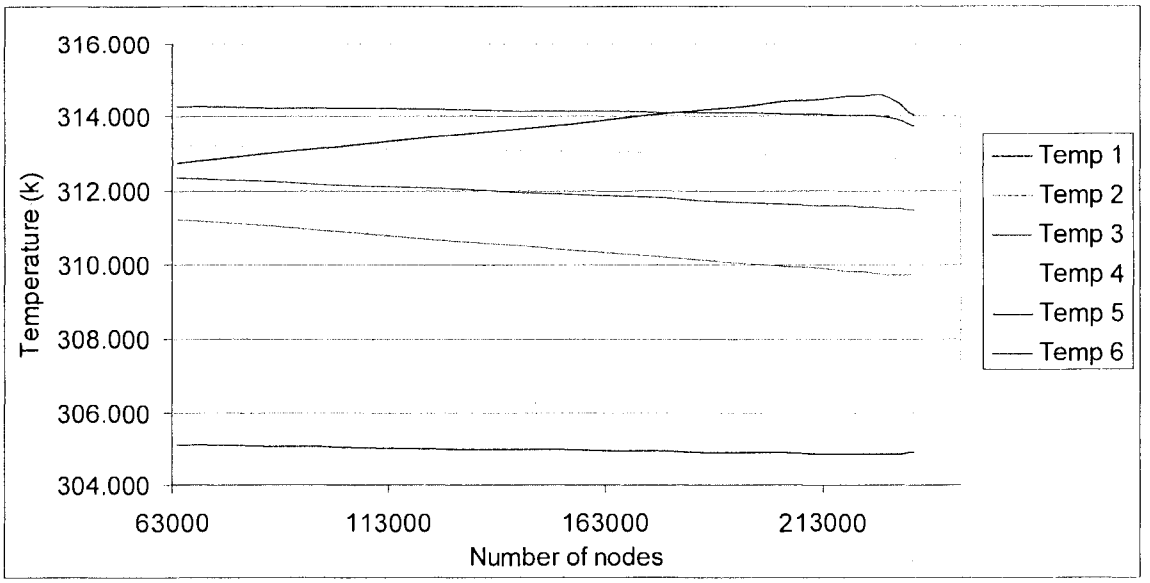

Figure 11. Temperatures along vertical line of chamber vs. number of nodes.

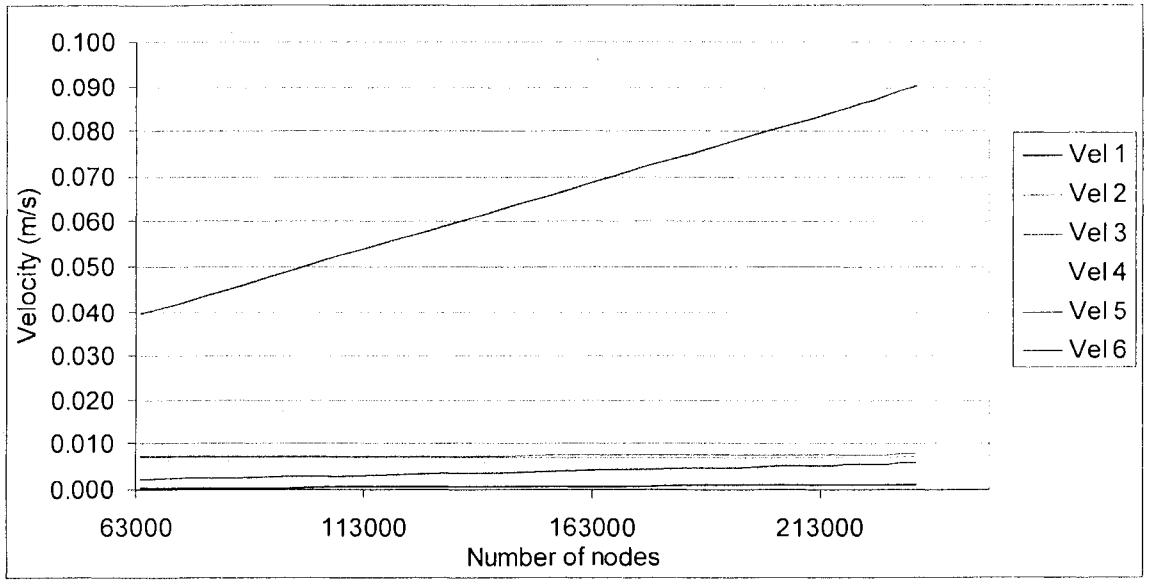

Figure 12. Velocities along vertical line of chamber vs. number of nodes.

Some of the meshes were found to be unstable and produced bizarre results. The densest meshes were generally stable but took weeks to converge. Further

accuracy would be very good but the computation time was much too great with the time available. The equations Fluent uses are given and discussed in the Appendix. The discretization scheme used for momentum and energy was second order upwind. The discretization scheme for pressure used was body forced weighted. The turbulence k-ε model was used because the Rayleigh number for the backplate was found to be above 10^9 for several cases. The range of relaxation factors used in the model can be seen in Table 1 and the material properties can be seen in Table 2.

Table 1. Range of Relaxation Factors Used.

Pressure	Density	Body Forces	Momentum	Turbulent Kinetic Energy
0.2-0.3	0.999-1	0.999-1	0.5-0.7	0.5-0.8
Turbulent Dissipation Rate	Turbulent Viscosity	Energy	P1	
0.5-0.8	1	0.997-1	0.8	

Table 2. Material Properties.

Property	ρ (kg/m^3)	C_p (J/kg-K)	k (W/m-K)	μ (kg/m-s)	Molecular Weight (kg/kgmol)
Air	ideal gas	1006.43	0.0242	1.7894·10-5	28.966
Acrylic	1149	1461.193	0.1902535	n/a	n/a
Aluminum	2719	871	202.4	n/a	n/a
Steel	8030	502.48	16.27	n/a	n/a

Convection Model Example

The first model studied was purely convection. Different points through out the day were input into the model. The first point is in the morning when the model is at a 15° elevation angle. The ambient temperature is low, at 304 K (31° C) and the ambient pressure is at 94113 Pa.

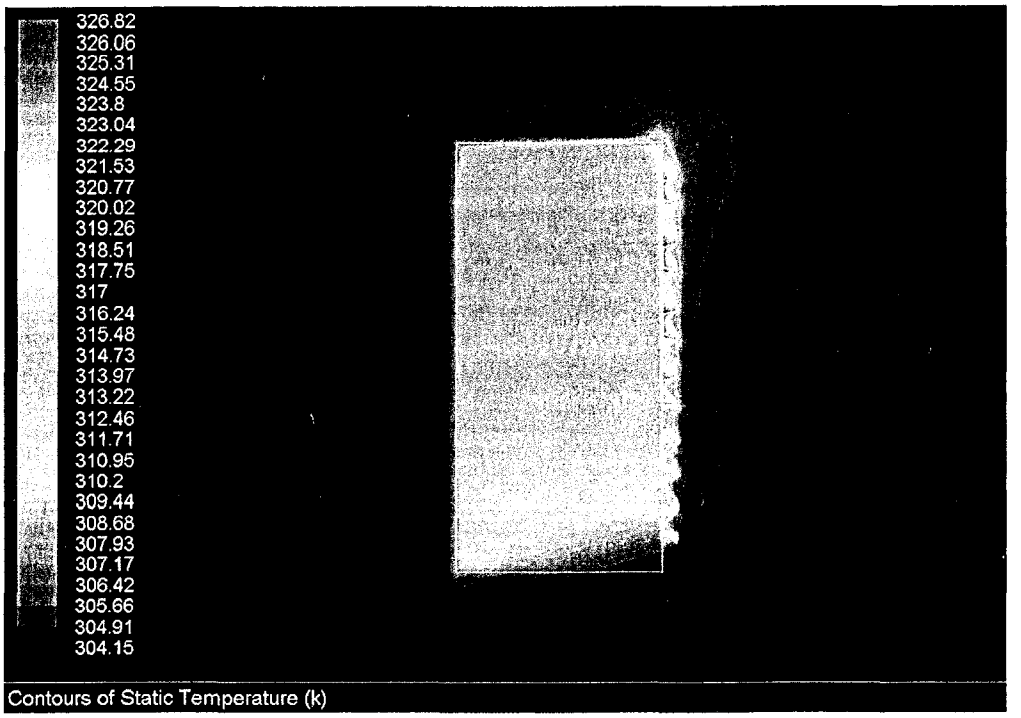

Figure 13. Temperature profile in Kelvin of chamber at a 15 degree elevation angle.

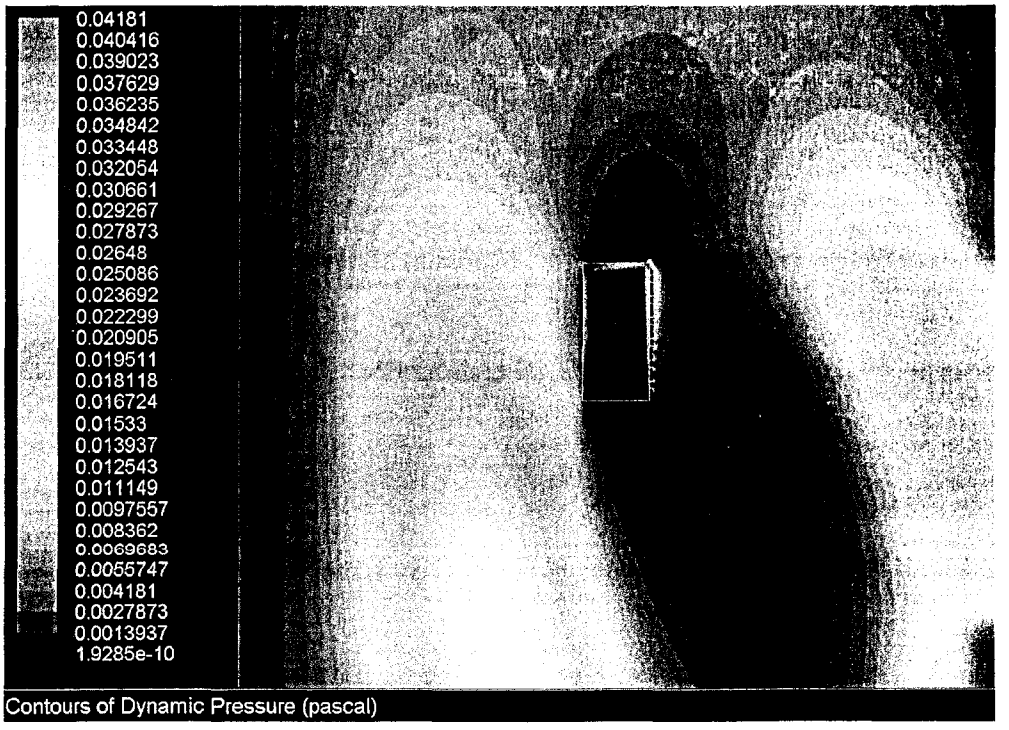

Figure 14. Pressure profile in Pascal for chamber at a 15 degree elevation angle.

The max temperature converged to 323.65 K (50.5° C). Because of the low elevation angle, a somewhat large vertical temperature distribution exists inside the chamber. Figure 14 shows the pressure distribution. There wasn't a large change in pressure. The model treats air as an incompressible ideal gas and assumes a sealed chamber which is not the way the actual chamber is. According to the model, there was only an addition of 1 Pa which if it is accurate should be even less in reality. Figure 15 shows the density profile which drops about 0.07 kg/m^3 from the ambient air density.

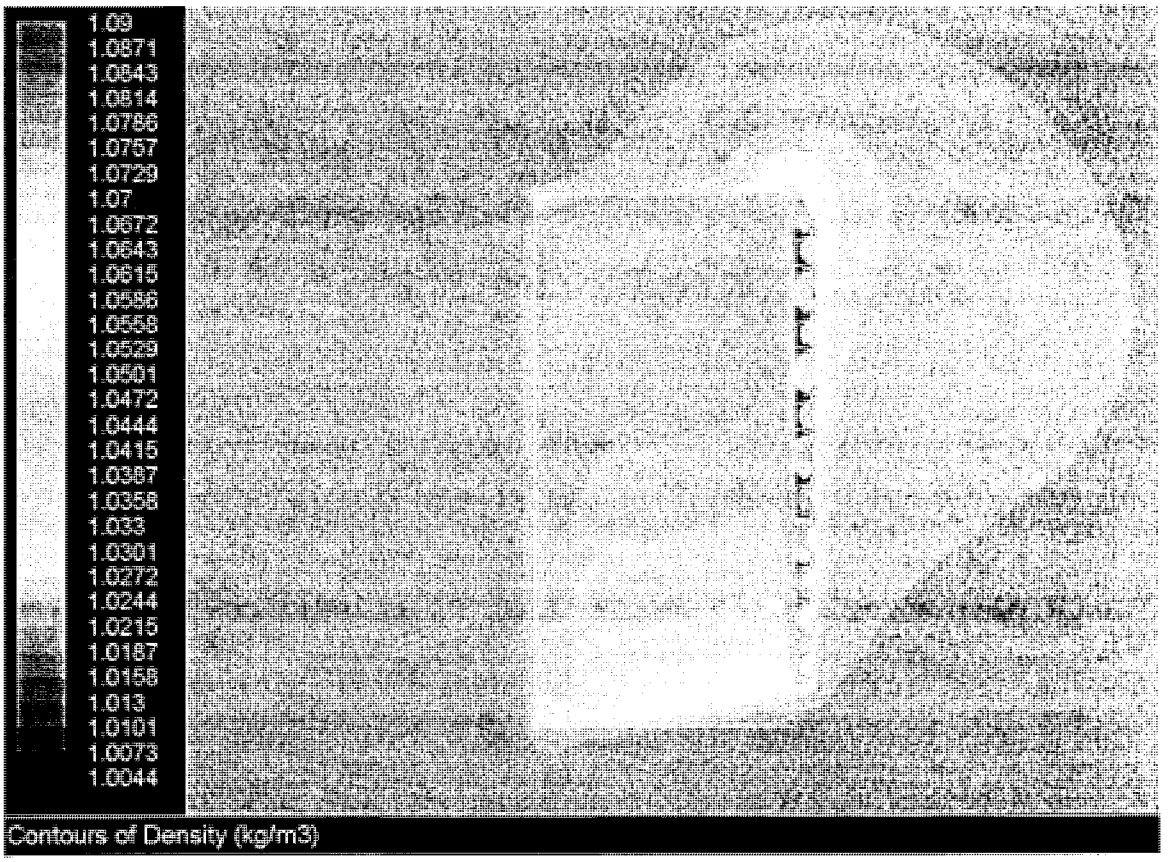

Figure 15. Density profile in kg/m^3 for chamber at 15 degrees elevation angle.

Figure 15 makes sense because the air was being modeled as an ideal gas. The pressure didn't change significantly which made density a function of temperature. Figure 16 shows the velocity magnitude profile for the domain.

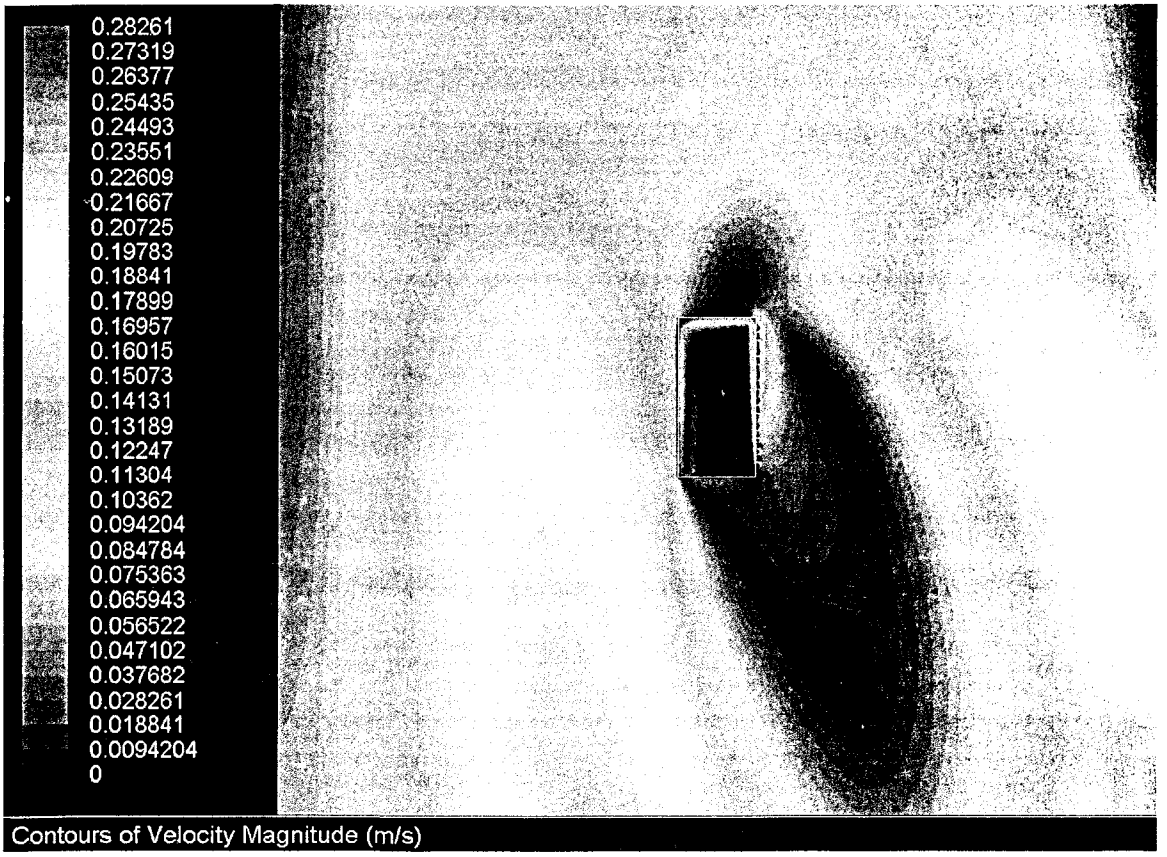

Figure 16. Velocity magnitude profile for the domain.

The air flow was initially set to a very low value around 0.001 m/s. The focus here is assuming no wind so the air flow is due to natural convection. Figures 17 and 18 show a velocity vector plot at the chamber. Velocities inside the chamber were fairly low in most of the chamber but near the edges it was much higher to a

maximum of 0.2 m/s. Outside the chamber the velocities along the heat sinks were higher at around 0.3 m/s.

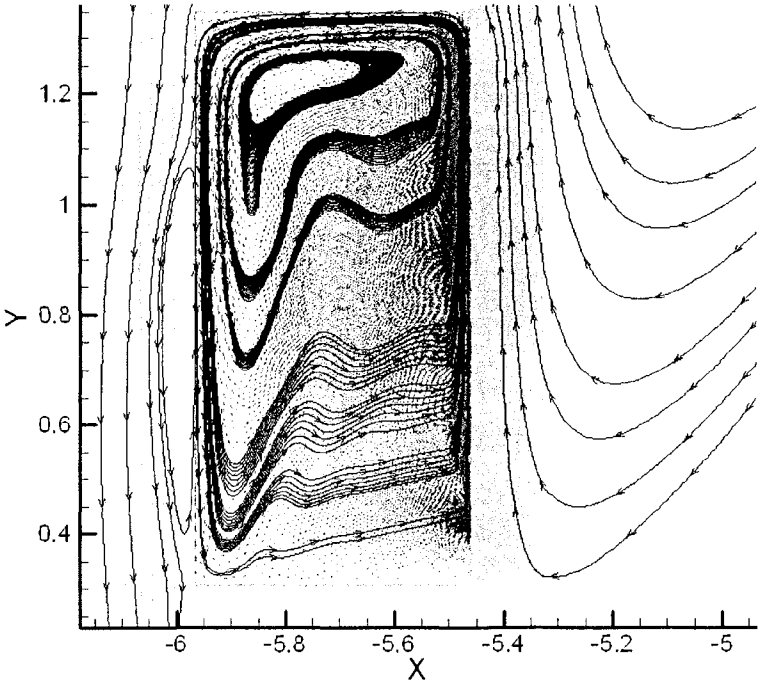

Figure 17. Velocity vector plot.

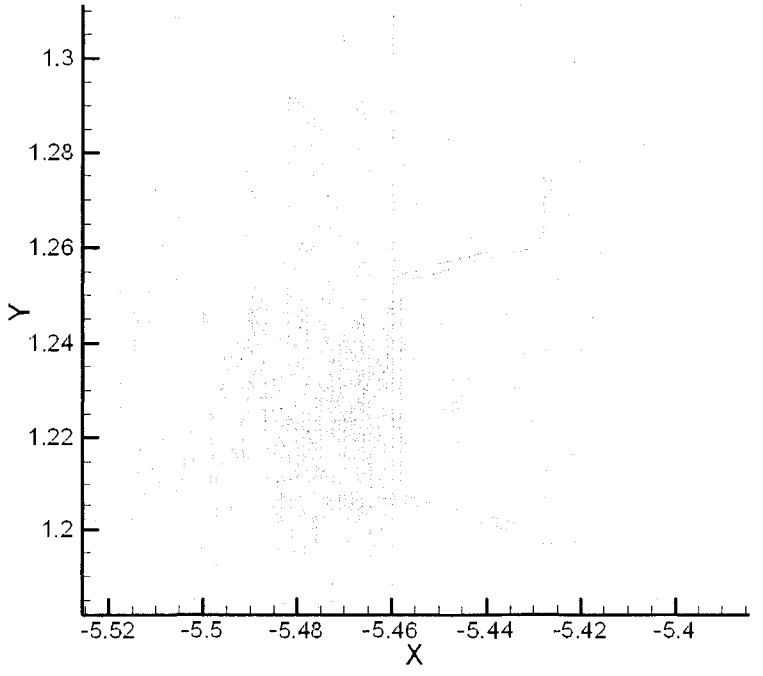

Figure 18. Velocity vector plot close-up.

CHAPTER 2

EXPERIMENTAL SETUP

Candlestick Sensors

Testing on the Amonix system was done several times with a few different methods. During the July month of 2007 and January month of 2008, candlestick sensors were placed in several locations both inside and outside of the test chamber (See Figure 19) [7]. These sensors measure both air temperature and air velocity 9 millimeters from the surface where the sensor is mounted.

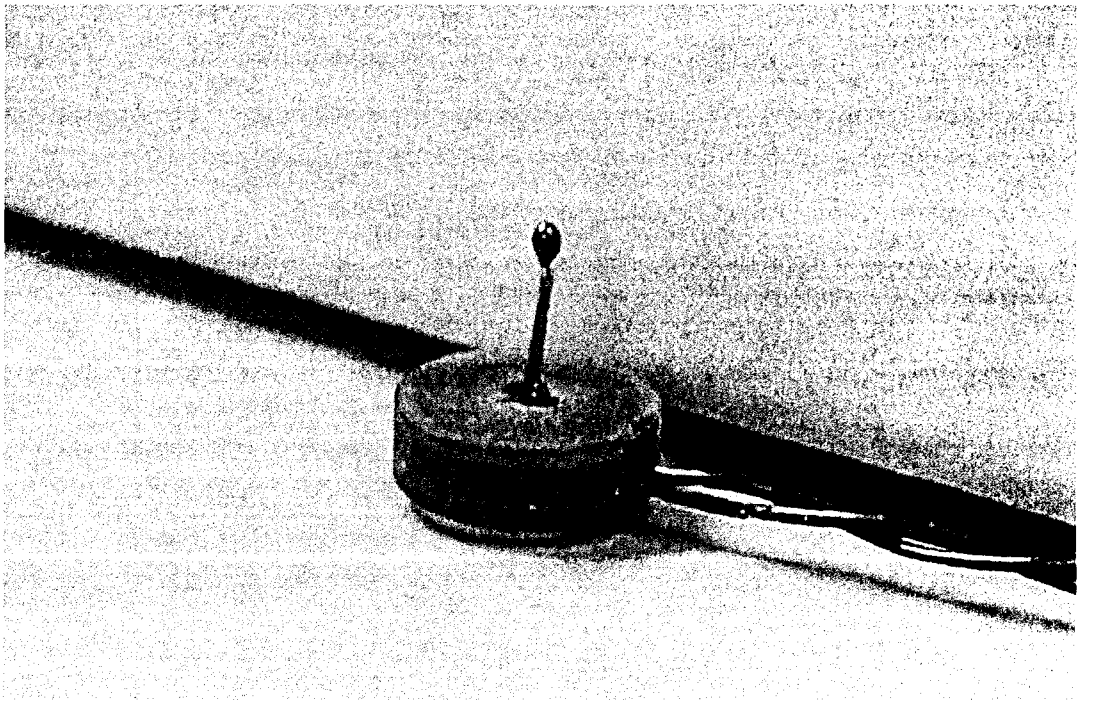

Figure 19. Image of candlestick sensor labeled T5 and V5 inside chamber.

Figure 19 shows one of the candlestick sensors that was inside the test chamber. It was mounted to the very top and was given the label T5. Testing was done over a period of a day and a half. The placement of these sensors can be seen in Figure 20.

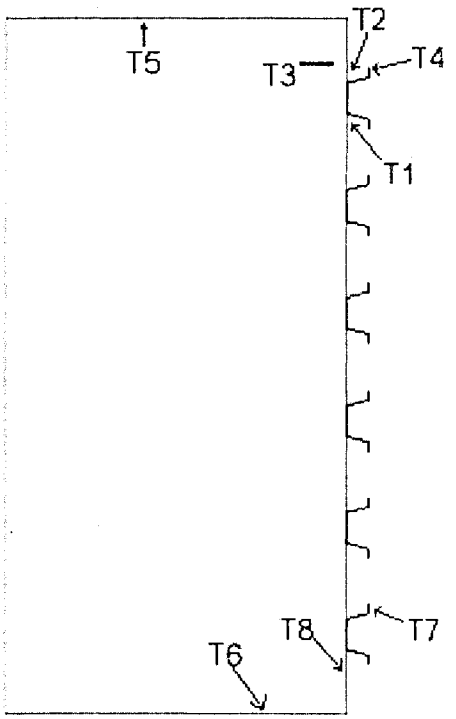

Figure 20. Candlestick sensor placement and identification.

Each of the sensor labels corresponds to places where both temperature and air speed were measured. The temperatures are called T1 and so on while the air speeds are called V1 and so on. The sensor placement and labeling are consistent for the January and July tests. However, some of the sensors were damaged in the field and were not used in the January experiment. These points were picked along with heat fin and several backplate areas to compare with the model predictions.

Thermal Camera

More testing was done in January 2008 using the same sensors along with a thermal imaging camera by FLIR. The thermal camera uses predetermined emissivity values to calculate temperature [8]. Initially it was attempted to take a picture of the entire back plate but problems were discovered. One problem was the fin's emissivity was different from the back plate's emissivity. Another problem was that light from outside sources interfered with the picture and temperature calculation. This occurred especially from sunlight reflections from the ground back onto the bottom of the Amonix megamodules. See Figures 21 and 22 for examples of this.

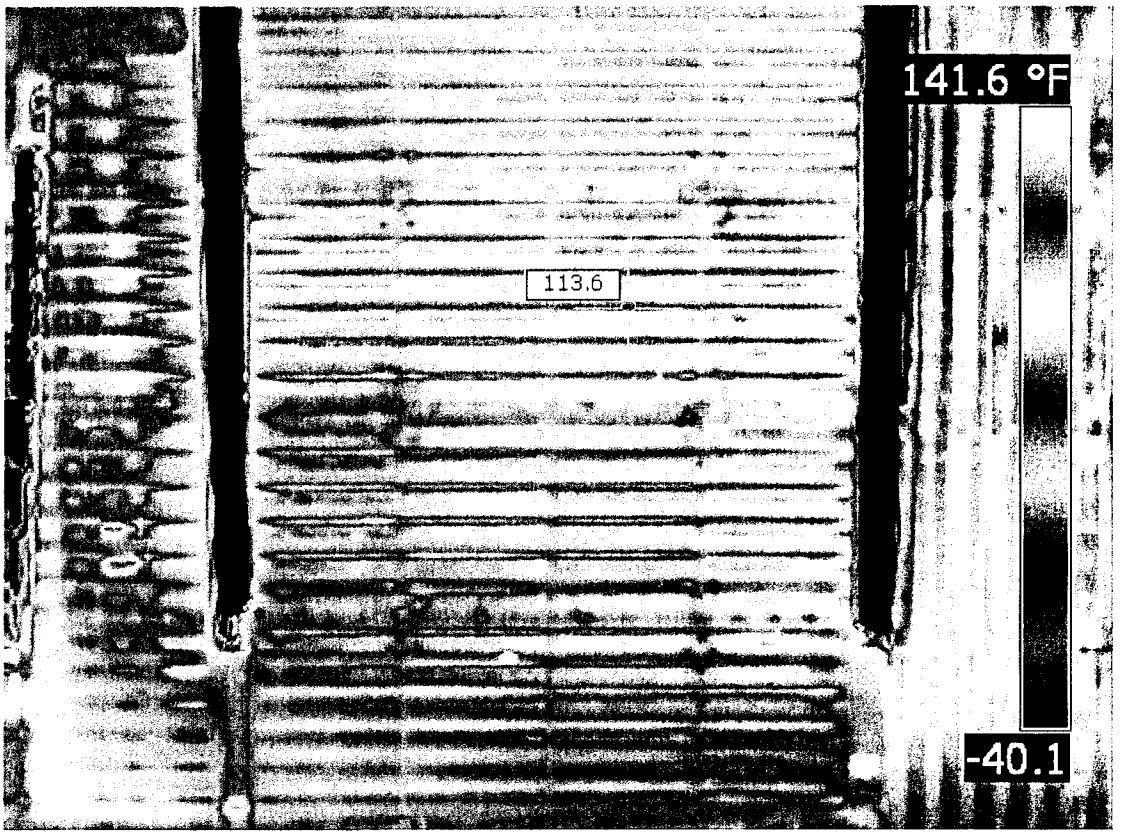

Figure 21. Thermal image of an Amonix mega-module.

Figure 22. Thermal image of my reflection on an Amonix back plate.

Figure 21 inaccurately shows that it is much hotter on the bottom of the module than toward the top. In addition to this, Figure 22 shows that reflections or emissions from other sources including people standing nearby and cars driving in the background could be clearly seen in the image which distorts the camera's intended purpose. In order to negate these latter effects a PVC and black felt structure, nicknamed the Obelisk, was created. The structure was fairly long because the camera would not be able to see the entire backplate unless it was around 10 feet from the backplate. (See Figure 23)

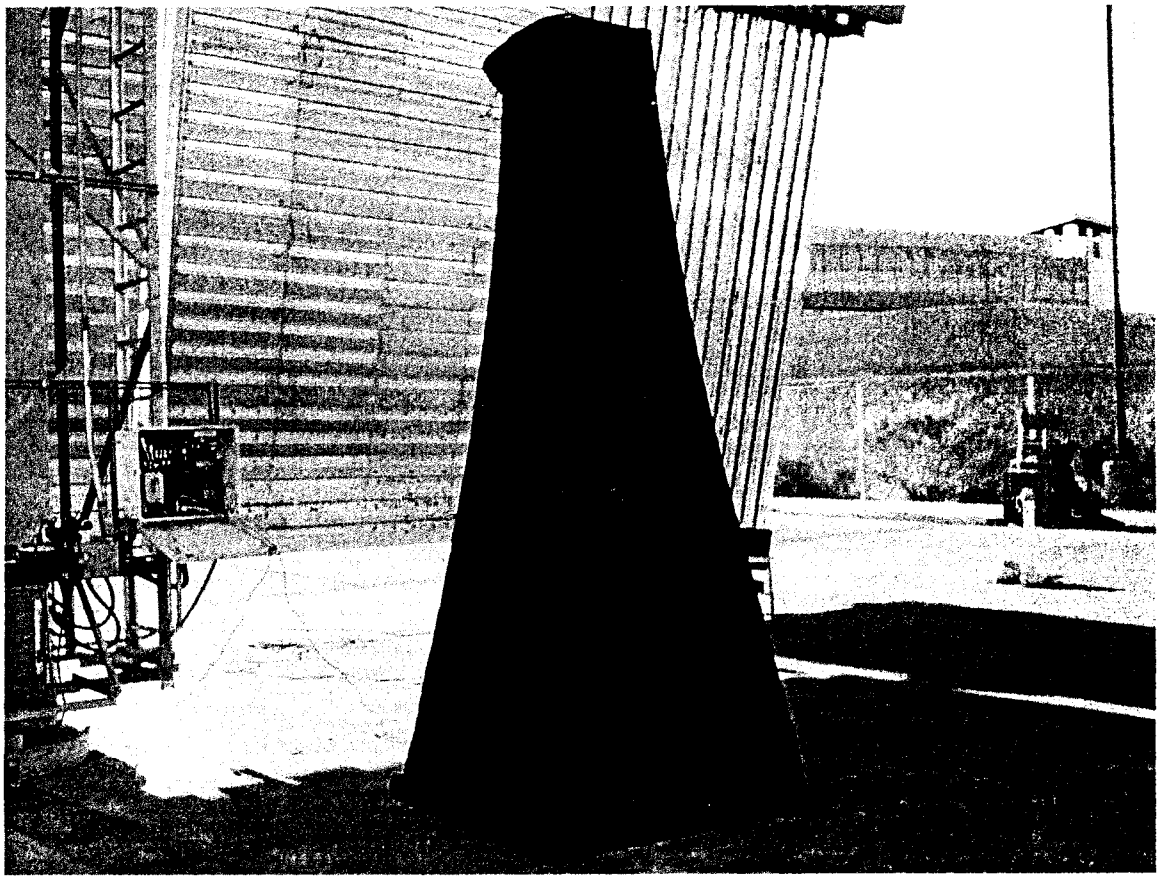

Figure 23. Image of the Obelisk.

The Obelisk blocked incoming light and ensured that only light emitted from the backplate made it to the camera. The first problem with differing emissivities was bypassed by placing black electrical tape with a known emissivity on any place where a temperature measurement was desired [8]. This method of temperature measurement was very quick and gave a large area measurement of temperatures for the entire backplate (see Figures 24 and 25). The data from both of these sources were then compiled and later compared with the model predictions.

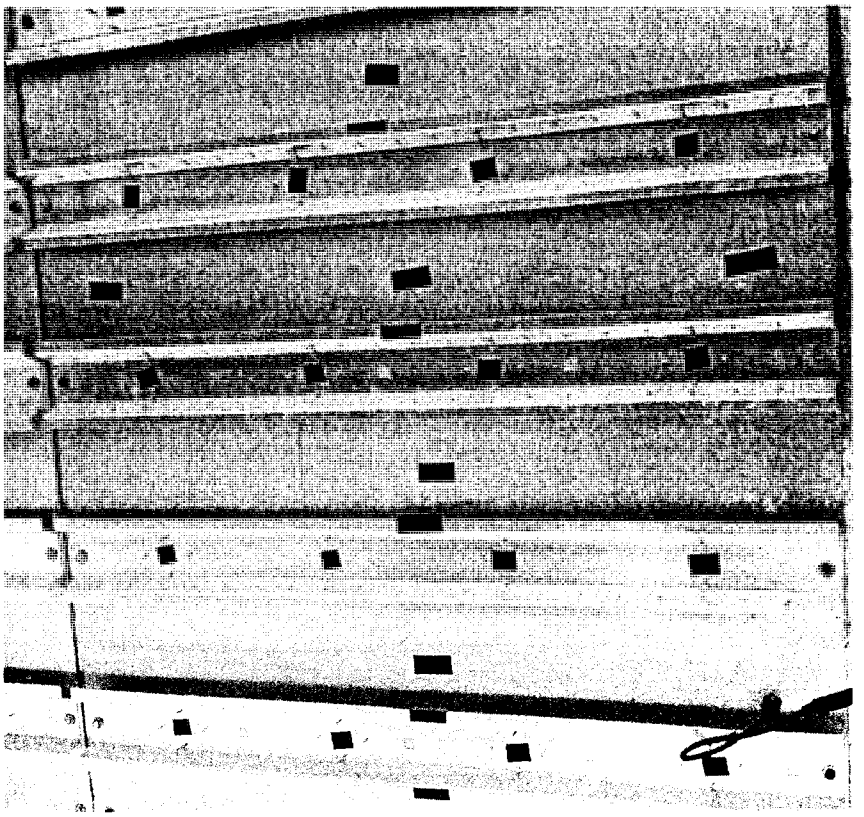

Figure 24. Back plate with electrical tape placed on points of interest.

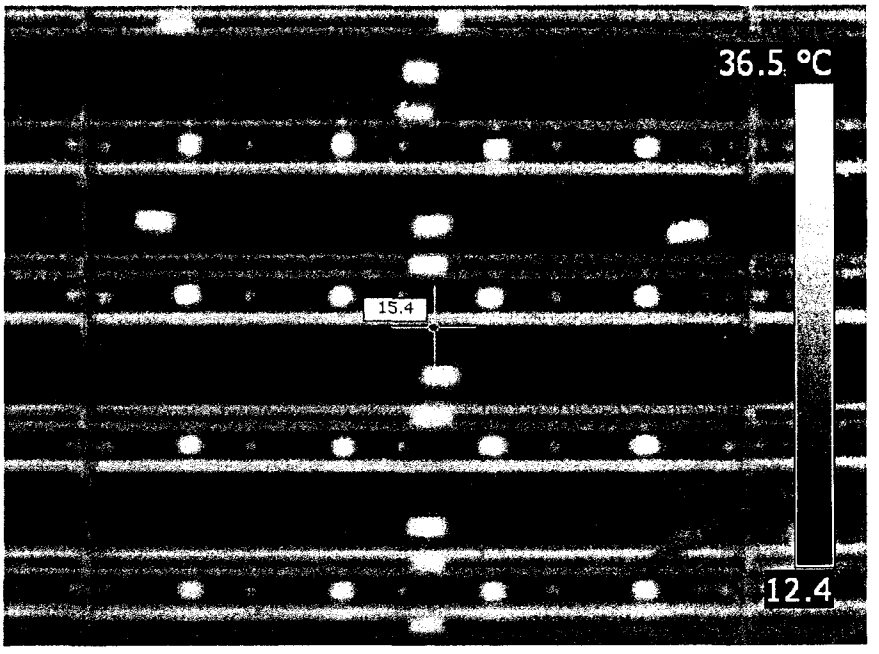

Figure 25. Thermal image of backplate with electrical tape.

CHAPTER 3

JANUARY 2008 CASE

Convection Model

On January 18, 2008 tests were performed on three chambers. One chamber used the candlestick sensors while the other two were used for thermal imaging. Ambient parameters at certain points throughout the test were picked in order to run a simulation and compare with experimental results. The maximum temperature predicted is of the most interest because it is the limiting factor in producing power. As the temperature of the cell increases the voltage decreases and since the cells are connected in series, the cell with the lowest voltage will limit the power produced for that plate. The initial temperatures and velocities were calculated with the following input parameters in Table 3. They were calculated with an assumed initial cell efficiency of 25%.

Table 3. January input parameters for model.

Time	DNI (W/m^2)	Ambient Temperature (K)	Elevation Angle
8:44	776	278.774	18
9:46	860	280.13	26
10:32	901	281.17	30
12:12	910	283.69	33.2
13:12	883.9	284.78	30.25
14:39	796.4	285.67	20.87

Results and Discussion

After including the corrected cell efficiency from the raised cell temperature, it was found that the maximum temperature rose anywhere from 0.07 to less than 1 degree C. For January the cell temperatures were not extremely high and thus did not change the cell efficiency by very much. The largest differences occur around solar noon and later in the day with highest DNI and ambient temperature. The temperature effect should play more of a role in July when the ambient temperatures are much higher. Table 4 shows the differences made by calculating the cell efficiency and re-running the model with the new efficiency.

Table 4. January predicted maximum temperatures with cell efficiency.

Time	1st iteration Max Temperature	2nd iteration Max Temperature	Difference	Calculated Cell Efficiency
8:44	303.372	303.445	0.073	23.76%
9:46	306.963	307.492	0.529	23.49%
10:32	309.241	309.853	0.612	23.34%
12:12	312.252	312.968	0.716	23.14%
13:12	312.782	313.285	0.503	23.12%
14:39	311.276	311.766	0.49	23.22%

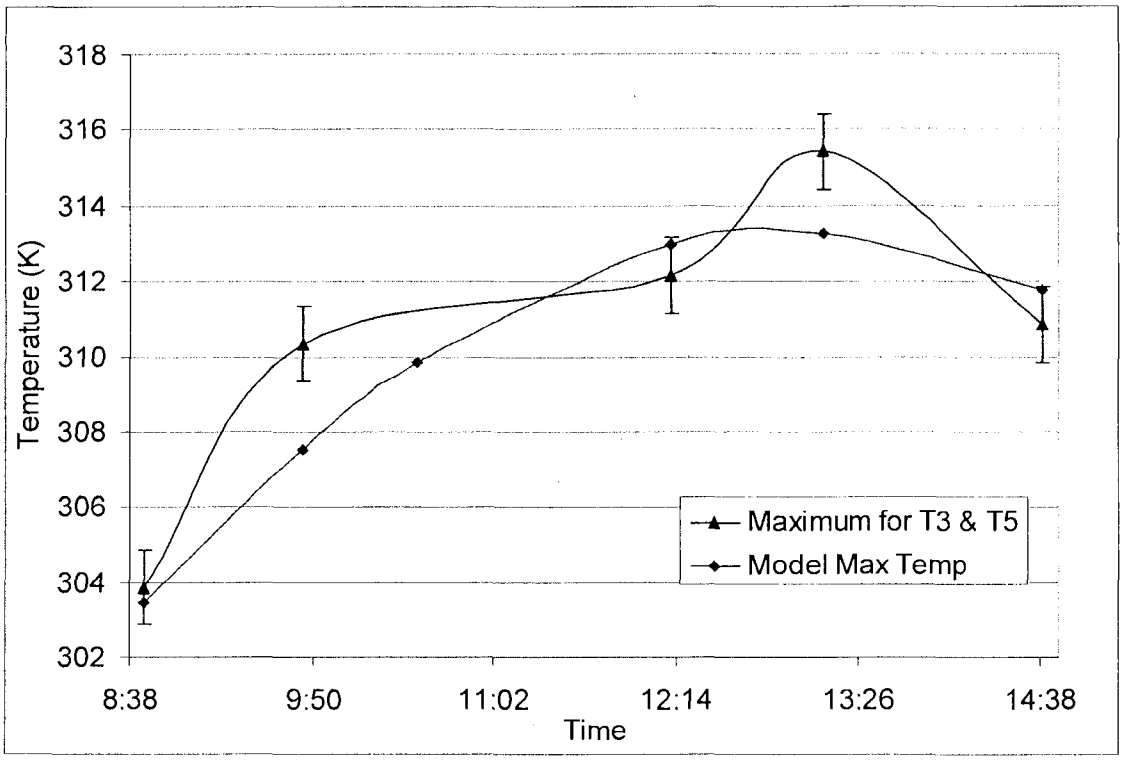

Figure 26. Maximum temperatures predicted with T3 and T5 for Jan.18th, 2008.

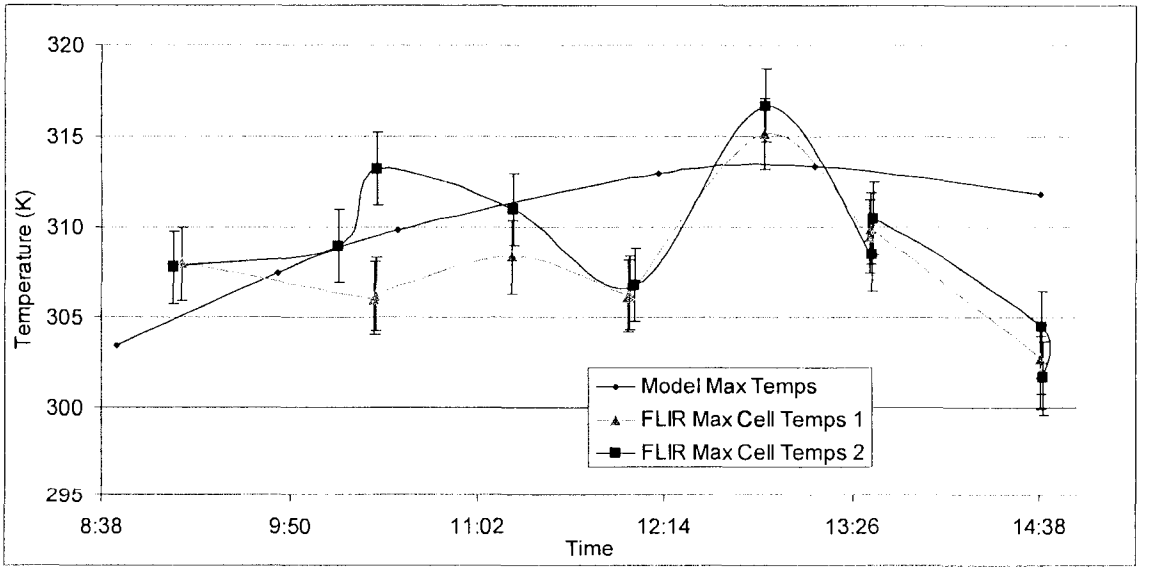

Figure 27. Maximum temperatures predicted vs. measured thermal camera for Jan. 18th, 2008.

Figures 26 and 27 show the maximum temperatures measured compared with the models maximum predicted temperatures. Both locations T3 and T5 were inside the chamber and are not the highest temperatures but should be close to it. Throughout the simulation ambient temperature increases and DNI peaks with elevation angle around 12:12 PM. A trend found in the model was the increase in temperature with the increase in elevation angle. This will be more apparent in the July model discussed later. The next figures compare temperature data between experimental and model data to outer chamber points listed in Figure 20.

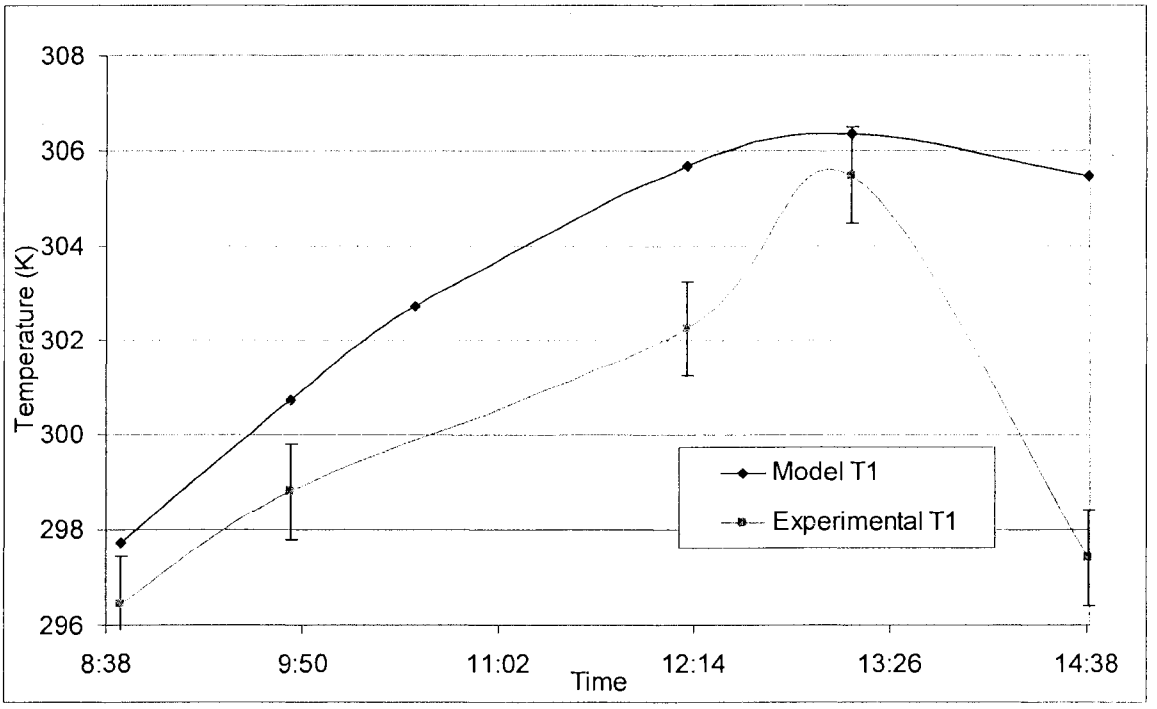

Figure 28. Temperature comparisons at T1 for Jan. 18th, 2008.

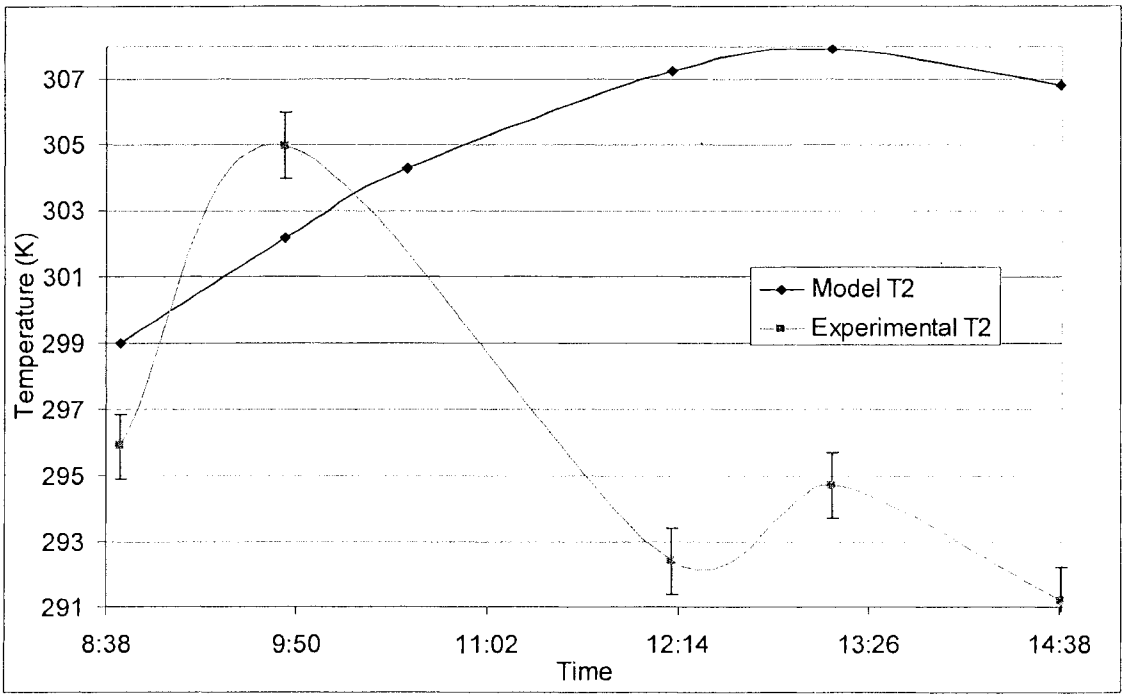

Figure 29. Temperature comparisons at T2 for Jan. 18th, 2008.

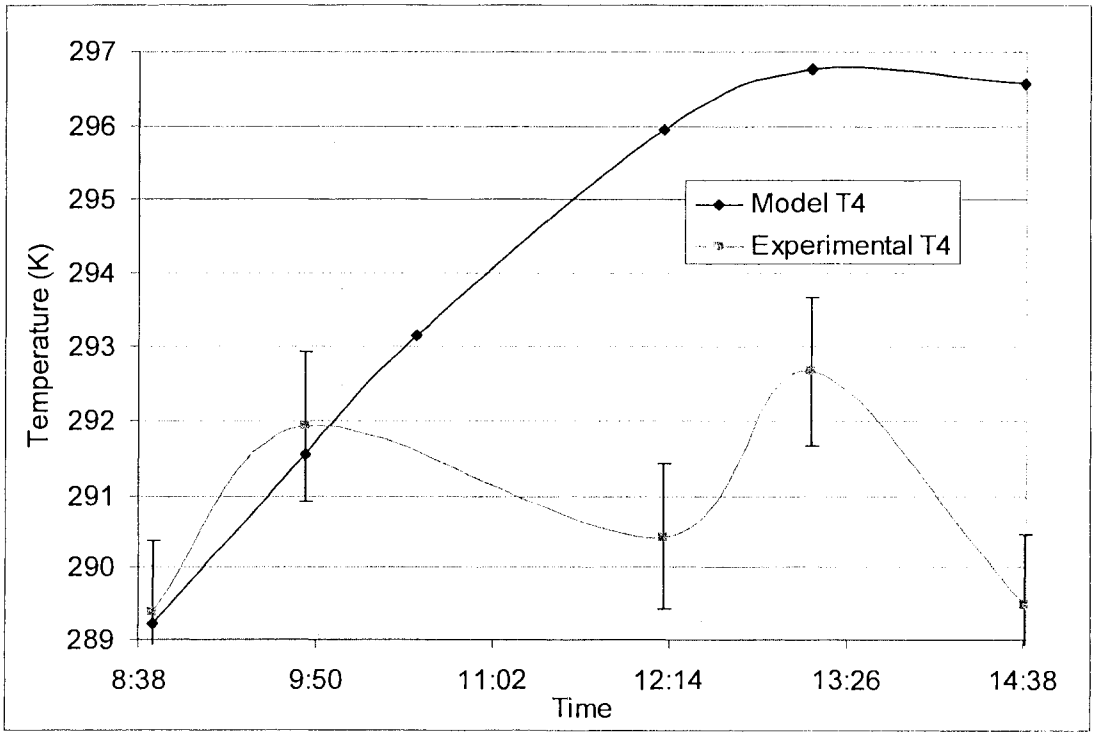

Figure 30. Temperature comparisons at T4 for Jan. 18th, 2008.

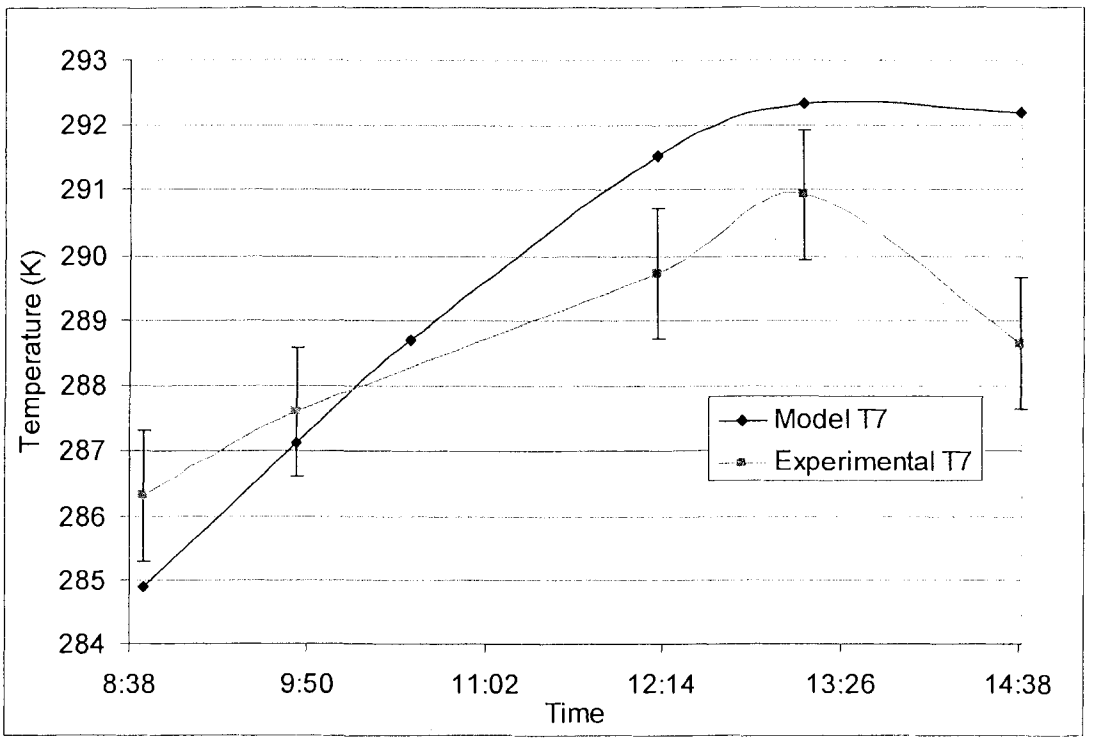

Figure 31. Temperature comparisons at T7 for Jan. 18th, 2008

The outer chamber predictions were very close and were within a degree or two in the morning which is within the instruments error range (±1° C). Later, though, the experimental temperatures rise but not as much as predicted. This is especially apparent in Figures 29 and 30. The difference is mostly due to wind fluctuations throughout the day which would have a cooler backplate compared to a backplate with no wind. This point will be discussed in the air velocity section later. The inner chamber temperatures are shown in the next several figures.

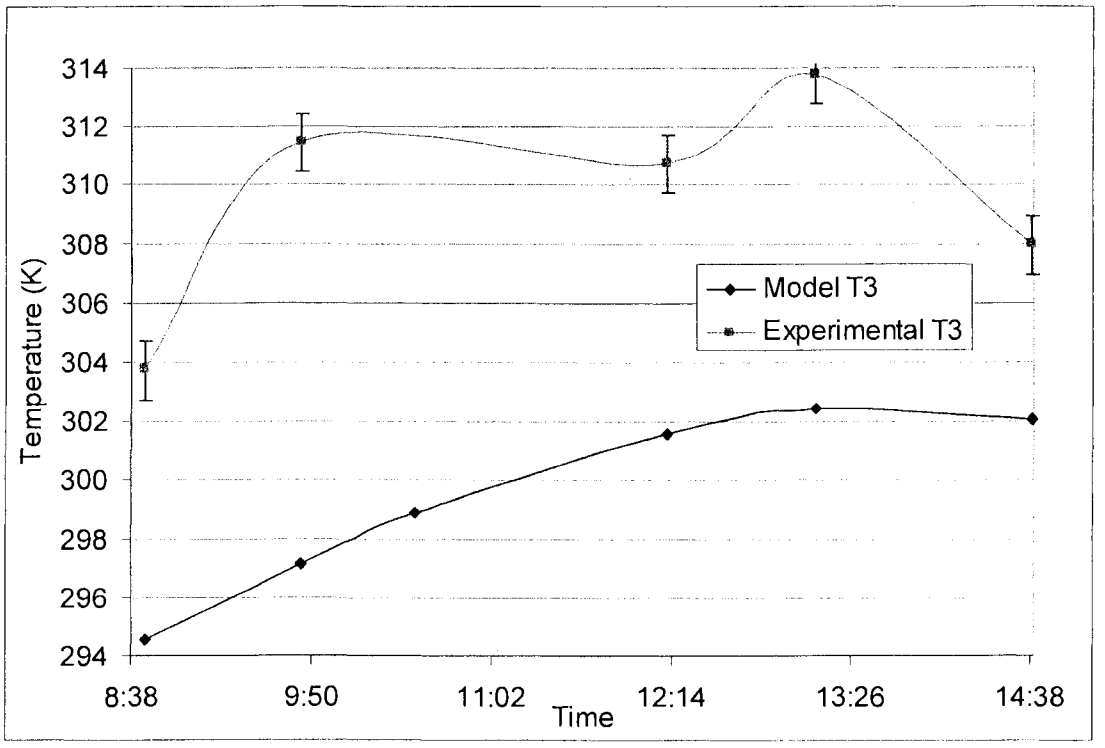

Figure 32. Temperature comparisons at T3 for Jan. 18th, 2008.

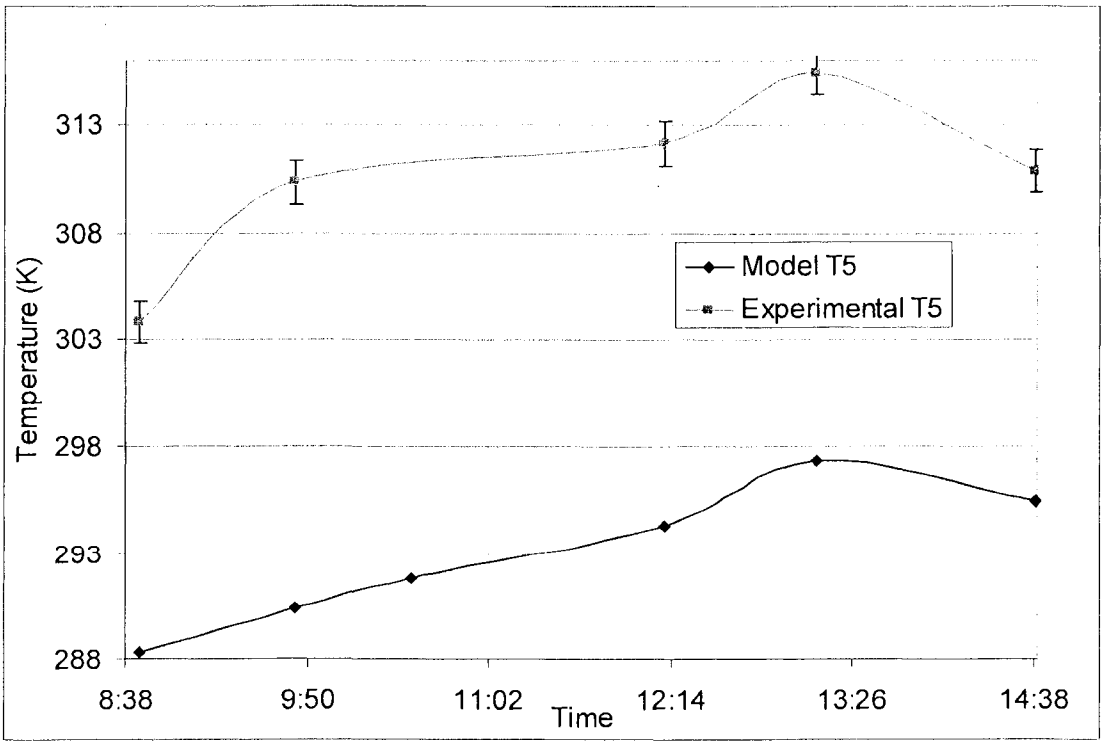

Figure 33. Temperature comparisons at T5 for Jan. 18th, 2008.

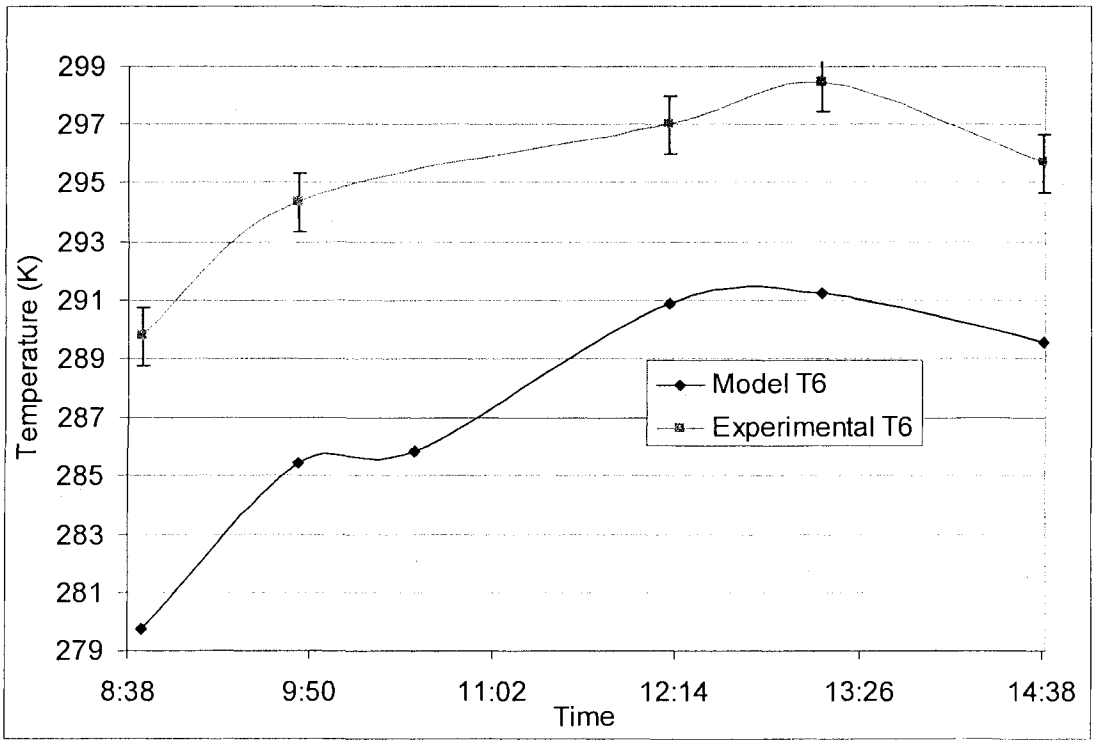

Figure 34. Temperature comparisons at T6 for Jan. 18th, 2008.

As can be seen in Figures 32 through 34, inner chamber predictions were several degrees cooler than measured. The predicted chamber temperatures should be lower due to its treatment as a single chamber with all sides exposed to the ambient. Differences at T3 may be due to inaccurate air velocity predictions because of not including the cell package in the model. This might be possible if the air velocities pull heat off of the cell and plate in a different direction because of the cell package obstructing the flow. Also, global horizontal irradiance was not taken into account in this model and neither was radiation exchange from the ground. Wind also makes a very complicated problem in that it does not always provide a cooling effect depending upon which direction it is blowing against the unit. If the wind speed is sufficient, it can rock the unit back

and forth which will move the beam and give a non-uniform flux on the cells as well as increase the reflectance on the surface of the lens [9]. This will lower the efficiency and raise the temperatures of the cells. It is expected that when the radiation model is used, the temperatures will be even lower since the heat will be given another avenue in which to leave the system. Attempts to investigate these differences will be dealt with later on. The outer chamber velocity plots can be seen in Figures 35 through 38.

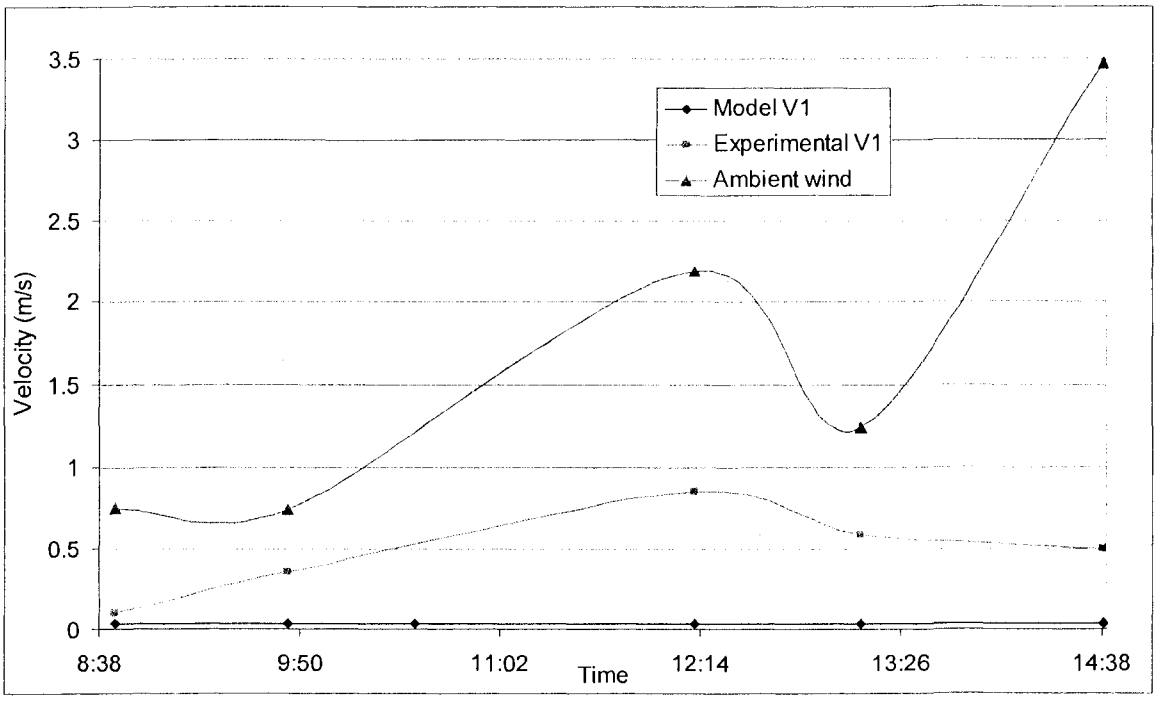

Figure 35. Velocity comparison for V1 with ambient wind for Jan. 18th, 2008.

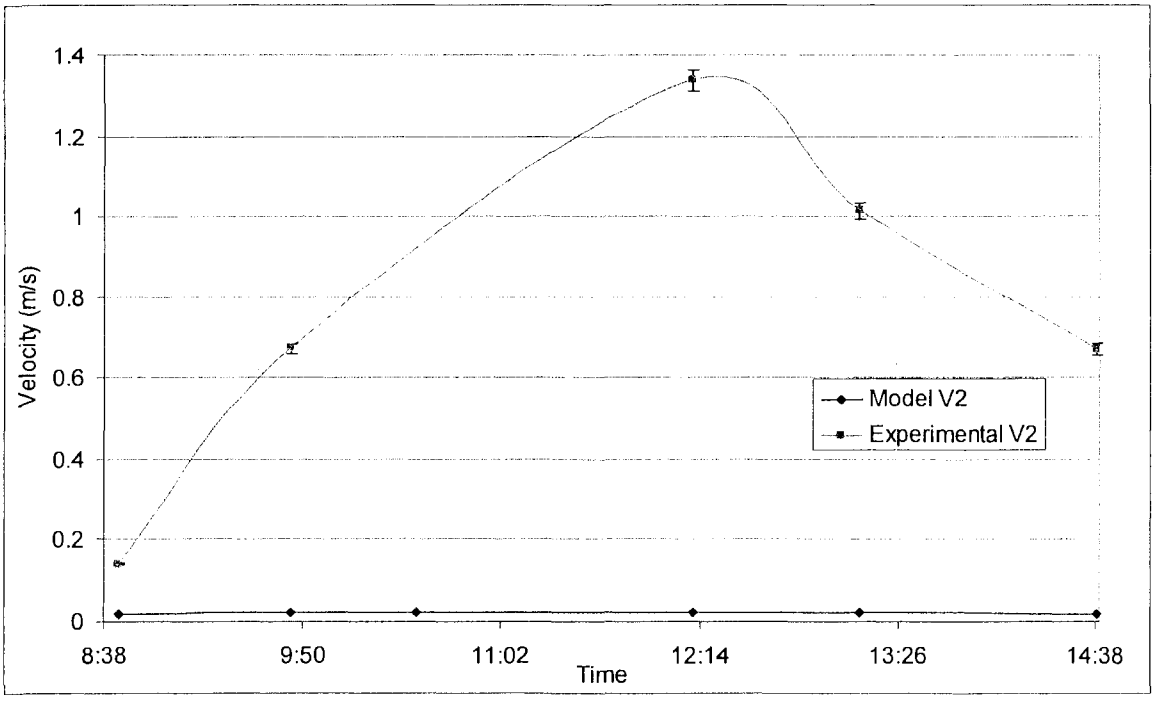

Figure 36. Velocity comparison for V2 for Jan. 18th, 2008.

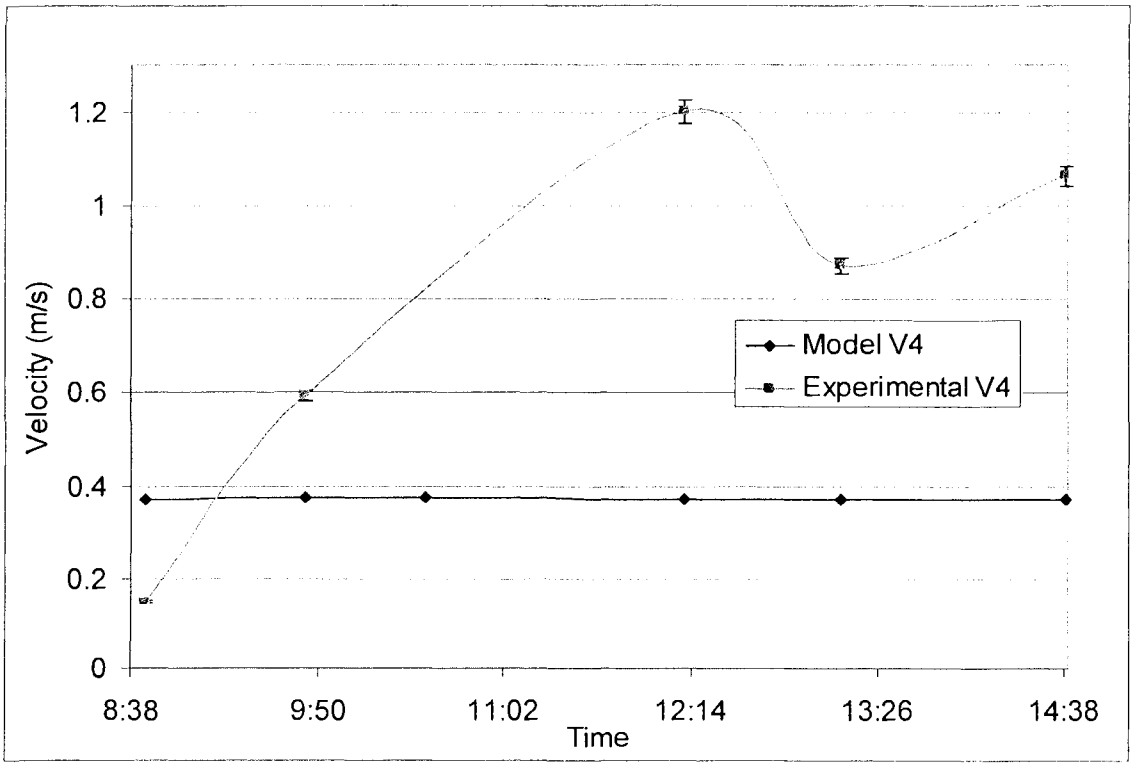

Figure 37. Velocity comparison for V4 for Jan. 18th 2008.

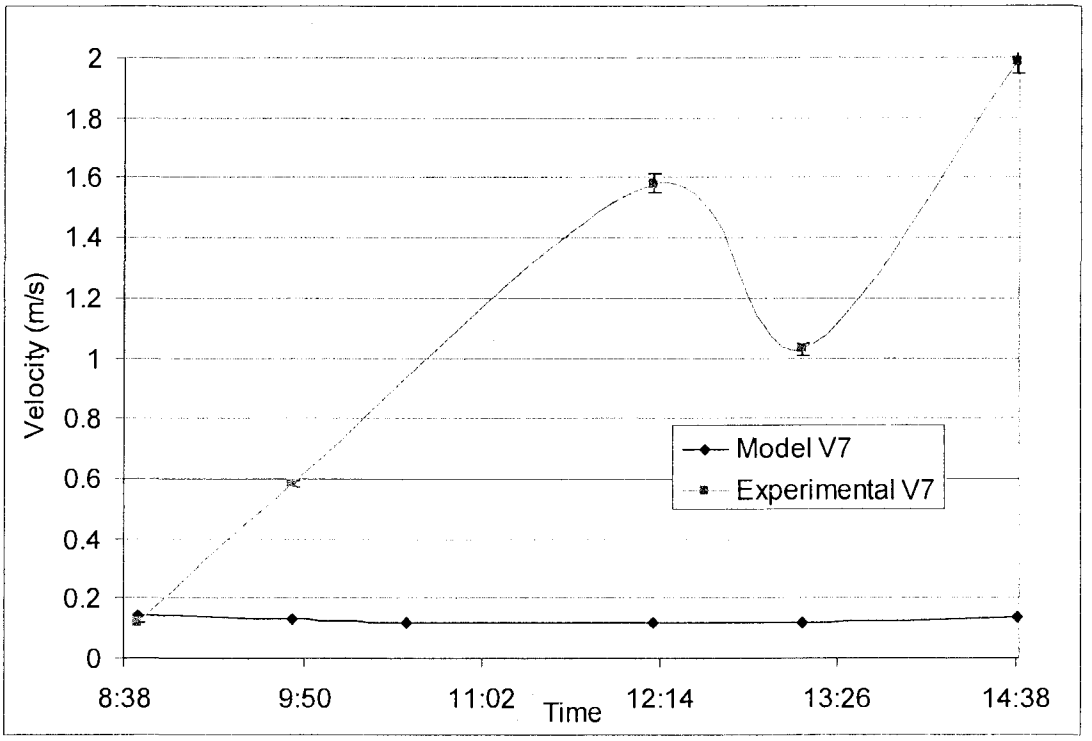

Figure 38. Velocity comparison for V7 for Jan. 18th 2008.

The outer chamber velocities were clearly affected by ambient wind, so much so that it is not of much value to compare these points in this case except for the explanation of cooler temperatures at these points. The sensors have error ranges of ±2%. The inner chamber velocities can be seen in Figures 39, 40, and 41. Many of the velocities are so small that the error bars do not appear in many of the figures. The model over predicted the air velocity at V3 while under predicting it at V5.

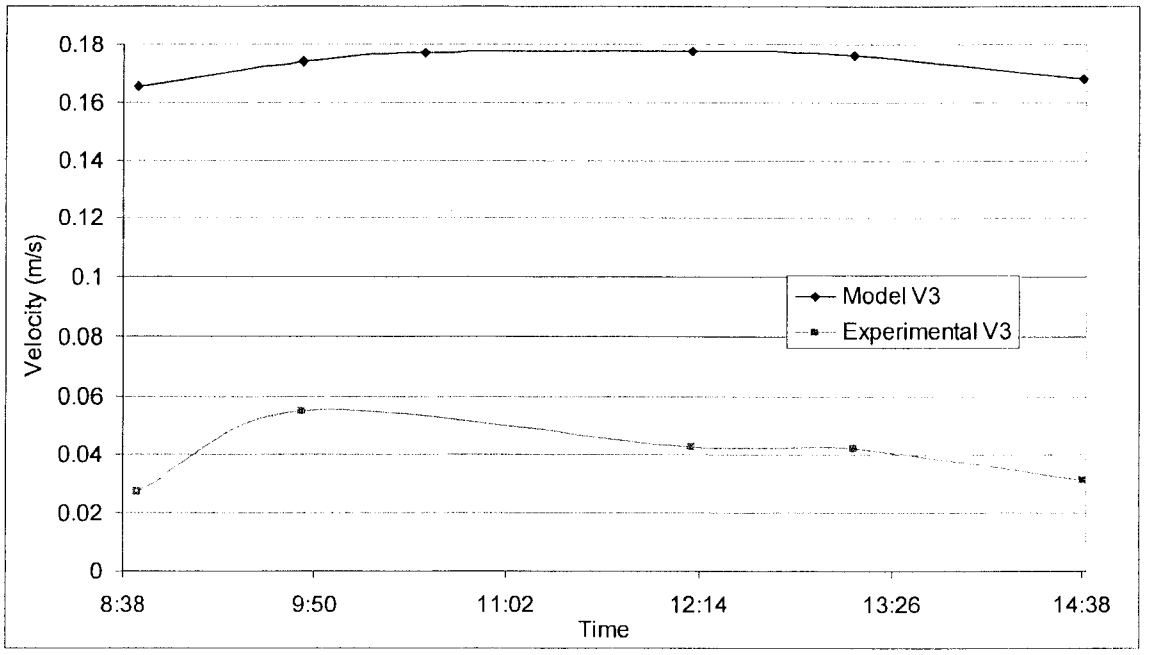

Figure 39. Velocity comparison for V3 at Jan. 18th, 2008.

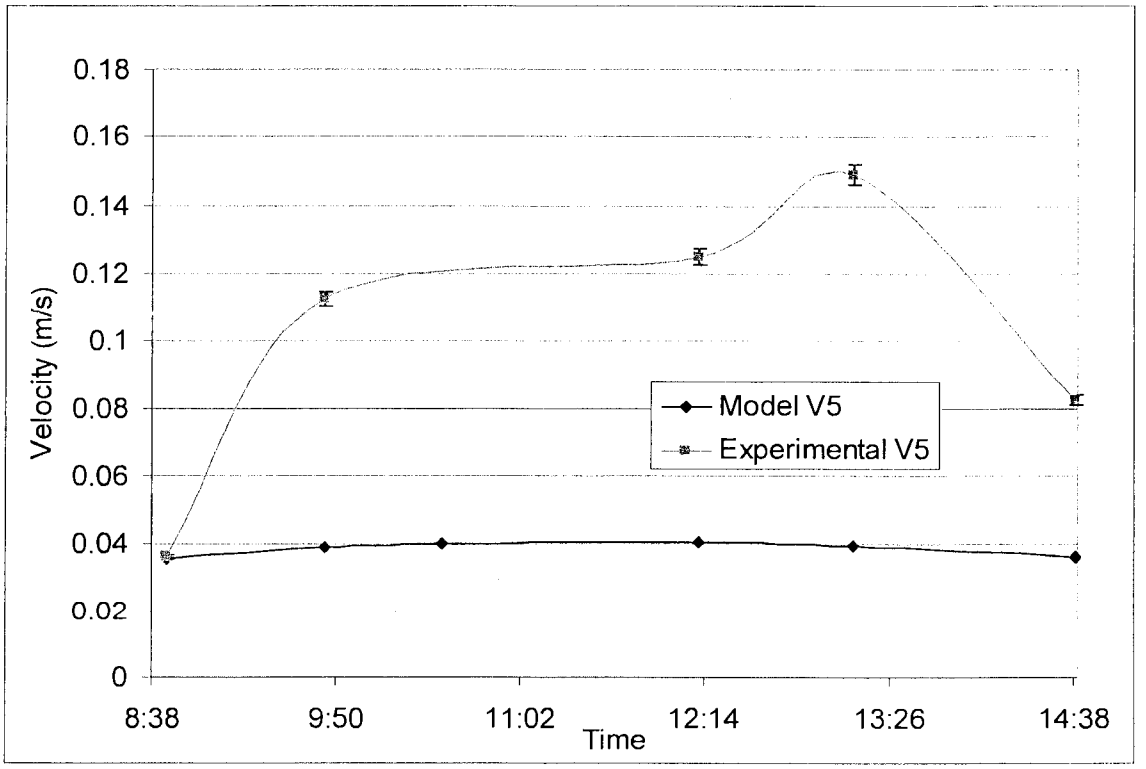

Figure 40. Velocity comparison for V5 for Jan. 18th, 2008.

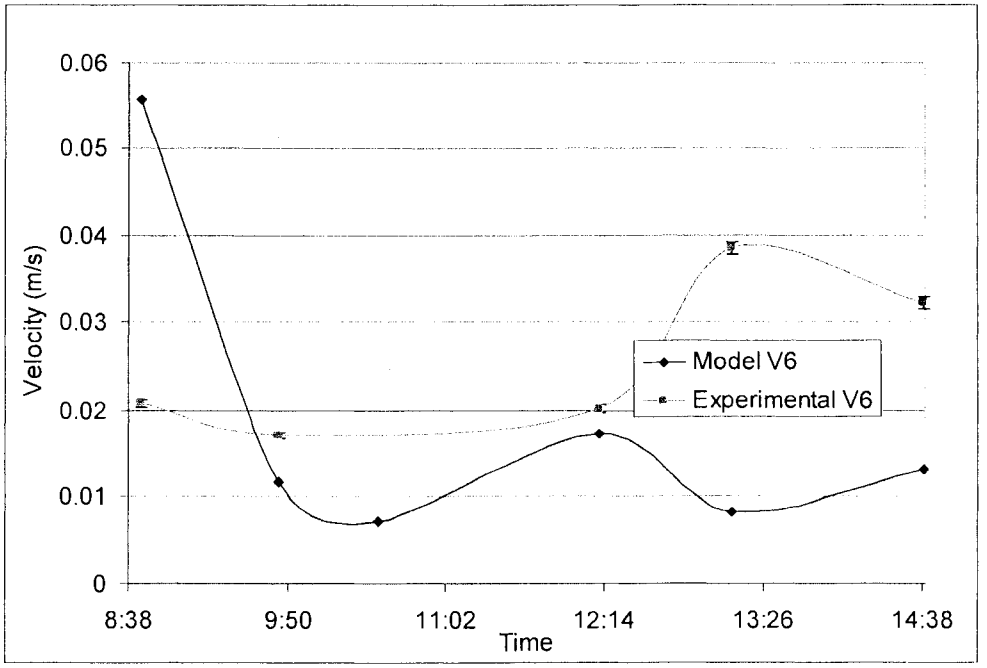

Figure 41. Velocity comparison for V6 for Jan. 18th, 2008.

The inner chamber velocities, although much closer compared to the outer chamber velocities, are still quite different in most cases. The predictions are at least in the ballpark range. Also the real chamber is not sealed as in the model. There is air flow between chambers on the sides and the model does not incorporate the cell package which will obstruct the flow of air. The percentage difference between the measured temperatures and the temperature predictions for the convection model can be seen in Table 5.

Table 5. Convection model percentage difference for January 18th, 2008 test.

Time	DNI	T_{inf}	Angle	T1	T2	T3	T4	T5	T6	T7
8:44	776	278.774	18	0.091%	0.713%	2.712%	0.000%	4.801%	3.126%	0.142%
9:46	860	280.13	26	0.315%	0.586%	4.286%	0.000%	6.122%	2.694%	0.000%
12:12	910	283.69	33.2	0.172%	3.699%	3.503%	1.559%	6.221%	3.428%	0.272%
13:12	883.9	284.78	30.25	0.000%	3.901%	3.574%	1.049%	6.388%	2.201%	0.140%
14:39	796.4	285.67	20.87	2.657%	5.367%	1.467%	2.102%	4.039%	1.169%	0.880%
Average	**845.26**	**282.609**	**25.664**	**0.647%**	**2.853%**	**3.108%**	**0.942%**	**5.514%**	**2.523%**	**0.287%**

In terms of percentage, the difference was fairly low with a maximum of about 5.5% and many cases were less than 1%. Now the model will be compared with the thermal camera results. Figure 42 shows the cell temperature predictions.

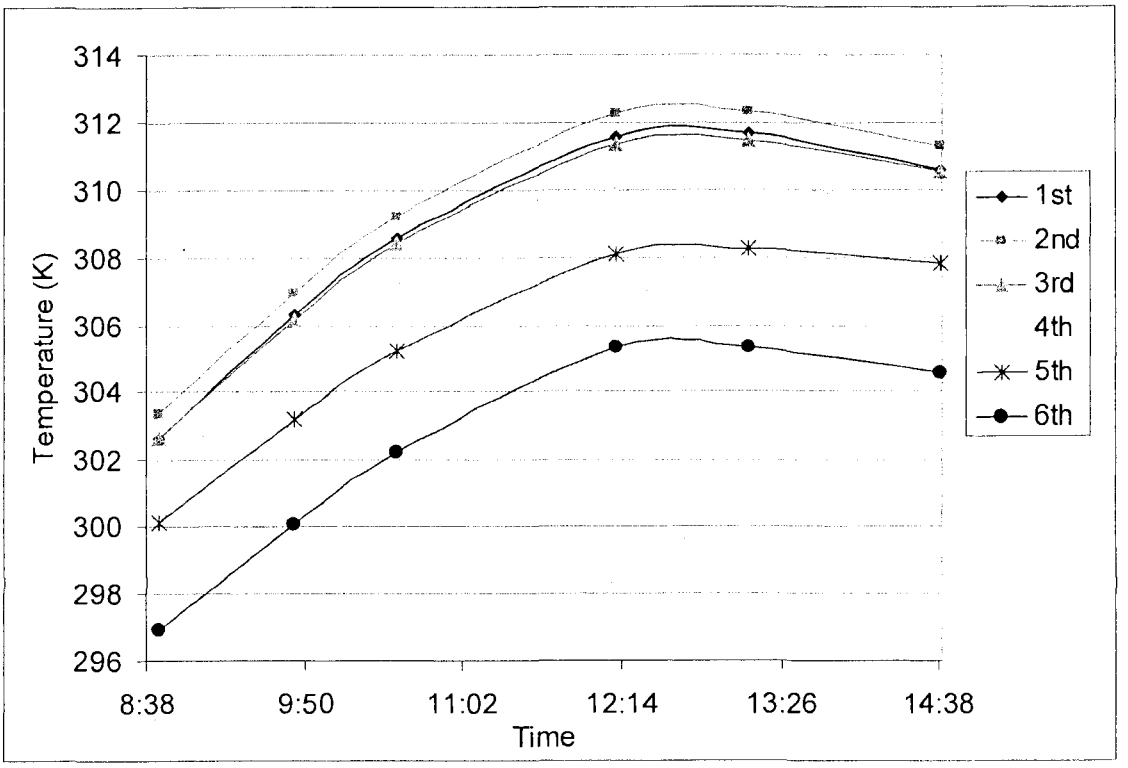

Figure 42. Cell temperature predictions for Jan. 18th, 2008.

Figure 43 shows the measured back plate cell temperatures and the results are compared to model predictions in Figure 44. The cells are measured from top to bottom meaning the top cell is labeled 1st. Something interesting to note is that the hottest cells were not the ones highest in the chamber but actually the 2nd cells from the top. This was also true in the experimental data although sometimes the cells in the third row were slightly higher than the 2nd and 1st row. This result is due to vortices that develop inside and outside the chamber as

well as the top cell has more material between itself and the top of the chamber to conduct heat away from itself. The latest 6th generation mega module design no longer uses individual chambers with dividers between each back plate. This should completely change the velocity profile inside the module and increase overall flow speeds.

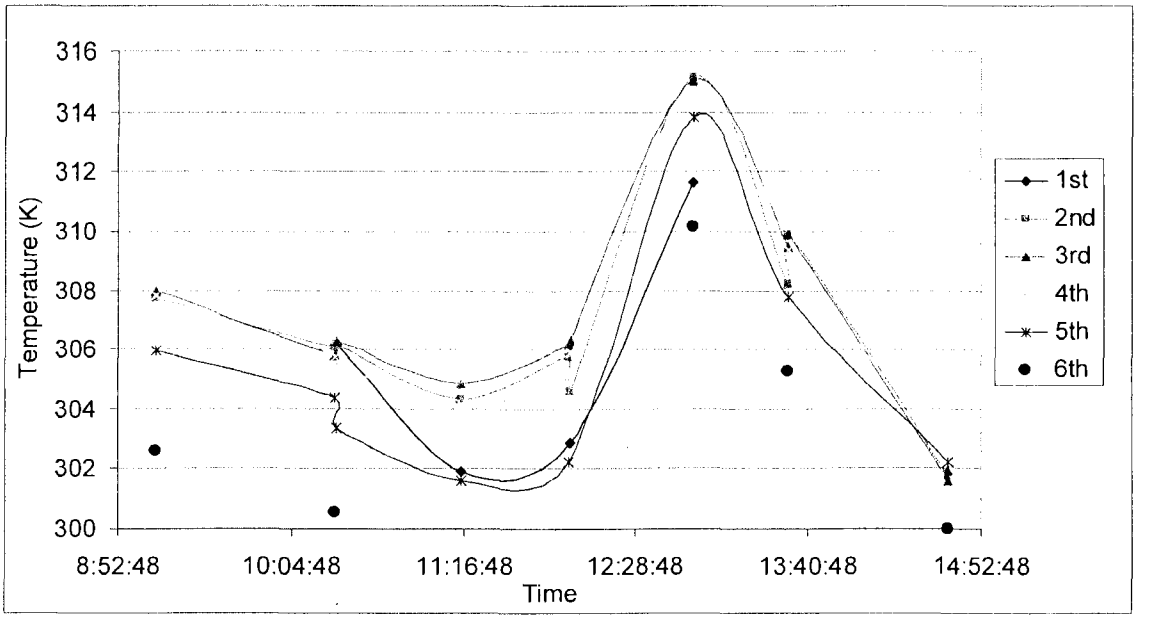

Figure 43. Back plate cell temperatures with thermal camera for Jan. 18th, 2008.

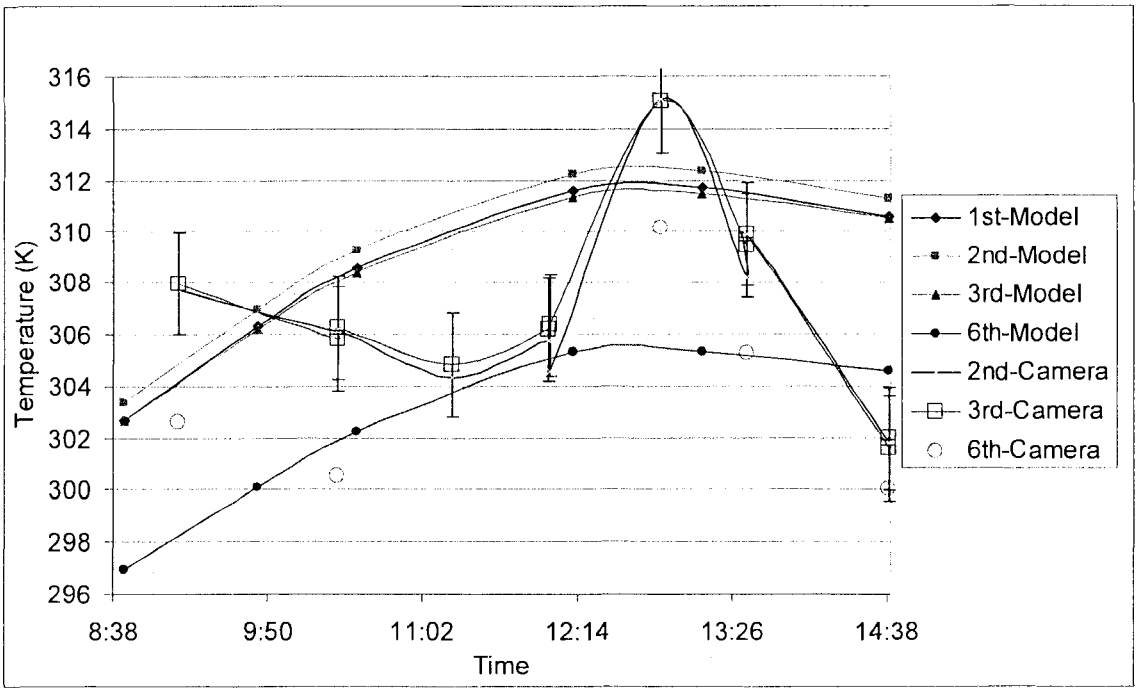

Figure 44. Cell temperature predictions with thermal camera measurements for Jan. 18th, 2008.

Figure 44 compares predicted cell temperatures with thermal camera readings. The error on the thermal measurement was given as ±2° C of reading. Figure 42 shows error bars for the 3rd set of cells. As can be seen in the figure, the model accurately predicted temperatures within the error range in some cases. Again, the reason for the difference in the temperatures is probably due to ambient wind on the system. The system has to be normal to the sun in order to generate power. Because of this it moves both in azimuth and elevation. If the wind is blowing in a certain direction, the change in azimuth will change the angle at which the wind blows on the back of the Amonix system. To check to see if this was the case, average wind speed during these readings were compared with a back plate cell temperature in Figure 45. From this figure it is very clear

that the wind speed has a direct effect on cell temperatures. As the wind speed increased, cell temperatures decreased and vice versa.

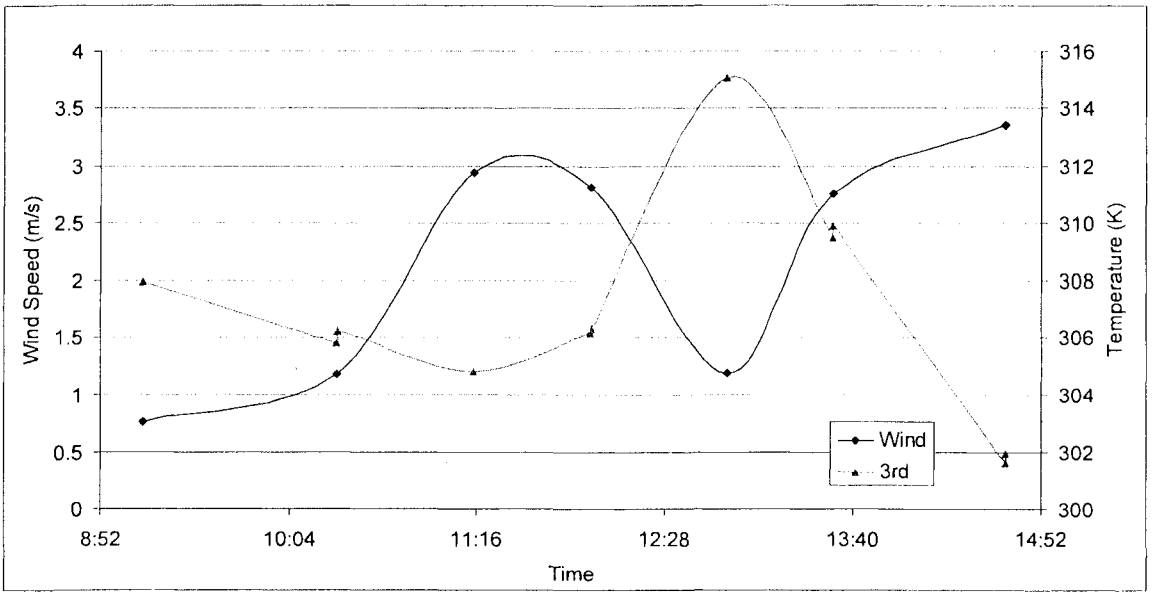

Figure 45. Cell temperature measurements with ambient wind for Jan. 18th, 2008.

Multivariable Regression Analysis

The model's max temperature data was examined with the regression tool in Excel. It was found that very small changes in maximum temperatures lead to very different results in correlating each variable, DNI, ambient temperature, and elevation angle to maximum temperature. In January, the range of values for each variable did not change by very much. This led to negative coefficients for either DNI or elevation angle which is not an accurate equation. The model will have to be run with values of DNI and elevation angle that were not measured in order find the correlations between these two variables and maximum temperature.

The measured data regression analysis showed expected positive coefficients for DNI, elevation angle, and ambient temperature and a negative coefficient for wind speed. The data used was at the location of T3 and this is not the maximum temperature in the field but should be close to it. Figures 46 and 47 show the temperature difference between T3 and ambient temperature over the ambient temperature at a specified DNI and elevation angle. The trend shown from these figures is that as the ambient temperature increases, the difference between the maximum cell temperature and ambient will decrease. This result makes sense because there is a finite amount of heat applied to the cell. As the temperature increases the finite amount of heat will become less and less significant.

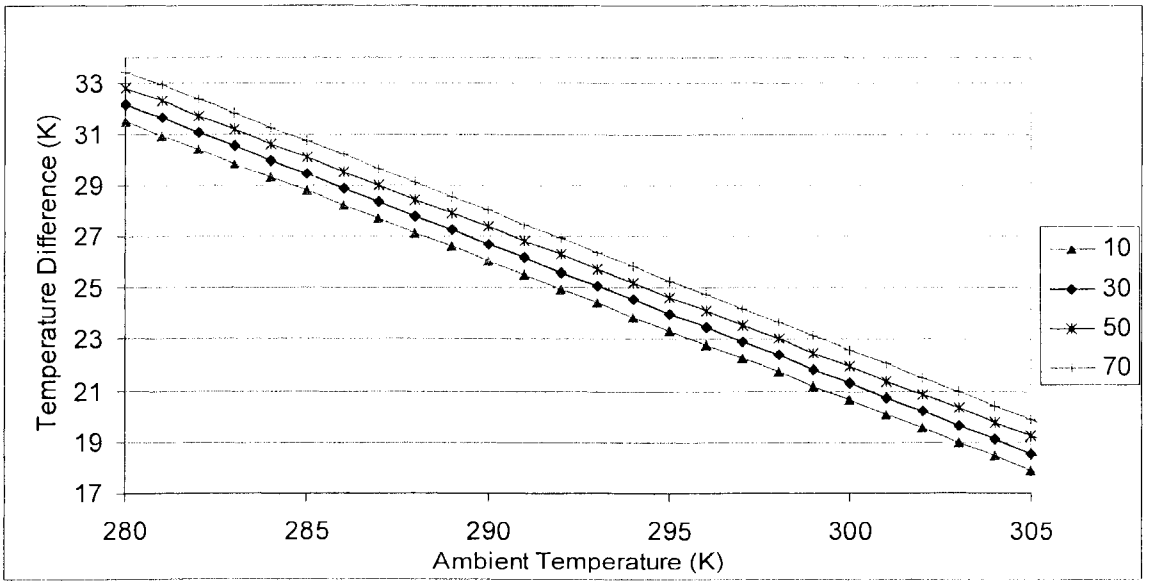

Figure 46. Temperature difference vs. ambient temperature for different elevation angles at 900 W/m^2.

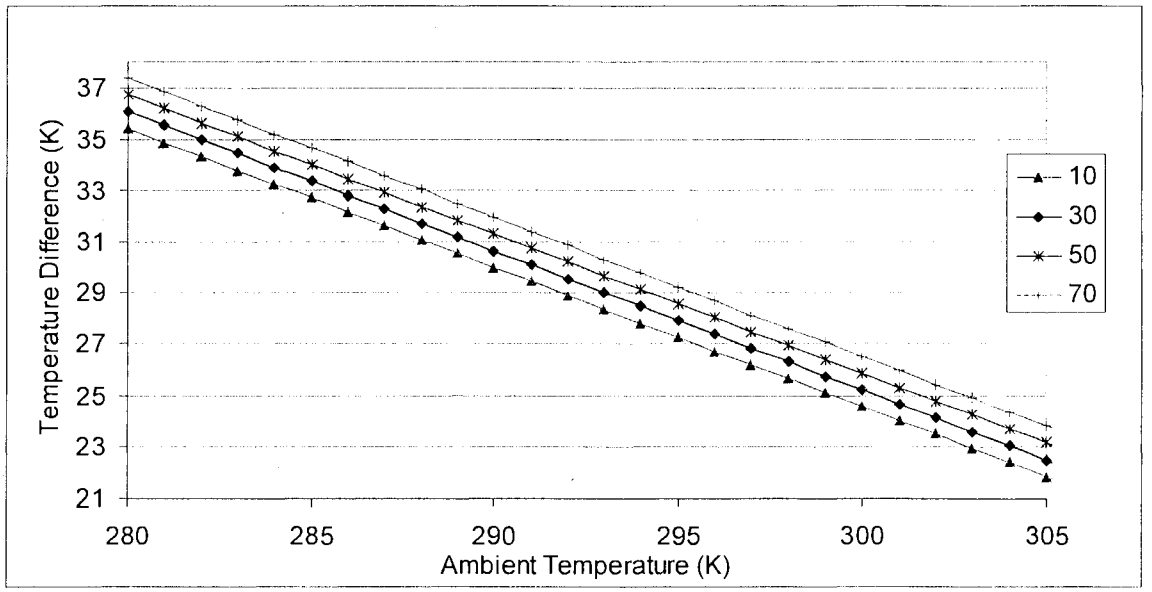

Figure 47. Temperature difference vs. ambient temperature for different elevation angles at 1000 W/m^2.

The equation generated gave a 2 degree difference between a chamber at a 10 degree angle versus a chamber at a 70 degree angle. This was extrapolated for this data since the largest angle is about 33 degrees. This will be interesting to compare to July data since the range of angles are much larger during the summer than in the winter. Something to note, however, is that the DNI measured in the field is not necessarily the same as the DNI striking the Amonix chamber. Tracking errors as well as wind play a role with these curves. July should be a better case for this analysis and will be discussed in the next chapter.

Convection with Radiation Model

The radiation models used were the P1 and the discrete ordinate models. The P1 model assumes that all surfaces are diffuse, which is not exactly the case

here. The optical thickness of the model is large since air does not play a significant role in radiation. The Fluent manual also notes that it tends to over predict radiative fluxes from localized heat sources [10]. On the other hand, the discrete ordinate model can be used to model specular surfaces and semi-transparent walls such as the case with the Fresnel lens. However, the use of this model is very CPU intensive and leads to huge data files for this model, around a gigabyte. Both models were used but the P1 model is used primarily because of its speed. What is of interest here is to see how much the temperatures will drop and whether there is any significant effect on other variables like air velocity. See Figure 48 for a comparison for the numerical model with the P1 radiation model turned on vs. only with the convection model.

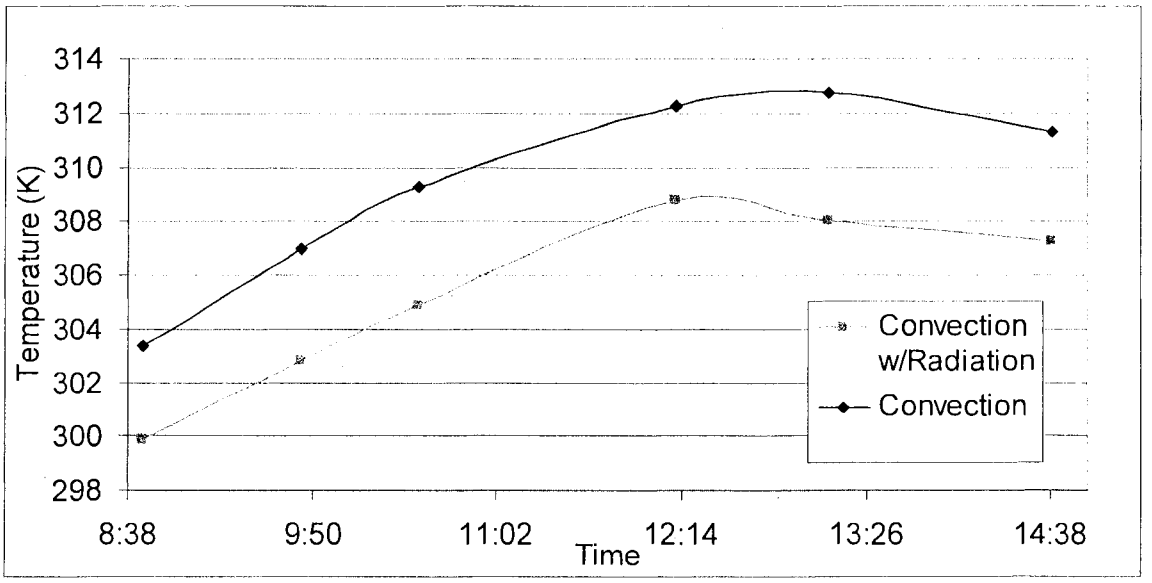

Figure 48. Maximum temperatures for the convection model with radiation vs. pure convection model for Jan. 18th, 2008.

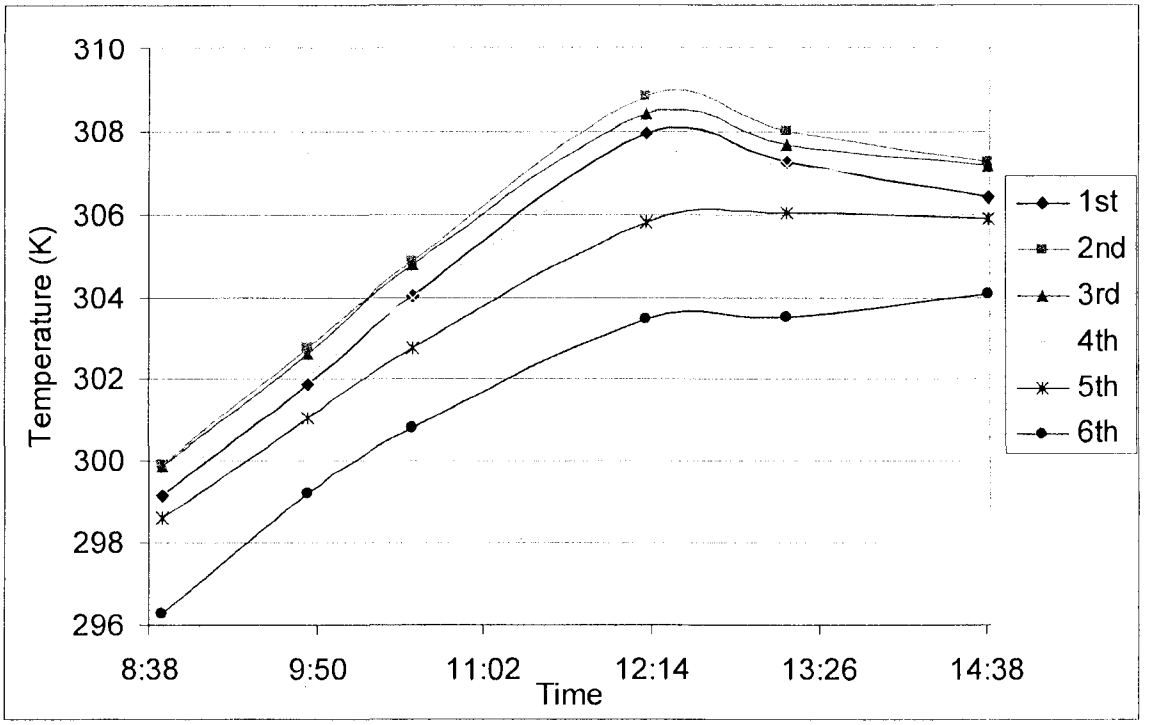

Figure 49. Model with radiation cell temperature predictions for Jan. 18th, 2008.

The average difference between the two models was about 4 degrees C. This decrease was expected but the model does not account for radiation exchange with the ground or global horizontal radiation. This is probably not a major factor in the winter but might be very significant in the summer. The cell temperature predictions with the use of the radiation model can be seen in Figure 49. It is interesting to note that the cells in the first four rows are much closer than with just the convection model. This was seen with the thermal camera images and can be seen in Figure 43. The drop in temperature made the percentage difference somewhat higher in some cases with little change in air velocity. The experimental air velocities for V5 and V6 were much higher than predicted in both models. It is unclear why this is, but it might be due to the chamber not

being sealed. Table 6 shows the percentage difference between measured data and predicted temperatures.

Table 6. Convection and radiation model percentage difference for Jan. 18th, 2008.

Time	DNI	T_{inf}	Angle	T1	T2	T3	T4	T5	T6	T7
8:44	776	278.77	18	0.182%	0.000%	3.171%	0.080%	4.799%	0.879%	0.158%
9:46	860	280.13	26	0.169%	1.879%	4.839%	0.304%	6.180%	1.599%	0.225%
12:12	910	283.69	33.2	0.000%	3.593%	3.108%	1.125%	5.411%	1.237%	0.013%
13:12	883.9	284.78	30.25	0.738%	2.647%	3.922%	0.226%	5.959%	1.219%	0.190%
14:39	796.4	285.67	20.87	1.240%	3.705%	2.124%	1.682%	4.633%	0.366%	0.823%
Average	**845.26**	**282.609**	**25.664**	**0.466%**	**2.365%**	**3.433%**	**0.683%**	**5.396%**	**1.060%**	**0.282%**

CHAPTER 4

JULY 2007 CASE

Convection Model

In this case, the thermal camera was not available and only candlestick sensors were used to measure temperature and air velocity. For this month the ambient temperatures were much higher than in the January. This made the cell efficiency play more of a role in determining cell temperature. In January, an assumption of a 25% efficient cell would be within one degree of the more accurate solution with cell efficiency as a function of temperature. This is not the case in July. In most of the simulations there is about a 3 degree difference between the 25% efficient case and the use of cell efficiency as a function of temperature. Table 7 gives the input parameters for the model.

Table 7. July 19th, 2007 input parameters for model.

Time	DNI (W/m^2)	Ambient Temperature (K)	Elevation Angle
8:23	878	306.2	31.3
9:31	945.8	308.53	45
10:48	972.5	310.29	60
12:46	962.7	312.88	74.6
13:47	947.7	314.19	69.66
15:36	898.9	313.98	50

The inner chamber temperatures are considered first. Figure 50 compares the maximum predicted temperatures to experimental T3. As opposed to the January case, the maximum temperatures in Figure 50 are much larger in most cases when compared to the hottest location measured. See Figures 51, 52, 53, and 54 for the model's predictions for the inner chamber temperatures.

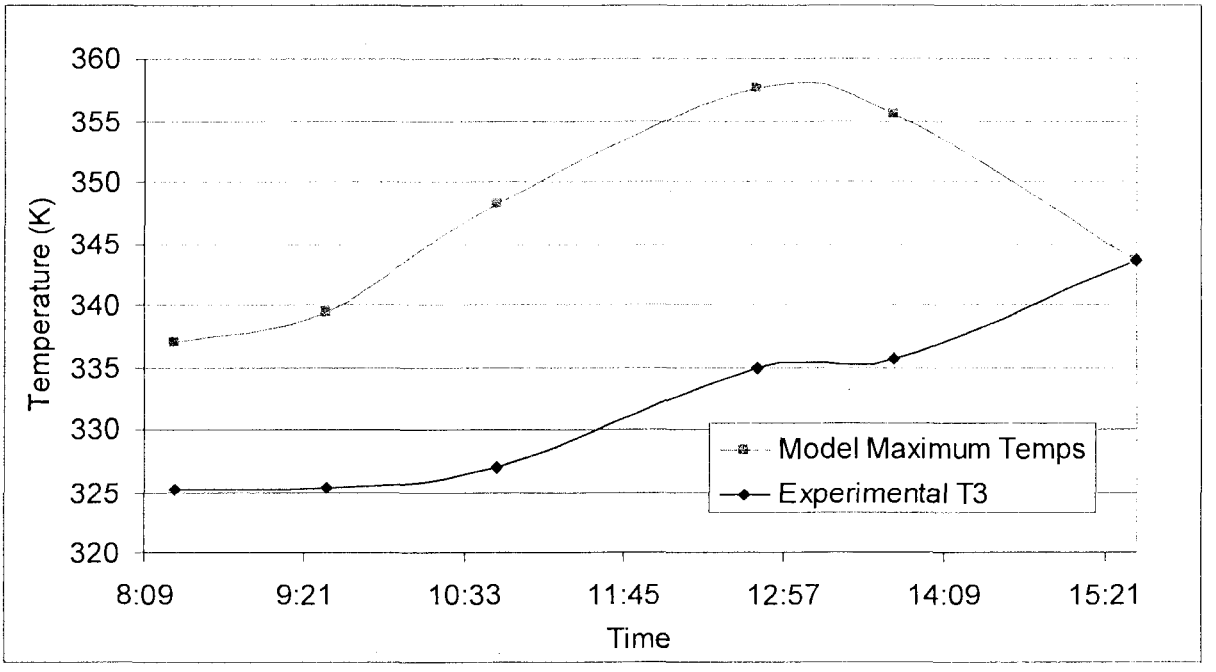

Figure 50. Maximum predicted temperatures vs. maximum measured temperatures for July 19th, 2007.

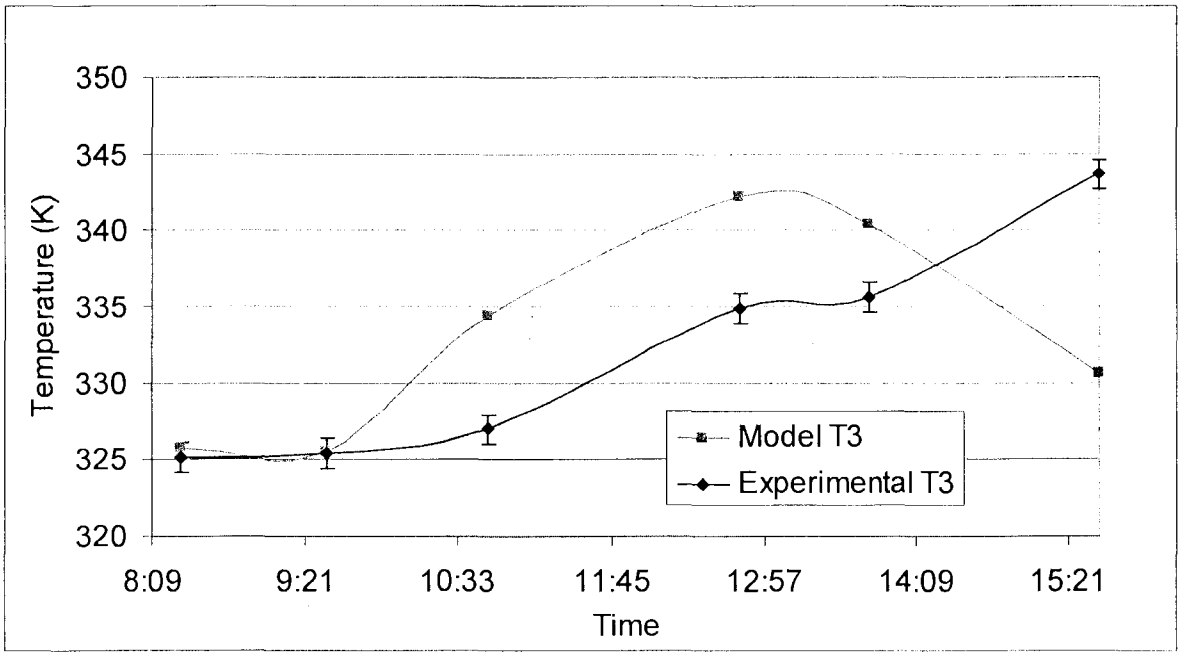

Figure 51. Model vs. Experimental for T3 for July 19th, 2007.

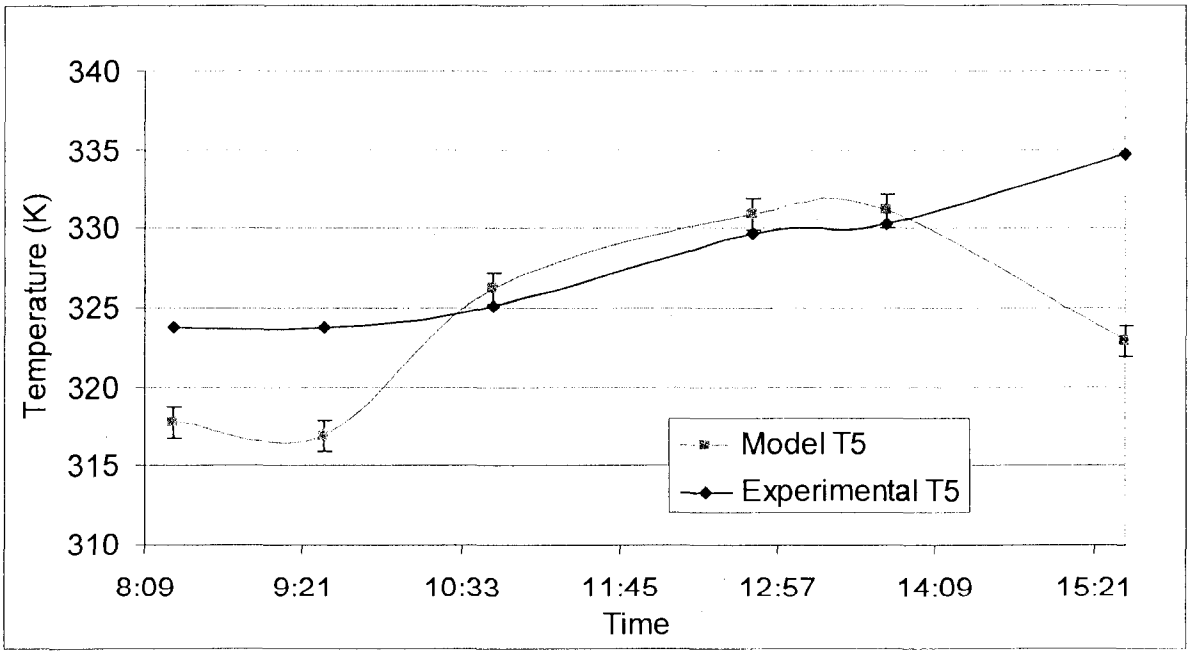

Figure 52. Model vs. Experimental for T5 for July 19th, 2007.

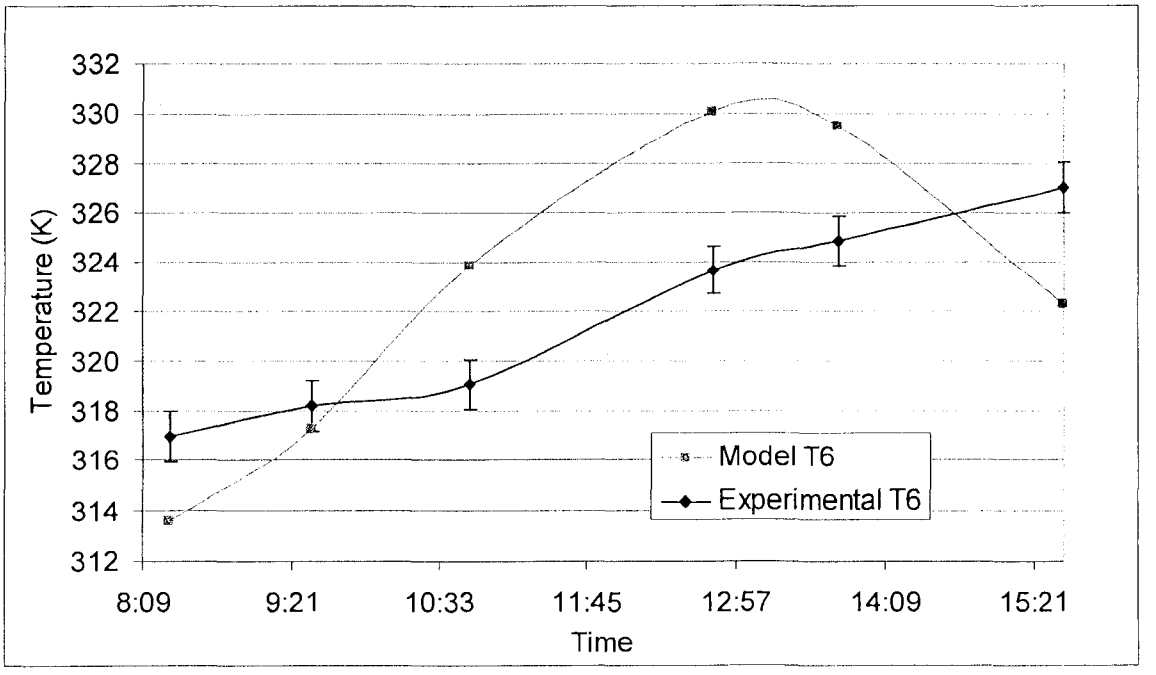

Figure 53. Model vs. Experimental for T6 for July 19th, 2007.

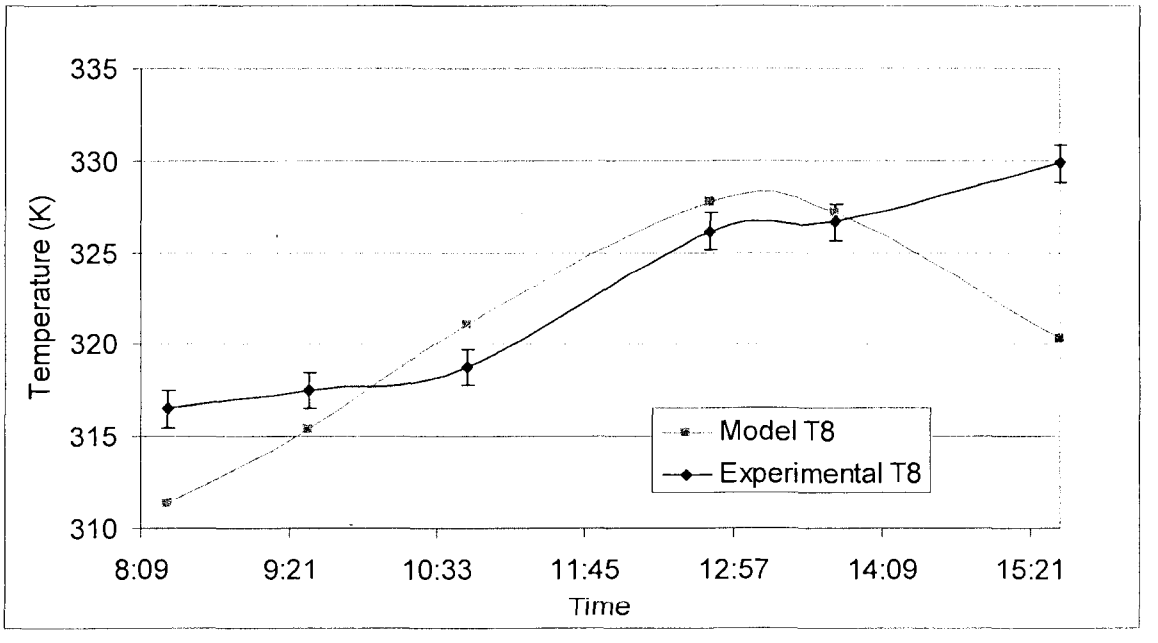

Figure 54. Model vs. Experimental for T8 for July 19th, 2007.

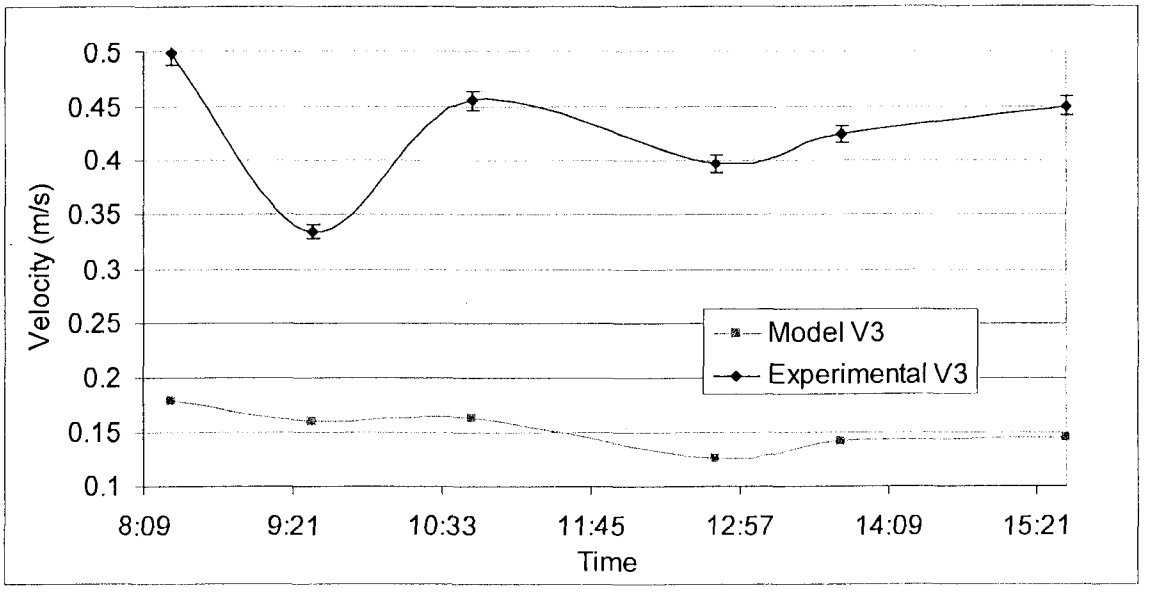

Figure 55. Model vs. Experimental for V3 for July 19th, 2007.

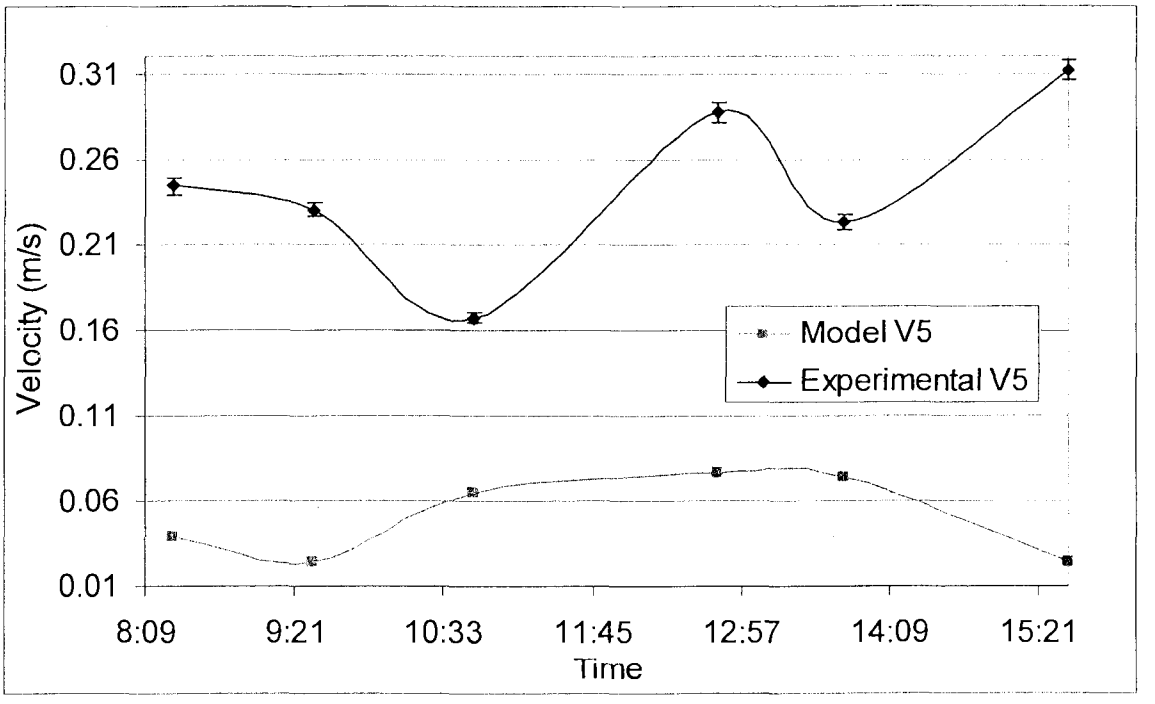

Figure 56. Model vs. Experimental for V5 for July 19th, 2007.

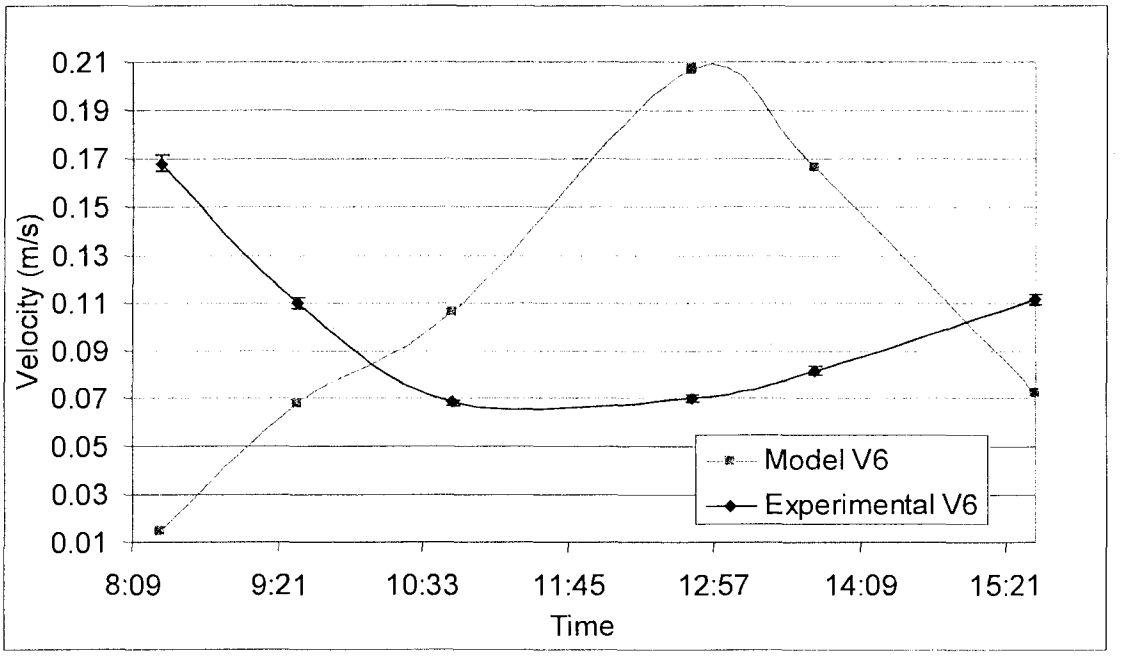

Figure 57. Model vs. Experimental for V6 for July 19th, 2007.

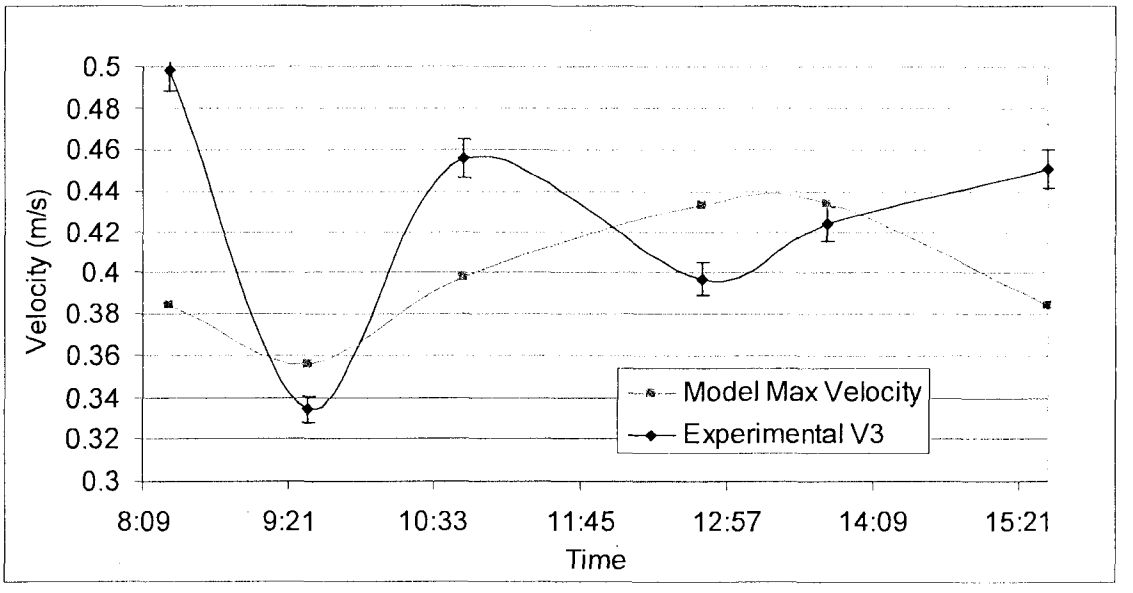

Figure 58. Maximum predicted air velocities vs. V3 for July 19th, 2007.

The inner chamber temperature predictions are higher in most cases although they should be since radiation and wind are not accounted for. The model under predicts the inner chamber velocities in most cases. Figure 58 shows the

maximum predicted air velocities versus the V3 location. Again the model does not take into account the cell packages which might change the air flow at these locations. As in the January case, the air velocities are not predicted very well overall but are in the ballpark range. Outer chamber temperatures can be seen in Figures 59, 60, 61 and 62.

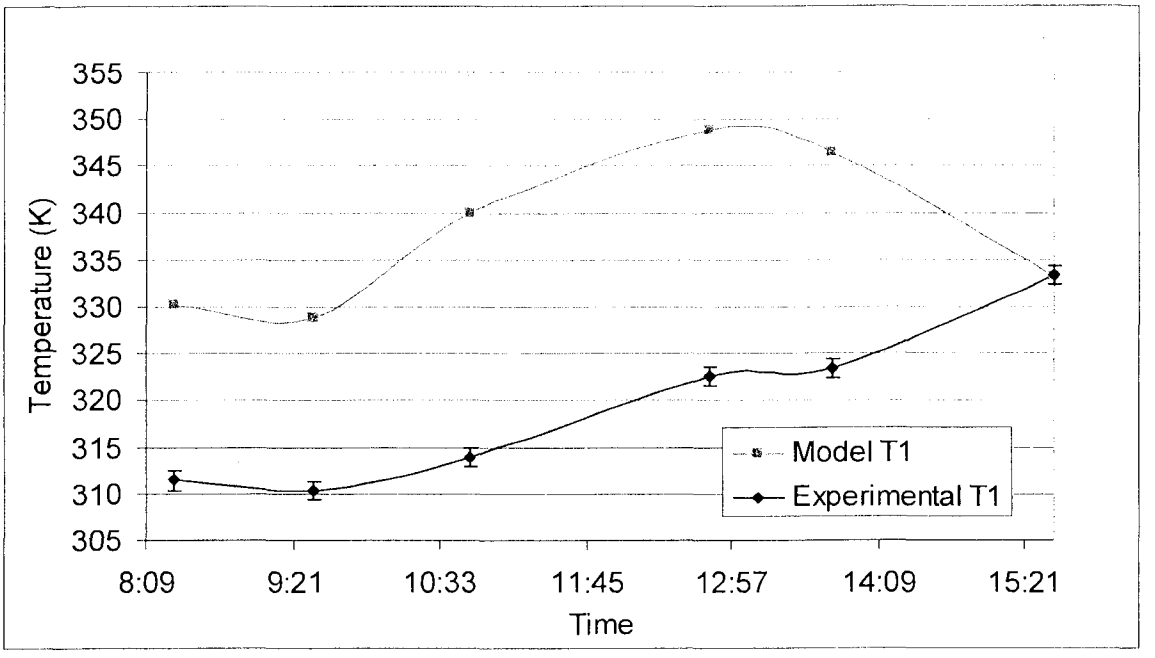

Figure 59. Model vs. Experimental for T1 for July 19th, 2007.

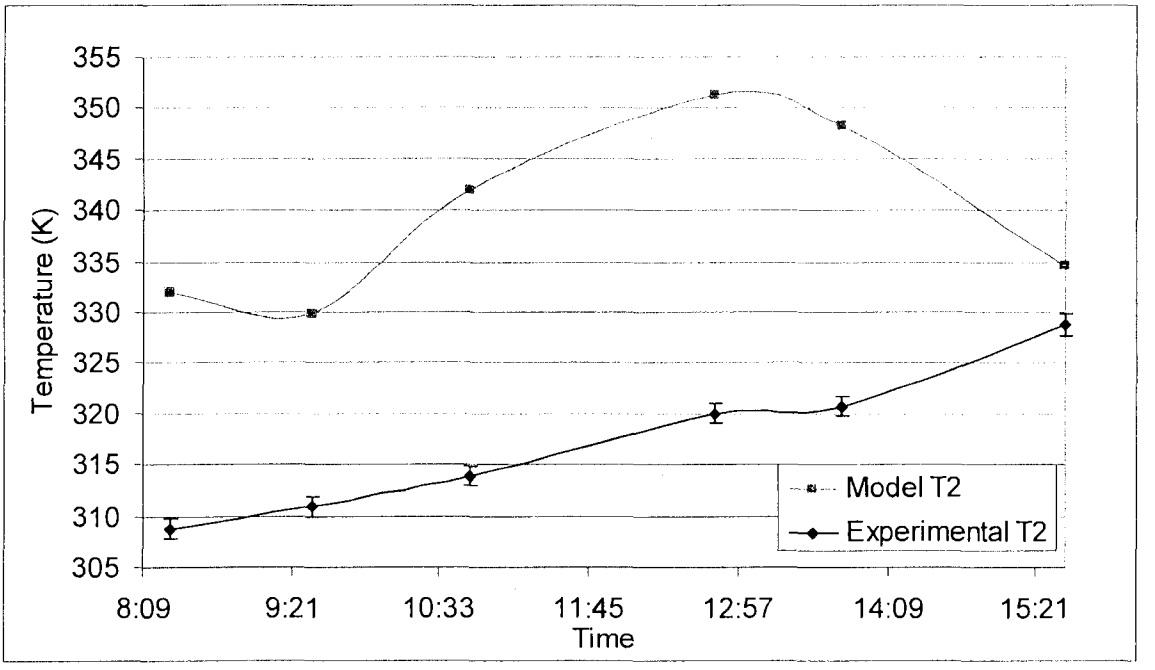

Figure 60. Model vs. Experimental for T2 for July 19th, 2007.

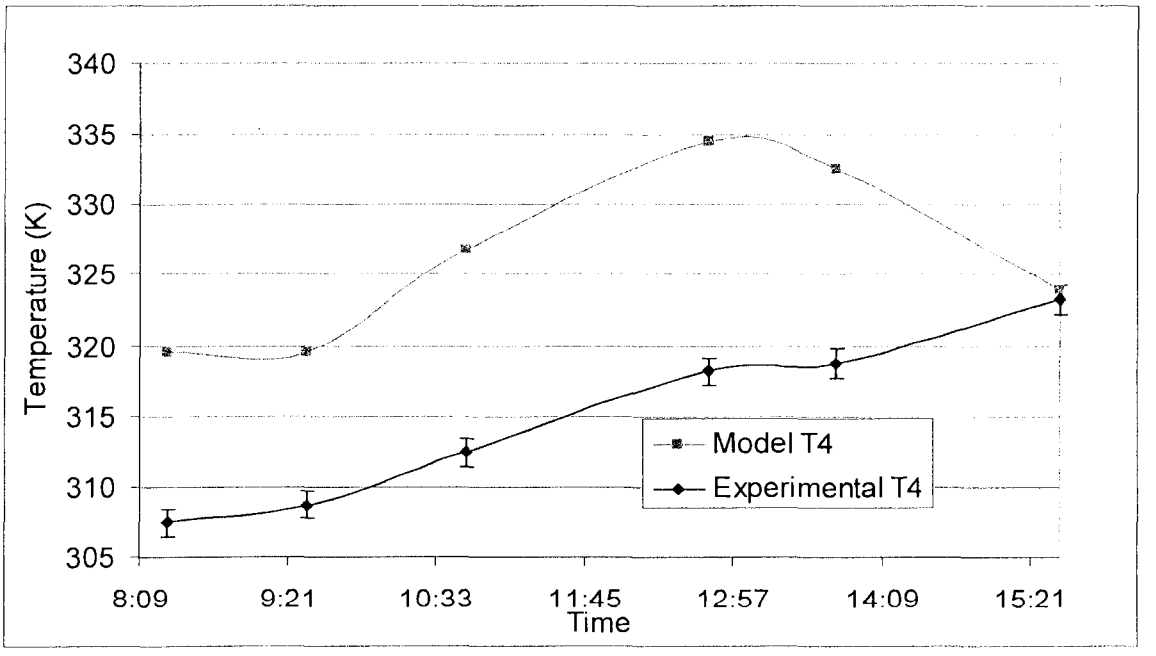

Figure 61. Model vs. Experimental for T4 for July 19th, 2007.

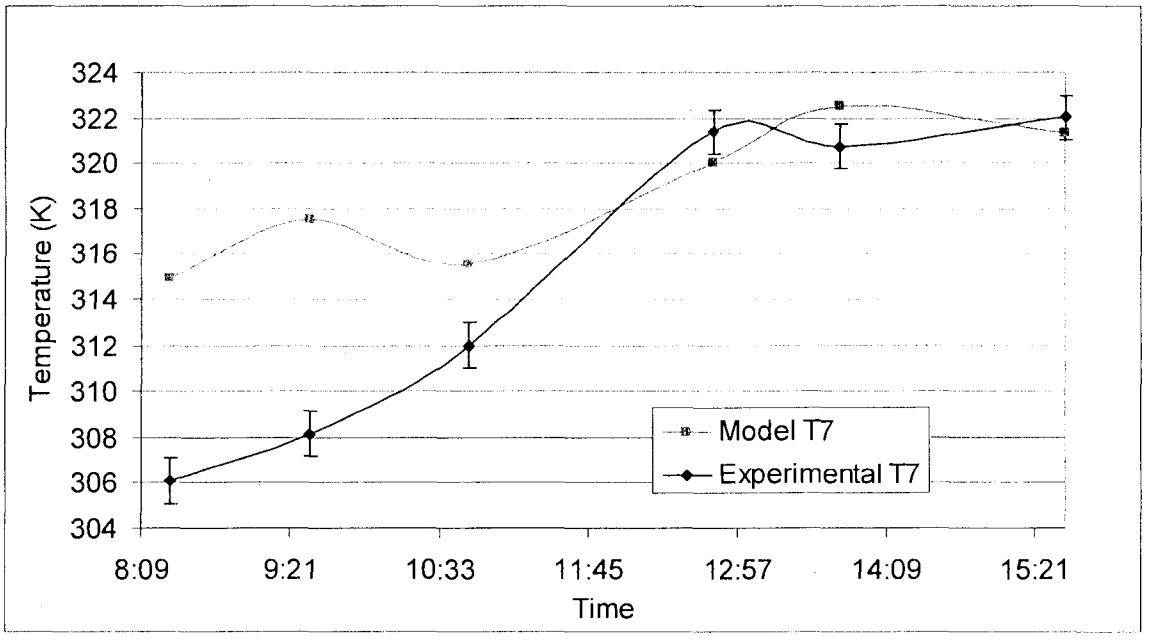

Figure 62. Model vs. Experimental for T7 for July 19th, 2007.

The outer chamber predictions were also much higher than experimental results except for several points in Figure 62. This is probably due to wind and will be examined later. The outer chamber velocities were clearly affected by wind and are not useful for comparison with the model. Previous work on a convection numerical model of this system was examining a worst case scenario [11]. The worst case scenario was one where the ambient temperature is very high, the DNI is very high, and there is no wind. Although a no wind situation is not very common, the prior two conditions are very common in the summer. In order to examine this case it was assumed that the cells had fixed temperatures of 353 K. Figure 63 shows that during the summer, the cell temperatures are very close to 353 K during the peak operating times from 10:00 AM to 2:00 PM. From these results it would seem that this was a good assumption to make.

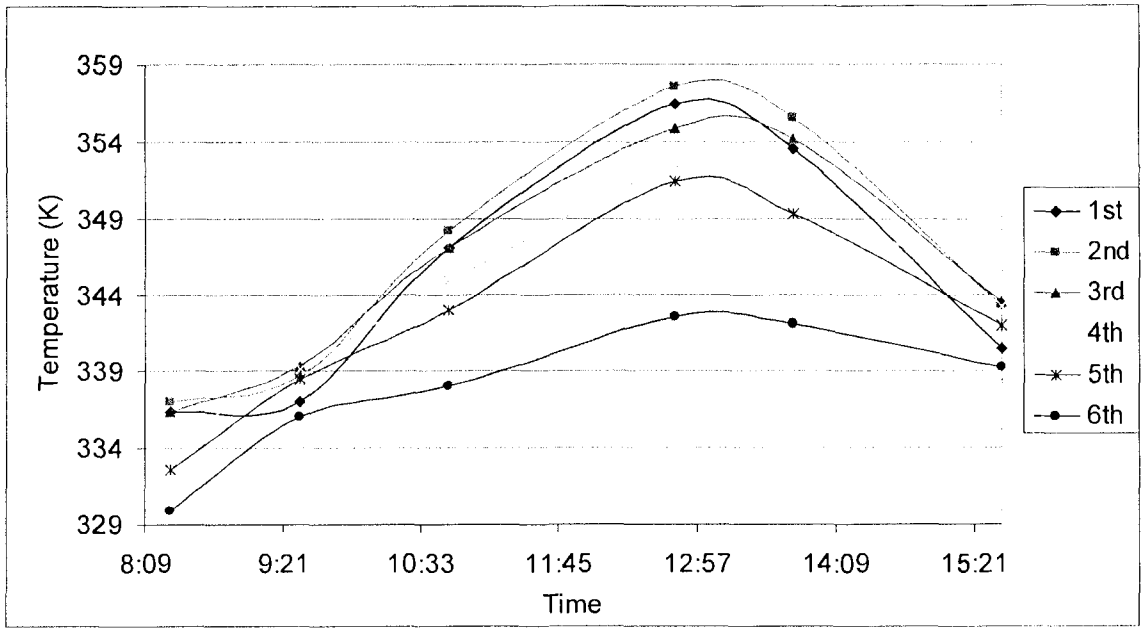

Figure 63. Predicted cell temperatures for July 19th, 2007.

Similarly to the January case, the hottest cells vary throughout the day and are very close together at the beginning and the end of the day. The hottest cells were also on the second and sometimes third row. Table 8 shows the percentage difference for the convection model for July. The percentage differences were much lower for inner chamber temperatures for the July case when compared with the January case.

Table 8. Percentage difference for convection model for July 19th, 2007.

Time	DNI	T_{inf}	Angle	T1	T2	T3	T4	T5	T6	T7	T8
8:23	878.00	306.20	31.30	5.67%	7.12%	0.00%	3.62%	1.58%	0.75%	2.55%	1.33%
9:31	945.80	308.53	45.00	5.66%	5.73%	0.00%	3.18%	1.85%	0.02%	2.69%	0.35%
10:48	972.50	310.29	60.00	7.90%	8.59%	1.93%	4.27%	0.05%	1.18%	0.81%	0.42%
12:46	962.70	312.88	74.60	7.78%	9.41%	1.89%	4.81%	0.09%	1.65%	0.11%	0.20%
13:47	947.70	314.19	69.66	6.76%	8.29%	1.12%	4.00%	0.00%	1.12%	0.23%	0.00%
15:36	898.90	313.98	50.00	0.00%	1.48%	3.53%	0.00%	3.24%	1.16%	0.00%	2.60%
Average	**934.27**	**311.01**	**55.09**	**5.63%**	**6.77%**	**1.41%**	**3.31%**	**1.13%**	**0.98%**	**1.07%**	**0.82%**

Convection with Radiation Model

The P1 model was used again for determining the temperature and velocity profiles. It was desired to find how much of a role radiation plays. The next few figures show temperature predictions with the radiation model.

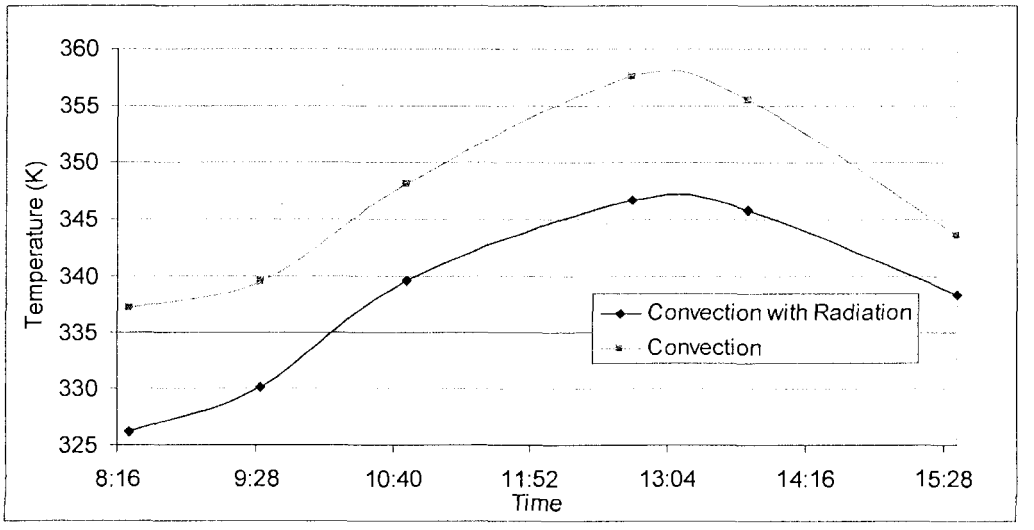

Figure 64. Convection model vs. convection with radiation model maximum temperatures for July 19th, 2007.

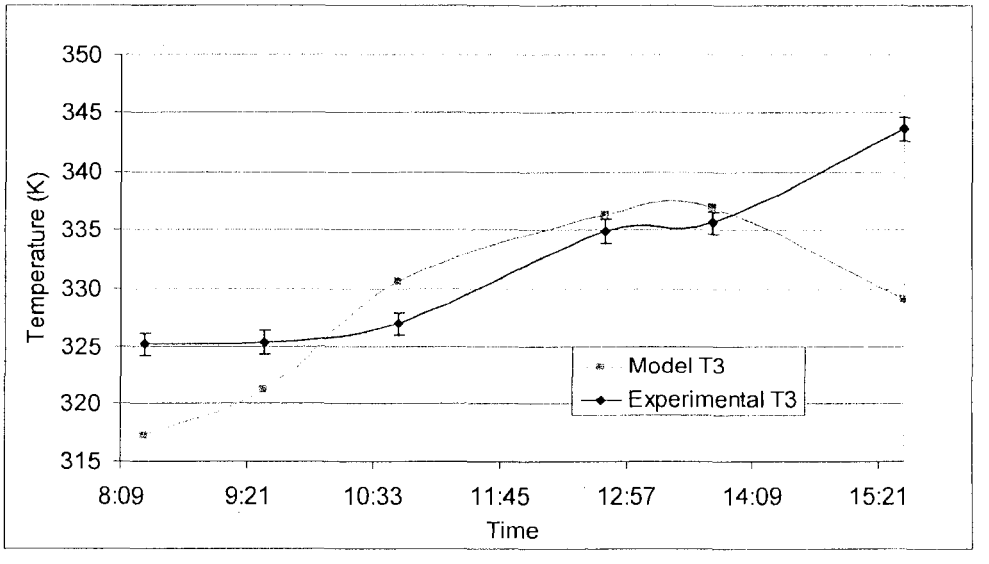

Figure 65. Model vs. Experimental for T3 for July 19th, 2007.

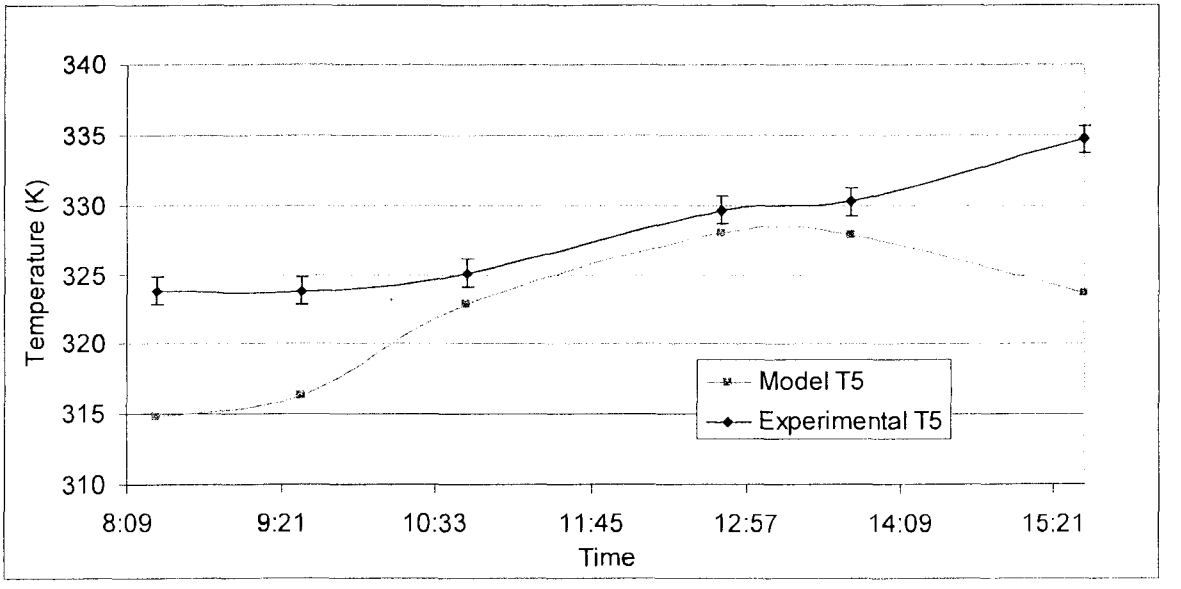

Figure 66. Model vs. Experimental for T5 for July 19th, 2007.

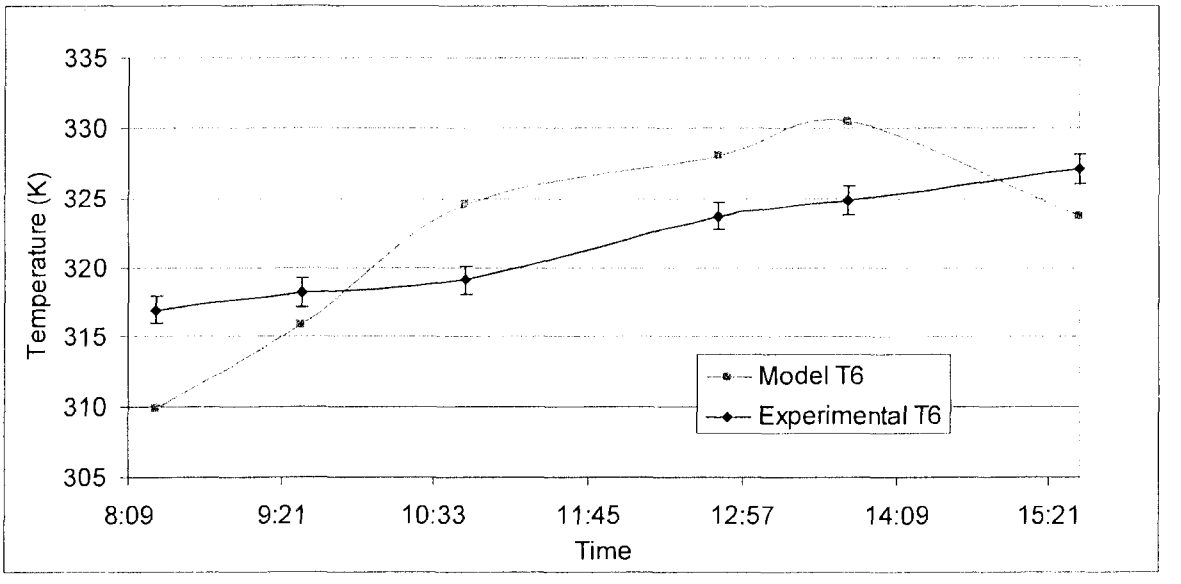

Figure 67. Model vs. Experimental for T6 for July 19th, 2007.

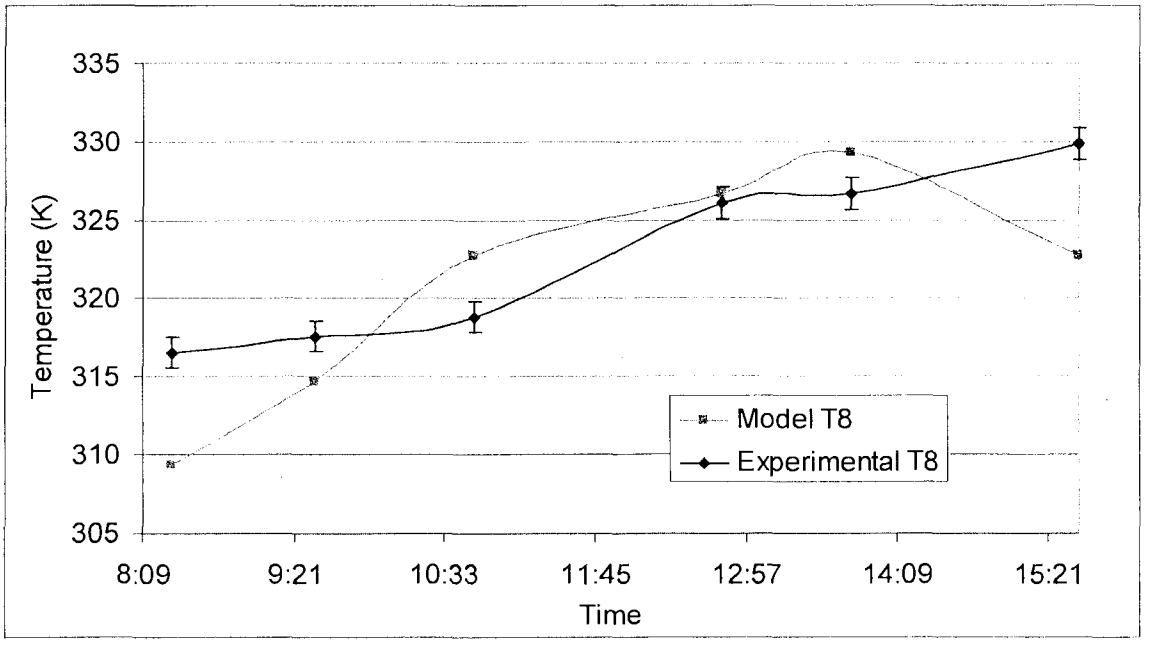

Figure 68. Model vs. Experimental for T8 for July 19th, 2007.

Figure 64 compares the maximum temperatures between the convection model and the convection with radiation model. The radiation model lowered temperatures greatly in some cases when compared to the convection model. The maximum temperature dropped 11 degrees C on the hottest case when the chamber was at about 75 degrees in elevation. The predicted inner chamber temperatures are much closer than in the January case and over predict the temperatures in most places except for T5. The reason for the difference in Figure 66 is most likely that the model has ambient air on the top of the chamber which is not the case in the test chamber. This might be negated by setting the boundary condition of the top wall to having a heat flux of zero. In contrast, the outer chamber temperatures are much different from the model predictions. The

next four figures compare outer chamber temperatures predictions with experimental results.

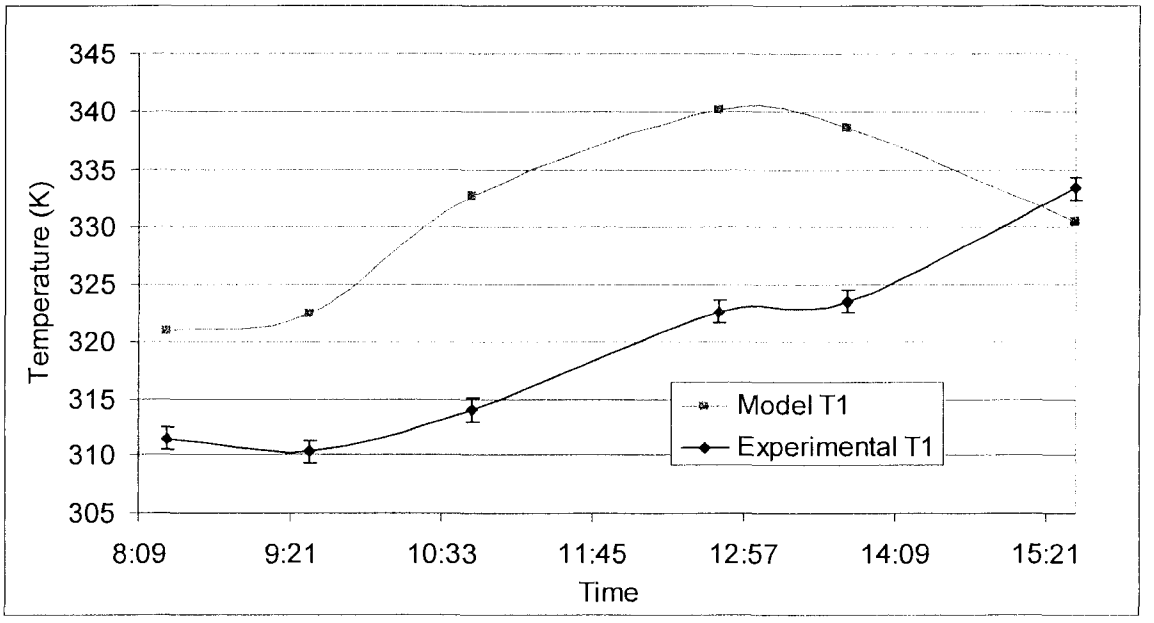

Figure 69. Model vs. Experimental for T1 for July 19th, 2007.

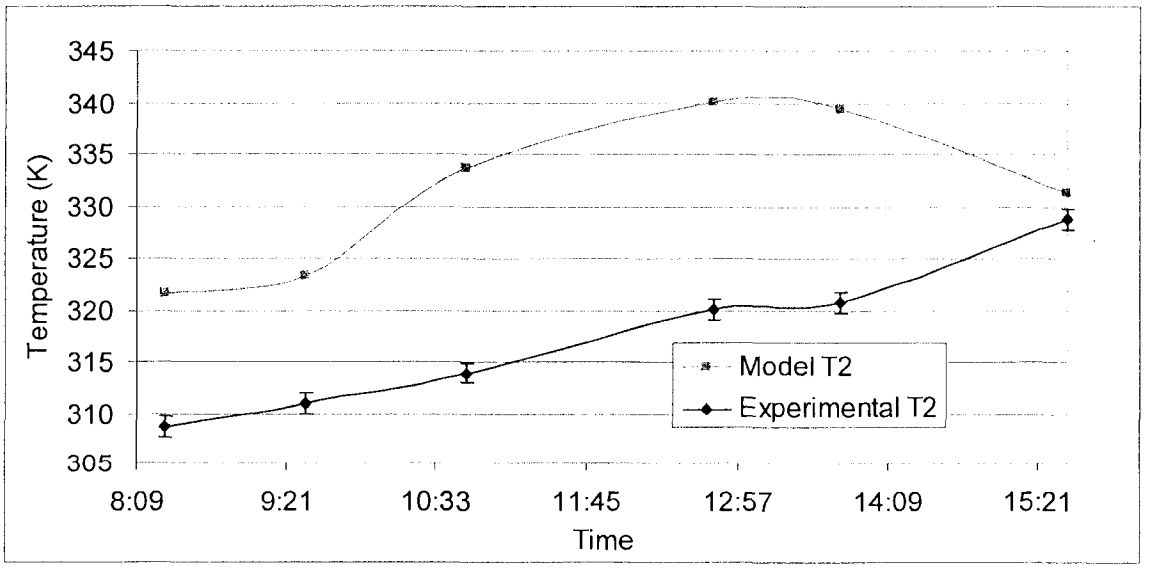

Figure 70. Model vs. Experimental for T2 for July 19th, 2007.

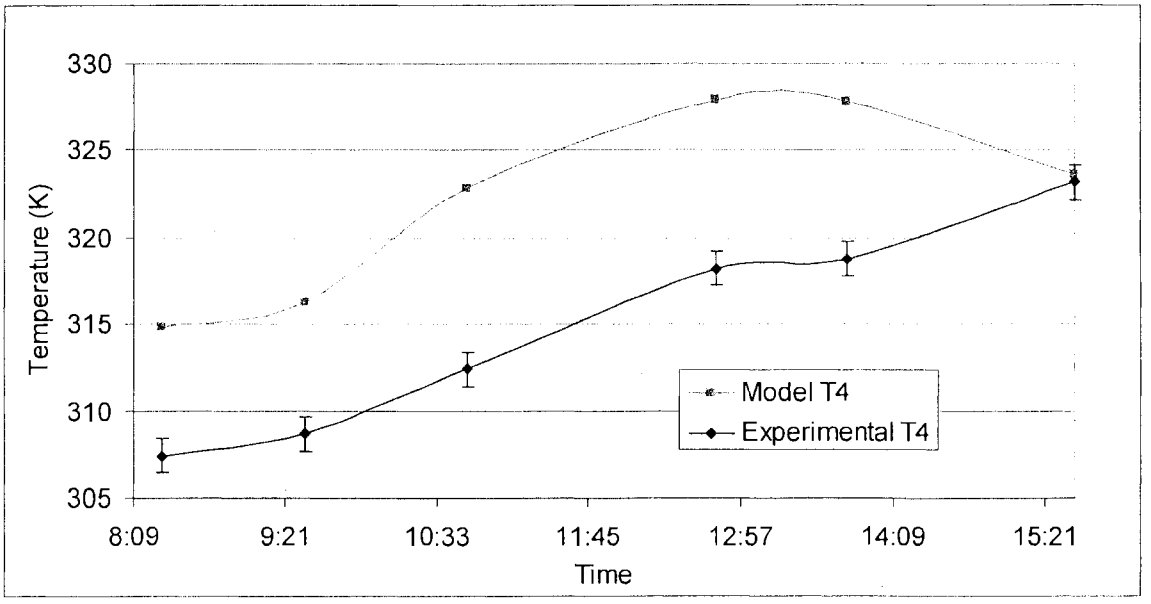

Figure 71. Model vs. Experimental for T4 for July 19th, 2007.

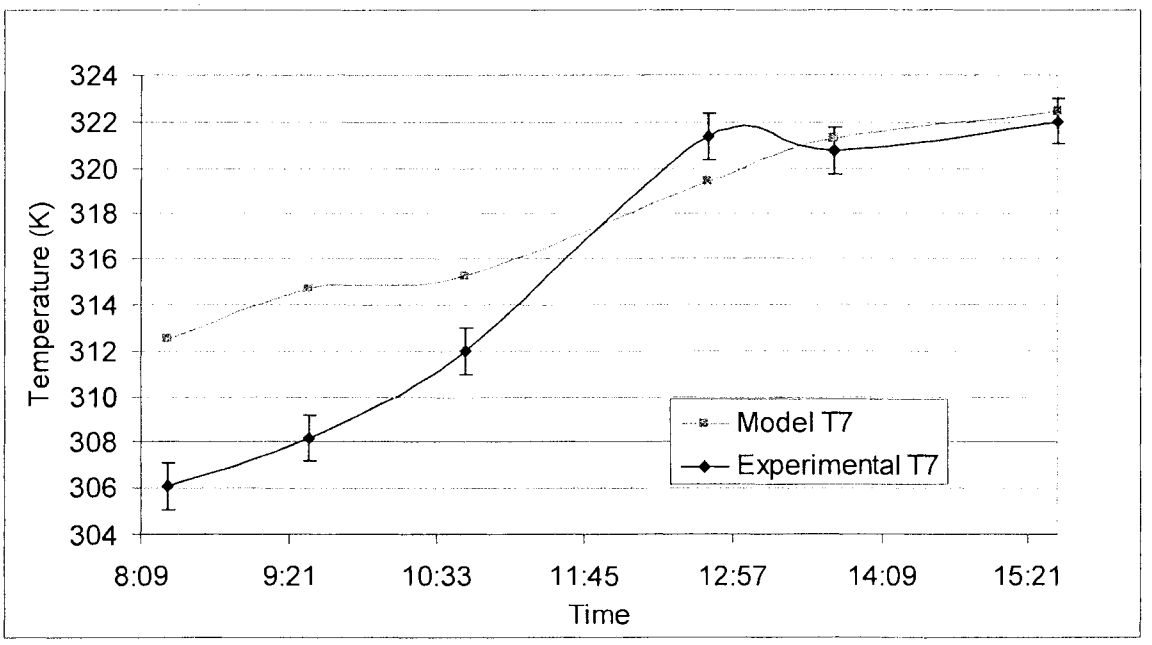

Figure 72. Model vs. Experimental for T7 for July 19th, 2007.

The discrepancy in the outer chamber results is mostly due to wind during the day. Notice the temperatures come closer together on the last point in the day in

each of the figures. To show the wind effect a wind rose plot of the test day can be seen in Figure 73.

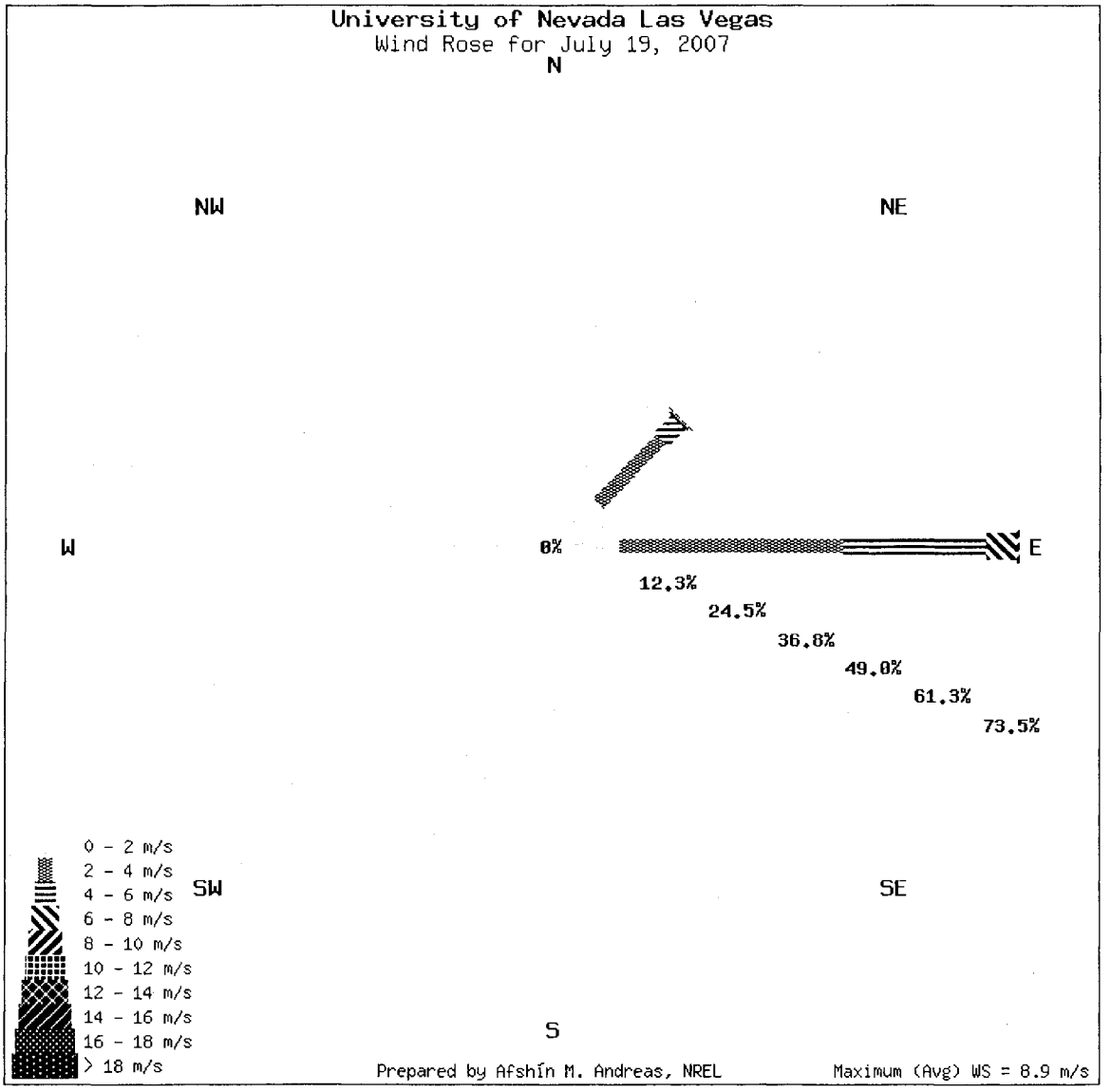

Figure 73. Wind rose plot for July 19, 2007

The wind rose plot shows that the majority of the wind was blowing towards an eastwardly direction and the rest was towards the north east. The eastward wind was during the morning up until noon and a little afternoon. Most of the

afternoon had wind blowing to the northeast. The wind provided a cooling effect in the morning while the unit faced east. The unit is continually moving towards the west until the heat fins are no longer in the path of the wind and thus no longer providing a cooling effect. The average wind speed also decreased as the day progressed. This should explain the majority of discrepancy between the predicted temperatures and measured data. The percentage difference for the temperature predictions were lower with the use of the radiation model and can be seen in Table 9. Predicted cell temperatures can be seen in Figure 74.

Table 9. Percentage difference for temperature predictions with radiation model for July 19th, 2007.

Time	DNI	T_{inf}	Angle	T1	T2	T3	T4	T5	T6	T7	T8
8:23	878.00	306.20	31.30	2.68%	3.80%	2.19%	2.07%	3.66%	1.93%	1.76%	1.96%
9:31	945.80	308.53	45.00	3.58%	3.62%	1.03%	2.12%	2.34%	0.43%	1.79%	0.60%
10:48	972.50	310.29	60.00	5.60%	5.98%	0.81%	3.00%	0.13%	1.36%	0.71%	0.93%
12:46	962.70	312.88	74.60	5.08%	5.95%	0.12%	2.74%	0.55%	1.01%	0.30%	0.00%
13:47	947.70	314.19	69.66	4.31%	5.48%	0.10%	2.52%	0.01%	1.43%	0.00%	0.50%
15:36	898.90	313.98	50.00	0.57%	0.45%	3.97%	0.00%	3.19%	0.72%	0.00%	1.85%
Average	**934.27**	**311.01**	**55.09**	**3.64%**	**4.21%**	**1.37%**	**2.08%**	**1.64%**	**1.15%**	**0.76%**	**0.97%**

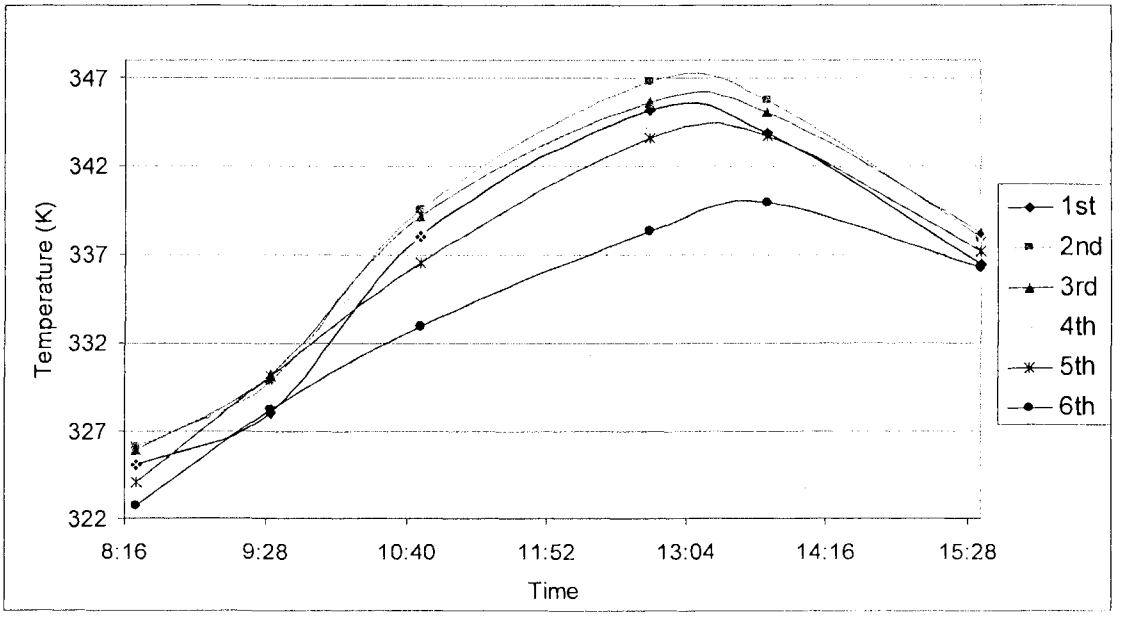

Figure 74. Predicted cell temperatures with radiation model.

One difference between the convection case and the radiation case is that the 3rd row temperature is higher than the 1st row throughout the day. This trend would not be seen had the radiation model not been used.

Multivariable Regression Analysis

The regression analysis for July was done much the same as for the January case. The model's max temperature did not include enough data points to accurately use the regression method and so only the measured data is used. The same location as in the previous regression analysis, T3 which had the highest temperatures during the experiment, was used for this analysis. Figures 75 and 76 show the temperature difference between T3 and the ambient temperature over a range of ambient temperatures at two different DNI values.

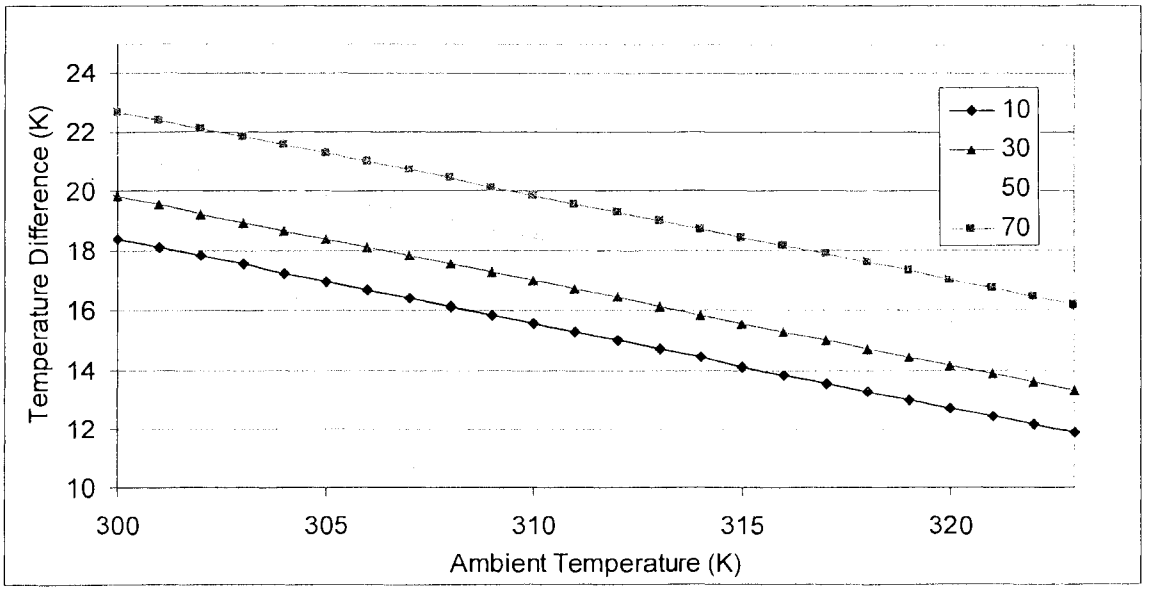

Figure 75. Temperature difference vs. ambient temperature with DNI at 900 W/m^2.

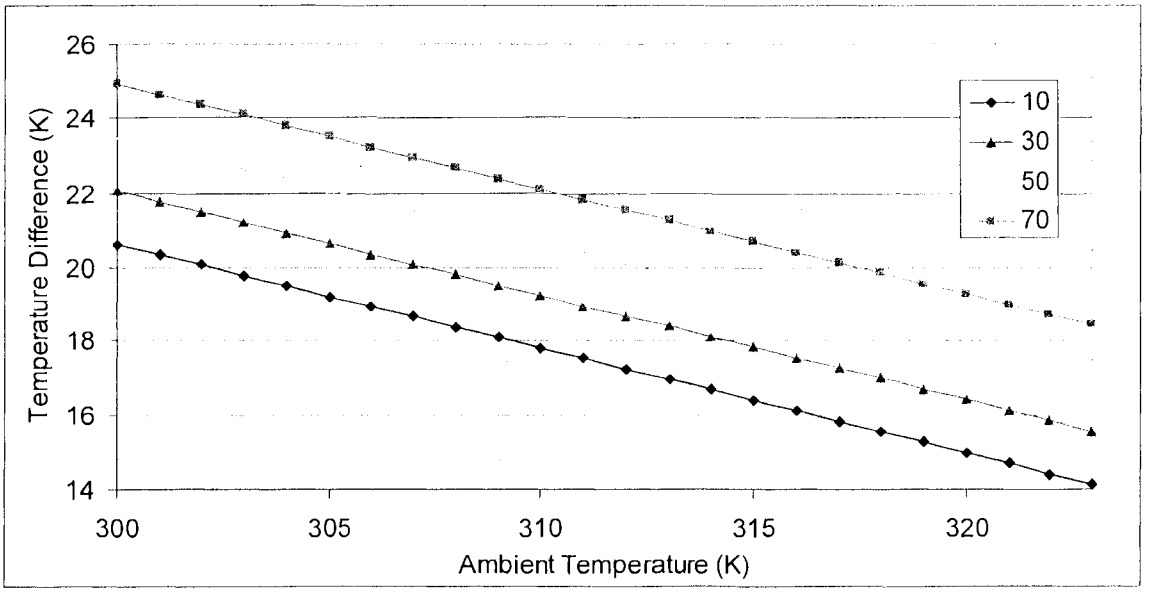

Figure 76. Temperature difference vs. ambient temperature with DNI at 1000 W/m^2.

The July data gave a temperature difference of 4.3 degrees between the 70 degree elevation angle case and the 10 degree. This is double what the January

case gave. The trend is similar to the previous case where the increase in ambient temperature decreases the difference between the temperature at T3 and the environment. The increase in DNI shifts the curves upward and thus increases the temperature difference with the ambient. Both of these results make sense because the increase in DNI increases the power on the cells which in turn raises the temperature.

CHAPTER 5

CONCLUSIONS AND RECOMMENDATIONS

The Amonix chamber was successfully modeled both numerically and experimentally. A method for using the thermal camera on a surface with differing emissivities and external light interference was shown and used. The developed numerical model accurately predicted temperatures with an average percentage difference between measured data of under 2%. Predicted induced air velocities were not as successful but were within range of measured. Both chamber temperatures and air velocities were shown to be a function of direct normal incident radiation, ambient temperature, and chamber elevation angle and established that each of these variables is critical for accurate calculations. It was shown that by not using the radiation model the predicted temperatures are significantly higher than with its use and the locations of the hottest cells may be incorrect. This information may be useful in designing cell placement for the purpose of making plates with more uniform performance. Perhaps cells with higher efficiency could be placed toward the center of the plate, like on the 2nd or 3rd row. This would enable the increase in temperature at these points to be lower and bring cell temperatures for the plate closer together and increase efficiency overall.

Further work could be done by running more in depth simulations where two variables are held constant and the third is changed over a realistic range of values to find how much of an effect it has on the maximum temperatures and air velocities. It might also be of interest to include wind speed and direction as variables in the model to quantify their effects on cooling. The use of the radiation model also provides the opportunity to numerically test different materials or surface coatings with different radiative properties to enhance cooling of the cells. Amonix has recently redesigned their megamodules and done away with dividers between chambers and reoriented the heat sinks to be vertical instead of horizontal. This reorientation will make modeling of a single chamber more difficult since it can no longer be treated symmetrically and will require the use of a 3D mesh. Amonix is also considering installing small wind turbine vents on the top of the megamodule, which are very similar to those used on rooftops, to increase air flow through the module. Finding out how much this would cool the cells would be a very worthwhile study.

Furthermore, Amonix has recently implemented the use of multi-junction cells into their plate and module design. The multi-junction cells have significantly higher efficiency and should be easily adapted into the current model through changing of the cell efficiency and its corresponding relation to temperature. The higher efficiency will lead to lower cell temperatures which should make the cells less sensitive to changes in ambient temperature.

APPENDIX

EQUATIONS USED IN THE MODEL

The Governing Equations

Fluent numerically solves three basic governing equations along with additional transport equations for turbulent flow [10]. The three basic governing equations are the continuity, momentum, and the energy equation. The continuity equation was developed by applying the conservation of mass to an element and can be seen in equation 1 [12].

$$\frac{\partial \rho}{\partial t} + \nabla \cdot (\rho \vec{v}) = S_m \tag{1}$$

where

$\frac{\partial \rho}{\partial t}$ = the change in density over change in time

$\vec{v}$ = velocity vector

S_m = mass added to the continuous phase from the dispersed second phase

The S_m term is specifically for multiphase species transport which is not applicable for the model and thus equals zero. The model also assumed a steady state condition which made any $\frac{\partial}{\partial t}$ terms go to zero. The incompressible ideal gas model was used for calculating density as only a function of temperature.

The second equation was developed by applying conservation of momentum to an element and can be seen in equation 2.

$$\frac{\partial}{\partial t}(\rho\vec{v}) + \nabla \cdot (\rho\vec{v}\vec{v}) = -\nabla p + \nabla \cdot (\overline{\overline{\tau}}) + \rho\vec{g} + \vec{F} \tag{2}$$

where

$\rho =$ density

$\vec{v} =$ velocity vector

$p =$ static pressure

$\overline{\overline{\tau}} =$ stress tensor

$\vec{g} =$ gravitational force vector

$\vec{F} =$ external body force vector

$$\overline{\overline{\tau}} = \mu \cdot [(\nabla\vec{v} + \nabla\vec{v}^{T}) - \frac{2}{3}\nabla \cdot \vec{v}I] \tag{3}$$

where

$\mu =$ molecular viscosity

$I =$ unit tensor

Again the time dependant terms for all equations go to zero. The third equation was developed by applying conservation of energy to an element and can be seen in equation 4.

$$\frac{\partial}{\partial t}(\rho E) + \nabla \cdot (\vec{v}(\rho E + p)) = \nabla \cdot (k_{eff}\nabla T - \sum_{j} h_j \vec{J}_j + (\overline{\overline{\tau_{eff}}} \cdot \vec{v})) + S_h \tag{4}$$

where

$\rho =$ density

$\vec{v} =$ velocity vector

$$E = h - \frac{p}{\rho} + \frac{v^2}{2} \quad (5)$$

$h =$ sensible enthalpy = $\sum_j Y_j h_j$ (6)

$Y_j =$ mass fraction of the species j

$$h_j = \int_{T_{ref}}^{T} c_{p,j} dT \quad (7)$$

$c_{p,j} =$ specific heat of the species

$T_{ref} =$ 298.15 K

$p =$ static pressure

$k_{eff} =$ effective thermal conductivity = k + k_t (8)

$k_t =$ turbulent thermal conductivity

$T =$ temperature

$\vec{J}_j =$ diffusion flux of the species j

$\bar{\bar{\tau}} =$ stress tensor

$S_h =$ defined volumetric heat sources

Since air was the only gas involved in the model, multi-species transport was irrelevant to the energy equation. The turbulent thermal conductivity required the use of other equations from the turbulence k-ε model and will be shown in the next section. When the energy equation is applied to a solid it becomes equation 9 with the same variable definitions as above.

$$\frac{\partial}{\partial t}(\rho h) + \nabla \cdot (\vec{v} \rho h) = \nabla \cdot (k \nabla T) + S_h \quad (9)$$

Turbulence Model

The standard k-ε model was chosen for determining the effect of turbulence in this model. It is a semi-empirical model and uses two transport equations 10 and 11.

$$\frac{\partial}{\partial t}(\rho k)+\frac{\partial}{\partial x_i}(\rho k u_i)=\frac{\partial}{\partial x_j}[(\mu+\frac{\mu_t}{\sigma_k})\frac{\partial k}{\partial x_j}]+G_k+G_b-\rho\varepsilon-Y_m+S_k \tag{10}$$

$$\frac{\partial}{\partial t}(\rho\varepsilon)+\frac{\partial}{\partial x_i}(\rho\varepsilon u_i)=\frac{\partial}{\partial x_j}[(\mu+\frac{\mu_t}{\sigma_\varepsilon})\frac{\partial \varepsilon}{\partial x_j}]+C_{1\varepsilon}\frac{\varepsilon}{k}(G_k+C_{3\varepsilon}G_b)-C_{2\varepsilon}\rho\frac{\varepsilon^2}{k}+S_\varepsilon \tag{11}$$

where

ρ = density

k = turbulence kinetic energy

u_i = velocity component

μ = molecular viscosity

μ_t = turbulent viscosity

σ_k = turbulent Prandtl number for k

$G_k = -\rho\overline{u_i' u_j'}\frac{\partial u_j}{\partial x_i}$ generation of k from velocity gradients (12)

$G_b = \beta g_i \frac{\mu_t}{\mathrm{Pr}_t}\frac{\partial T}{\partial x_i}$ generation of k from buoyancy (13)

β = coefficient of thermal expansion

Pr_t = turbulent Prandtl number for energy

ε = turbulence dissipation rate

Y_m = fluctuating dilatation in compressible turbulence

S_k = user defined source term

σ_ε = turbulent Prandtl number for ε

$C_{1\varepsilon}$ = 1.44

$C_{2\varepsilon}$ = 1.92

$C_{3\varepsilon}$ = constant for multiphase model

S_ε = user defined source term

Radiation Model

Fluent also solves the radiative transfer equation for participating media and can be seen below in equation 14.

$$\frac{dI(\vec{r},\vec{s})}{ds} + (a+\sigma_s)I(\vec{r},\vec{s}) = an^2 \cdot \frac{\sigma T^4}{\pi} + \frac{\sigma_s}{4\pi}\int_0^{4\pi} I(\vec{r},\vec{s}')\Phi(\vec{s}\cdot\vec{s}')d\Omega' \qquad (14)$$

where

$\vec{r}$ = position vector

$\vec{s}$ = direction vector

a= absorption coefficient

σ_s = scattering coefficient

I = radiation intensity

n = refractive index

σ = Stephan-Boltzmann constant ($5.672 \cdot 10^{-8}$ W/m^2-K)

$\vec{s}'$ = scattering direction vector

T= temperature

Φ = phase function

Ω' = solid angle

Since air is not considered a participating media, the absorption coefficient and the scattering coefficient were set to zero which reduced the equation to the derivative of intensity over direction equals zero. The P1 model was used and gave equations for more useful radiative flux at the walls.

$$q_{r,w} = -\frac{\varepsilon_w}{2(2-\varepsilon_w)} \cdot (4\sigma T_w^4 - G_w) \qquad (15)$$

where

$q_{r,w}$ = wall radiative flux

ε_w = emissivity of wall

T_w = wall temperature

G_w = incident radiative flux

REFERENCES

[1] Anderson, Betty. Anderson, Richard. Fundamentals of Semiconductor Devices. McGraw Hill. 2005 (683-689).

[2] Yoon, Sewang. Garboushian, Vahan. "Reduced Temperature Dependence of High-Concentration Photovolatic Solar Cell Open-Circuit Voltage (Voc) at High Concentration Levels." IEEE. CH3365. 1994.

[3] Slade, A., Gordon, R., Dutra, D., Garboushian, V., "Long Term Reliability of Mass-Produced High-Efficiency Silicon Point-Contact Solar Cells Under 250X Concentration." IEEE. 2002:1015-1018

[4] Sahm, A., Gray, A., Boehm, R., Stone, K., "Cleanliness Maintenance for an Amonix Lens System." ISEC2005-76036, 2005 International Solar Energy Conference, August 6-12, 2005, Orlando, Florida.

[5] Cyro Industries. "Acrylite GP, Acrylite FF Light Transmission and Reflectance." Parsippany, NJ. 2001.

[6] "Solar Spectral Irradiance: Air Mass 1.5." NREL. Retrieved on March 27, 2008 from http://rredc.nrel.gov/solar/spectra/am1.5/#a.

[7] "Candle Stick Sensor.' Advanced Thermal Solutions Inc. Retrieved on March 27, 2008 from http://www.qats.com/productdata/Candlestick_sensor.pdf.

[8] "ThermaCAM E45 Users Manual." FLIR Systems. Publ. No. 1558015 Rev. a155. February 6, 2006.

[9] Cosby, Robert M., "The Linear Fresnel Lens Solar Concentrator: Transverse Tracking Error Effects." Muncie Ind., Ball State University. NASA. August 1977.

[10] Fluent 6.2 User's Guide. Fluent Inc. Chapter 12.3.2. 2005.

[11] Gray, Allison. "Modeling a Passive Cooling System for Photovolatic Cells Under Concentration." MS Thesis. University of Nevada, Las Vegas. 2007.

[12] Jiji, Latif M., Heat Convection. City University of New York, New York. 2006 (21- 42)

VITA

Graduate College
University of Nevada, Las Vegas

Aaron Sahm

Local Address:
1324 Maplegrove Cir
Las Vegas, NV 89108

Degrees:
Bachelor of Science, Mechanical Engineering, 2006
University of Nevada, Las Vegas

Publications:

Sahm, A., Gray, A., Boehm, R., Stone, K., "Cleanliness Maintenance for an Amonix Lens System." ISEC2005-76036, 2005 International Solar Energy Conference, August 6-12, 2005, Orlando, Florida.

Khalil, I., Sahm, A., Boehm, R., "Wet or Dry Cooling?" ISEC2006-99082, 2006 International Solar Energy Conference, July 8-13, 2006, Denver, Colorado.

Gray, A., Hale, M.J., Sahm, A., Newmarker, M., Hurt, R., Boehm, R., Andreas, A., Gotseff, P., Stoffel, T., "Southern Nevada Renewable Resource Assessment." ASME Energy Sustainability 2007. June 27-30, 2007, Long Beach, California.

Sahm, A., Stone, K., Boehm., R., Gray, A., "Modeling a High Concentration Photovoltaic System." ASES Solar 2008. May 5-8, 2008. San Diego, California.

Thesis Title: Thermal Modeling of a High Concentration Photovoltaic System

Thesis Examination Committee:
Chairperson, Dr. Robert Boehm, Ph. D.
Committee Member, Dr. Jian Ma, Ph. D.
Committee Member, Dr. Yitung Chen, Ph. D.
Graduate College Representative, Dr. Yahia Baghzouz, Ph. D.